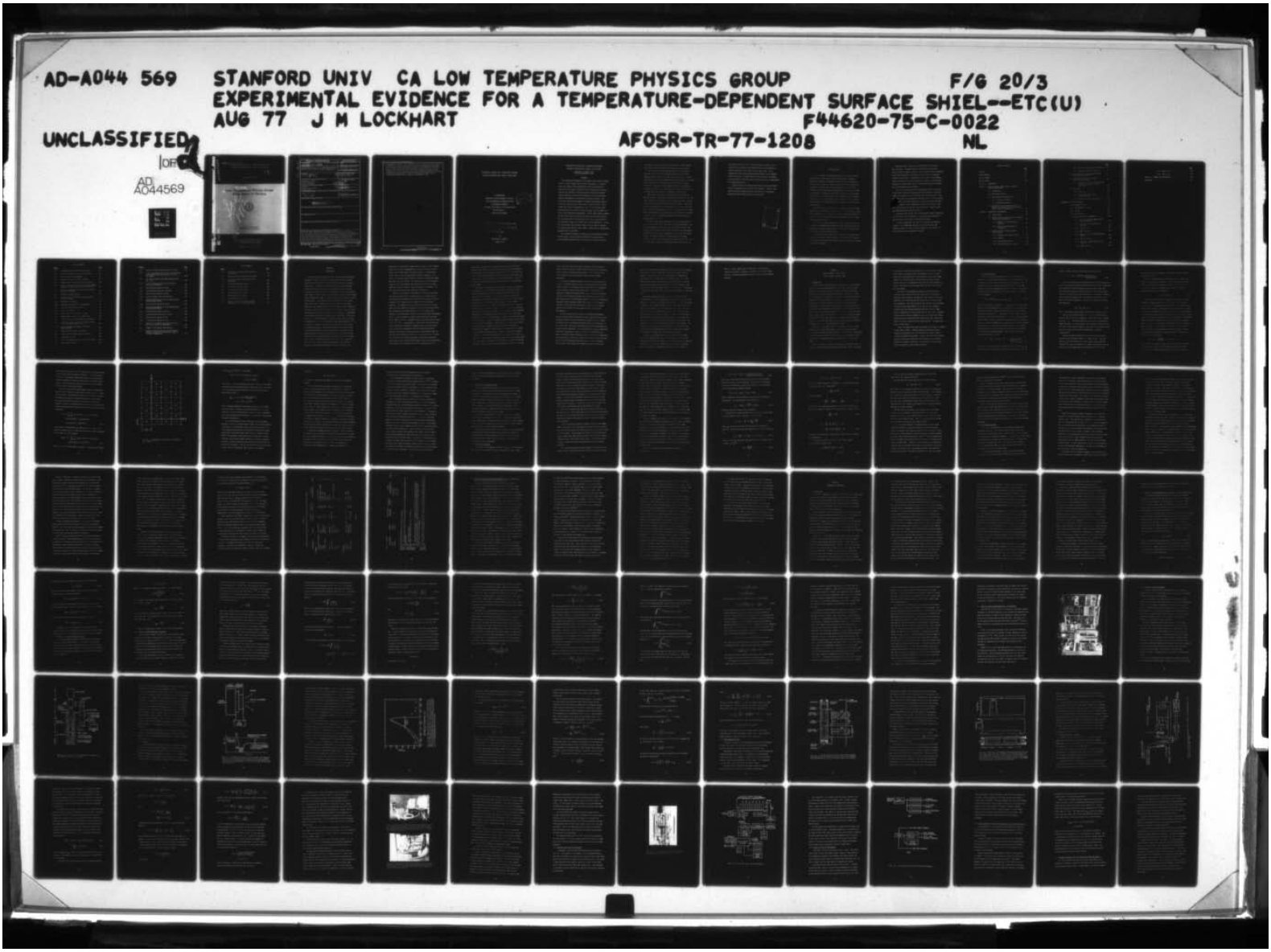
AD-A044 569 STANFORD UNIV CA LOW TEMPERATURE PHYSICS GROUP F/G 20/3
EXPERIMENTAL EVIDENCE FOR A TEMPERATURE-DEPENDENT SURFACE SHIEL--ETC(U)
AUG 77 J M LOCKHART F44620-75-C-0022
UNCLASSIFIED AFOSR-TR-77-1208 NL



AD A044569

AFOSR-TR- 77-1208

EXPERIMENTAL EVIDENCE FO

SURFACE SHIELDING EFFE

by

James Mar

410396

Low Temperatur

Department

STANFORD

STANFORD,

DDC FILE COPY

This research was s

Air Force Office

under Contract F

DDC

SECURITY CLASSIFICATION OF THIS PAGE (When Data Entered)

REPORT DOCUMENTATION PAGE	READ INSTRUCTIONS BEFORE COMPLETING FORM
1. REPORT NUMBER: AFOSR-TR- 77 - 1208	2. GOVT ACCESSION NO. / 3. RECIPIENT'S CATALOG NUMBER
4. TITLE (and Subtitle): EXPERIMENTAL EVIDENCE FOR A TEMPERATURE-DEPENDENT SURFACE SHIELDING EFFECT INSIDE A COPPER TUBE.	5. TYPE OF REPORT & PERIOD COVERED: Interim
	6. PERFORMING ORG. REPORT NUMBER
7. AUTHOR(s): James Marcus Lockhart	8. CONTRACT OR GRANT NUMBER(s): F44620-75-C-0022
9. PERFORMING ORGANIZATION NAME AND ADDRESS: Department of Physics, Stanford University, Stanford CA 94025	10. PROGRAM ELEMENT, PROJECT, TASK AREA & WORK UNIT NUMBERS: 61102F, 2301/A5
11. CONTROLLING OFFICE NAME AND ADDRESS: AFOSR/NP, Bolling AFB, Bldg.410, Wash DC 20332	12. REPORT DATE: August 1977
	13. NUMBER OF PAGES: 181
14. MONITORING AGENCY NAME & ADDRESS (if different from Controlling Office): 188 p.	15. SECURITY CLASS. (of this report): Unclassified
	15a. DECLASSIFICATION/DOWNGRADING SCHEDULE

16. DISTRIBUTION STATEMENT (of this Report)

Approved for public release; distribution unlimited.

17. DISTRIBUTION STATEMENT (of the abstract entered in Block 20, if different from Report)

18. SUPPLEMENTARY NOTES

19. KEY WORDS (Continue on reverse side if necessary and identify by block number)

20. ABSTRACT (Continue on reverse side if necessary and identify by block number)

The temperature dependence of the ambient axial electric field inside a vertical copper tube has been investigated. A vertical metal tube subject to the gravitational field of the Earth is expected to have spatial variations in the electrostatic potential along its axis because of contract potential differences between adjacent crystals in the metal and because of the gravitationally-induced rearrangement of the metallic electrons and ions. The result of a previous measurement by Witteborn and Fairbank (WF) of the ambient axial electric field inside a copper tube at 4.2 degree K is roughly four orders

DD FORM 1 JAN 73 1473 EDITION OF 1 NOV 65 IS OBSOLETE

UNCLASSIFIED

SECURITY CLASSIFICATION OF THIS PAGE (When Data Entered)

411396

of magnitude too small to be consistent with the predictions of the theory of Dessler et al. and the results of several room temperature measurements. Schiff, among others, pointed out that the WF result would be consistent with the other results if a shielding effect involving electrons on the inside surface of the tube were to exist at 4.2 degree K but not at room temperature. In this work the electron time-of-flight method of WF was used to measure the ambient axial electric field inside a copper tube at temperatures ranging from 4.2 degree K to 300 degrees K.

EXPERIMENTAL EVIDENCE FOR A TEMPERATURE-DEPENDENT SURFACE SHIELDING EFFECT INSIDE A COPPER TUBE

A DISSERTATION

SUBMITTED TO THE DEPARTMENT OF PHYSICS

AND THE COMMITTEE ON GRADUATE STUDIES

OF STANFORD UNIVERSITY

IN PARTIAL FULFILLMENT OF THE REQUIREMENTS

FOR THE DEGREE OF

DOCTOR OF PHILOSOPHY

DDC
RECEIVED
SEP 26 1977
C

AIR FORCE OFFICE OF SCIENTIFIC RESEARCH (AFSC)
NOTICE OF TRANSMITTAL TO DDC
This technical report has been reviewed and is
approved for publ[illegible] release IAW AFR 190-12 (7b).
Distribution is unlimited.
A. D. BLOSE
Technical Information Officer

By

James Marcus Lockhart

August 1976

EXPERIMENTAL EVIDENCE FOR A TEMPERATURE-DEPENDENT

SURFACE SHIELDING EFFECT INSIDE A COPPER TUBE

James Marcus Lockhart, Ph.D.
Stanford University, 1976

ABSTRACT

The temperature dependence of the ambient axial electric field inside a vertical copper tube has been investigated. A vertical metal tube subject to the gravitational field of the Earth is expected to have spatial variations in the electrostatic potential along its axis because of contact potential differences between adjacent crystals in the metal and because of the gravitationally-induced rearrangement of the metallic electrons and ions. The result of a previous measurement by Witteborn and Fairbank (WF) of the ambient axial electric field inside a copper tube at 4.2°K is roughly four orders of magnitude too small to be consistent with the predictions of the theory of Dessler et al. and the results of several room temperature measurements. Schiff, among others, pointed out that the WF result would be consistent with the other results if a shielding effect involving electrons on the inside surface of the tube were to exist at 4.2°K but not at room temperature. In this work the electron time-of-flight method of WF was used to measure the ambient axial electric field inside a copper tube at temperatures ranging from 4.2°K to 300°K.

The relevant literature on theoretical and experimental studies of patch effect fields and strain-induced fields (particularly gravitationally-induced fields) in and near the surface of metals

is reviewed. Some ways in which the discrepancy between the WF result and the other results could be resolved are mentioned.

The slow electron time-of-flight method which was used to study the ambient field is discussed and the versions of the apparatus used at 300°K, 77°K, and 4.2°K are described. A drift tube heater and temperature monitor system is described which allows the 4.2°K version of the apparatus to be used over the range 4.2°K-11°K. The manner in which ambient fields are measured is discussed in detail, as is the effect of the delayed emission of electrons from electrostatic and magnetic potential traps.

Room temperature results are presented which indicate an ambient electric field inside the tube of more than 10^{-6} V/m. This value is essentially consistent with the room temperature measurements of strain-induced fields made by other workers. Data taken at 77°K is presented; it is quite similar to the room temperature data. Data from experiments at 4.2°K is described and it is shown that this data implies an ambient field in the tube at 4.2°K which is several orders of magnitude smaller than the ambient field found at 300°K and 77°K.

Ambient field studies made with drift tube temperatures of 4.2°K, 4.3°K, 4.4°K, 6.3°K, 9°K, and 11°K are then described. The 4.2°K measurements in this series were made with the drift tube heating system in place; they yielded an ambient field measurement consistent with the earlier measurement at 4.2°K and with the WF result. The ambient field at 4.3°K was found to be roughly 3×10^{-8} V/m, while at 4.4°K the field was about 3×10^{-7} V/m. For the three higher values of temperature the ambient field was in

the range $(3.5\text{-}8) \times 10^{-7}$ V/m. This last range of values is consistent with the ambient field expected from the gravitationally-induced distortion of the lattice of the copper tube. It is suggested that the observed temperature dependence of the ambient field in the tube is a manifestation of the presence of a surface shielding effect in the tube which is functional only at temperatures below approximately 6°K.

Sources of error are discussed and various consistency checks which were performed on the results are described. Finally, some possible physical mechanisms which could produce a temperature-dependent surface shielding effect are mentioned.



ACKNOWLEDGMENTS

It is a pleasure to acknowledge the advice, support, and continued enthusiasm provided by my principal adviser, Professor William M. Fairbank. His interest in the fundamental problems in physics and his positive outlook have been a constant source of inspiration. An equally great debt of gratitude is due Dr. Fred C. Witteborn, without whose many contributions this work would not have been possible. In addition to providing me with an excellent apparatus with which to begin my work, he has continuously given generously of his time to provide advice and assistance in all phases of the experiment. He also made many useful comments on the manuscript of this thesis.

During the course of this work I have profited from many informative discussions with Dr. John Madey and Dr. Brian Kincaid. I also wish to thank Prof. A. L. Fetter, Prof. R. P. Giffard, and Prof. W. A. Little for their critical reading of the manuscript and for serving on my examining committee.

The thin-film tunnel cathodes used in the experiment were fabricated in collaboration with Forrest Futtere, formerly of the Stanford solid state shop, whose expertise in thin-film technology made it possible to obtain reliable devices.

I am grateful to Dr. John Turneaure and to the Stanford Nuclear Physics Group for the loan of equipment. Dr. Turneaure also spent a considerable amount of time helping me set up a data analysis program on the PDP-11 computer.

Many people have contributed to the technology involved in this experiment. Wolfgang Jung and the machine shop crew have always provided cheerful assistance. Bill Holding has been especially helpful with suggestions and advice on the construction and maintenance of electronics. Herb Rader has often gone to considerable effort to provide the necessary hundreds of liters of liquid helium, frequently on rather short notice. Administrative duties have been very ably managed by Ms. Sharon Hoo.

All of my colleagues in the Low Temperature Physics Group have at one time or another provided advice and assistance. Particular thanks for frequent help with the many long helium transfers is due Drs. Edward Wilson, Philip Marston, and John Philo. Ed also pitched to operate the helium liquifier on a couple of crucial occasions.

This thesis was very competently typed by Vicki LaBrie. The beautiful drawings are the work of Sylvia Harris. Bogar Tesszary provided important assistance in Xeroxing.

During portions of this work I held National Science Foundation and California State Fellowships. The research was supported in part by the Air Force Office of Scientific Research.

A special thanks goes to K for her continuing encouragement. Finally, I am tremendously grateful to my parents, Hazel and Raymond Lockhart, for their unfailing support of and interest in my scientific career throughout the years.

TABLE OF CONTENTS

		PAGE
ABSTRACT		iii
ACKNOWLEDGMENTS		vi
LIST OF FIGURES		xi
LIST OF TABLES		xiii
CHAPTER 1.	INTRODUCTION	1
CHAPTER 2.	AMBIENT ELECTRIC FIELDS INSIDE A VERTICAL METAL SHIELDING TUBE	7
	2.1 Introduction	7
	2.2 Patch Effect Fields	9
	2.3 Gravitationally-Induced Fields	17
	2.3.1 Theoretical Results	17
	2.3.2 Experimental Results	23
	2.4 Reconciliation of Witteborn-Fairbank Results with Theoretical Predictions and Results of Other Experiments	31
CHAPTER 3.	TECHNIQUE OF MEASUREMENT	35
	3.1 Introduction	35
	3.2 Effect of Drift Tube Potential Variations on the TOF Distribution	39
	3.2.1 Effect of a Linear Potential Gradient	40
	3.2.2 Effect of Random Potential Variations	41
	3.3 Electron Time-of-Flight Apparatus, 4.2°K Version	51
	3.3.1 Cryogenic and Vacuum Systems	53
	3.3.2 Cathode	55
	3.3.3 Beam Handling System	62
	3.3.4 Electrode Biasing Circuits	66

PAGE

3.3.5 Detector and Counting Electronics . . 74

3.3.6 Timing and Control Electronics . . . 77

3.4 Modifications for Room-Temperature and LN_2-Temperature Operation 79

3.5 Apparatus Modifications for Heated Drift Tube Experiments 80

3.5.1 Determination of the Thermoelectric Potential Gradient along the Drift Tube 86

3.6 Procedure 92

3.6.1 LHe Runs 92

3.6.2 Room Temperature and LN_2 Temperature Runs 93

3.6.3 Heated Drift Tube Experiments 94

CHAPTER 4. DATA AND ANALYSIS 96

4.1 Trapped Electrons 97

4.2 Room Temperature Results 101

4.3 77°K Data 113

4.4 First LHe Run 117

4.5 Heated Drift Tube Experiments 122

4.5.1 Nature of the Zero-Applied-Force TOF Distribution 123

4.5.2 Analysis of the Heated Drift Tube Data 129

4.5.3 Data at 4.2°K 133

4.5.4 Data at 4.3°K 142

4.5.5 Data at 4.3°K with Upward Applied Forces 148

4.5.6 Data at 4.4°K 152

4.5.7 Data with Upward Applied Forces at 4.4°K 152

4.5.8 Data at 6.3°K 156

PAGE

4.5.9 Data at 9°K 156

4.5.10 Data at 11°K 162

CHPATER 5. SUMMARY AND CONCLUSIONS 165

REFERENCES 173

LIST OF FIGURES

FIGURE		PAGE
2.1	A Completely Periodic Patch Distribution	13
3.1	View of the Upper Portion of the Apparatus	52
3.2	Cross-Section of the Apparatus	54
3.3	Schematic Diagram of a Tunnel Cathode	56
3.4	Tunnel Cathode Electron Energy Distribution	58
3.5	Schematic Diagram of the Electron Time-of-Flight Apparatus and the Electrode Biasing Circuitry . . .	63
3.6	Electric and Magnetic Field Profiles along the Electron Flight Path	65
3.7	Electron Injection System	67
3.8	Low-Noise Totally-Shielded Power Supplies for the Bias Circuits	72
3.9	LHe Bias Circuit Board	72
3.10	Superconducting Clamps and Feedthroughs	75
3.11	Detector and Counting Electronics	76
3.12	Control Electronics	78
3.13	Cross-Section of the Drift Tube Area	82
3.14	Thermal Decay Curves for the Drift Tube	88
4.1	A Representative Room Temperature TOF Spectrum . .	103
4.2	A Full Logarithmic Plot of the Initial Portion of the TOF Distribution of Fig. 4.1	104
4.3	Room Temperature TOF Spectra Taken with Applied Forces	106
4.4	Summary of Room Temperature Results	110
4.5	A Linear Plot of Room Temperature Results	111
4.6	TOF Spectra at 77°K	114
4.7	A Full Logarithmic Plot of a 77°K TOF Spectrum . .	116
4.8	TOF Spectra at 4.2°K	118

FIGURE		PAGE
4.9	Summary of Results from the First 4.2°K Run	120
4.10	A Full Logarithmic Plot of a 4.2°K TOF Distribution Obtained During the Heated Drift Tube Experiments	124
4.11	The Latter Portion of the TOF Distribution of Fig. 4.10	125
4.12	4.2°K TOF Spectra Taken at Four Values of Residual Gas Pressure	126
4.13	Observed Force Results at 4.2°K	137
4.14	Scatter Analysis Plot of 4.2°K Data	139
4.15	Observed Force Results at 4.3°K	145
4.16	Scatter Analysis Plot of 4.3°K Data	147
4.17	Observed Force Results at 4.3°K Obtained with Upward Applied Forces	149
4.18	Observed Force Results at 4.4°K	154
4.19	Observed Force Results at 4.4°K Obtained with Upward Applied Forces	155
4.20	Observed Force Results at 6.3°K	158
4.21	Scatter Analysis Plot of 6.3°K Data	159
4.22	Observed Force Results at 9°K	161
4.23	Observed Force Results at 11°K	164
5.1	Summary of the Ambient Force Results for the Four Lowest Values of Temperature	166
5.2	Summary of the Ambient Force Results	167
5.3	Summary of Ambient Force Results Obtained by Ratioing Zero-Applied-Force Spectra Taken at Different Temperatures	170

LIST OF TAB

TABLE

2.1	Compilation of Strain-Induced Field Results . . . . .
3.1	Temperature Monitor Resistor
4.1	4.2°K Data from the Heated Dr Experiments . . . . .
4.2	4.2°K Observed Force Values .
4.3	4.3°K Observed Force Values .
4.4	4.4°K Observed Force Values .
4.5	6.3°K Observed Force Values .
4.6	9°K Observed Force Values . .
4.7	11°K Observed Force Values .
5.1	Ratios of TOF Spectra Taken a Temperatures to a 4.2°K TOF S

CHAPTER 1

INTRODUCTION

This dissertation describes a series of experiments which were performed in order to search for a temperature dependence in the ambient axial electrostatic potential variations inside a vertical copper tube. A vertical metal tube subject to the gravitational field of the Earth is expected to have spatial variations in the electrostatic potential along its axis because of several mechanisms which cause the walls of such a tube to depart from the normal uniform charge distribution found in a single metallic crystal not in a gravitational field. One mechanism results from the fact that a macroscopic metal tube is composed of very many small crystals which, because of their differing work functions, develop contact potential differences from one crystal to the next in order to achieve a single electrochemical potential throughout the entire metal. The presence of the Earth's gravitational field produces two effects. First, the center of mass of the conduction electrons in the walls of the tube is shifted downward a small but finite amount (approximately 10^{-31} m), resulting in a downward electric field in the metal of mg/e, where m is the electron mass. This field must exist in the metal if the conduction electrons are to be in equilibrium in the presence of a downward gravitational field of magnitude g. The existence of this field was first predicted by Schiff and Barnhill in 1966.[1] Second, gravity causes a differential compression of the ionic lattice of the walls. The metallic electrons redistribute in an effort to maintain charge neutrality throughout the metal; however, the

cancellation of the positive charge density gradient is not complete because of the finite compressibility of the electron gas (we are using a very simple model of the metal; however, the conclusions are the same as those obtained from a rigorous treatment). The result is an upward electric field in the metal of magnitude roughly Mg/e where M is the ion mass. The existence of a field of approximately the same value outside the surface of the metal was first predicted in 1967 by Dessler, Michel, Rorschach, and Trammel.[2] We will explore these ideas more completely in Chapter 2.

Interest in the nature of the ambient electrostatic potential variations along the axis of a copper tube was stimulated by the 1967 experiment of Witteborn and Fairbank[3] which measured the force of gravity on a single electron by means of a time-of-flight technique. Two aspects of the results of that experiment did not agree with the theoretical predictions concerning the ambient potential variations to be found along the axis of the copper tube employed as an electrostatic shield in the time-of-flight measurements. First, it proved possible to control the distribution of electron flight times by the use of applied fields in the copper tube as small as 2.5×10^{-11} V/m. In particular, it was possible to turn back the slowest electrons in the beam by applying these very small fields. Such a result is not compatible with the expected patch effect potential fluctuations, which on the most straightforward model can have rms values as large as 10^{-6} V or so. We show in Sec. 3.2 that any electrons which could pass through a region having potential fluctuations of this size would have their flight times modified only infinitesimally by a field of 2.5×10^{-11} V/m applied over a 1-m

flight path. Specifically, the applied field would not be able to turn back such electrons. Second, the electron gravity measurement indicated that the only forces larger than 5×10^{-12} eV/m acting on an electron traveling along the axis of the copper tube were gravity and a force due to the field predicted by Schiff and Barnhill. The 10^{-7} eV/m force predicted on the basis of the ion lattice distortion was not observed.

Considerable controversy arose concerning the proper reconciliation of the results of the Witteborn-Fairbank experiment with the theoretical predictions about the ambient potential fluctuations inside the shielding tube. Other workers conducted a variety of experiments to search for the existence of a lattice distortion field both inside and just outside a metal subject to a compression gradient (see Sec. 2.3.2). These experiments verified the order of magnitude predictions of the theory. It must be pointed out however that these experiments were conducted under conditions quite different from those of the Witteborn-Fairbank experiment. One of the more obvious differences is the temperature: Witteborn and Fairbank worked at 4.2°K in order to make use of superconducting magnets and circuitry while all other experiments to date which look at the lattice distortion field outside a metal have been done at room temperature. Witteborn and Fairbank,[3,4] among others,[5,6] suggested that a surface shielding effect occurring at low temperatures might have shielded the interior of the copper tube from fields arising in the walls of the tube. Assuming that the charge responsible for the surface shielding is provided by electrons in a layer which is decoupled from both the strain gradient and the electron distribution present in the tube

walls, the patch effect and lattice distortion fields would not appear along the tube axis, while the Schiff-Barnhill field produced by the surface electrons would be present. This situation would agree completely with the results of the Witteborn-Fairbank experiment.

If a surface shielding effect of the type described exists at 4.2°K, it presumably does not exist at room temperature since there was no evidence of its presence in the room temperature experiments which studied the lattice distortion field; it would thus be a temperature-dependent shielding effect. We felt that by conducting electron time-of-flight experiments at temperatures from 4.2°K to room temperature we could determine whether or not such a temperature-dependent surface shielding effect exists and if so, the range of temperatures over which it is operative. That line of reasoning provided the motivation for the experiments described in this dissertation.

The initial phase of our search for a temperature-dependent surface shielding effect consisted of using a modified version of the Witteborn-Fairbank apparatus (described in Chapter 3) in an attempt to determine the room temperature ambient potential fluctuations in the copper tube. This work was followed by a similar measurement at liquid nitrogen temperature. The room temperature and LN_2 temperature measurements (described in Secs. 4.2 and 4.3) indicated that any onset of anomalous surface shielding would occur below LN_2 temperature. After conducting a 4.2°K run to verify the existence of the shielding effect at that temperature (described in Sec. 4.4), we designed a low-power drift tube heating and temperature monitor system which

made possible experiments in which the drift tube operated at temperatures from 4.2°K up to 30-40°K while the other components of the apparatus remained at 4.2°K. The heated drift tube apparatus is described in Sec. 3.5 while the results appear in Sec. 4.5. This mode of operation has the great advantage of permitting the use of superconducting magnets and circuitry as well as cryopumping. The ability to use these techniques results in a factor of 10^4 improvement in sensitivity over the version of the apparatus employed at 300°K and 77°K.

As shown in Chapters 4 and 5, the results from experiments conducted with the drift tube temperature ranging from 4.2°K to 11°K indicate that there is a surface shielding effect at 4.2°K; the effect is greatly weakened when the temperature is increased by only 0.1°K and is either non-existent or else extremely small above 6°K. The ambient electric field observed in the tube above 6°K agrees well with the predictions of Dessler, Michel, Rorschach, and Trammel for the magnitude of the lattice distortion field. It seems that the patch effect fluctuations are at least an order of magnitude or so smaller than expected on the basis of commonly accepted models. The suggestions that the use of a 4.2°K operating temperature for the electron free fall experiment may have been crucial to its success thus appear to be borne out by the results of our work.

Section 2.4 explores some of the requirements for a surface state which would provide the necessary shielding. A few of the mechanisms which have been suggested in order to explain the apparent shielding at 4.2°K are also presented in that section; in general they do not predict a temperature dependence in the shielding. In

Chapter 5, after summarizing our conclusions concerning the temperature-dependent shielding, we discuss a few possible models in which a temperature dependence similar to that observed might be expected.

CHAPTER 2

AMBIENT ELECTRIC FIELDS INSIDE A VERTICAL METAL SHIELDING TUBE

2.1 Introduction

In this chapter we will discuss the theoretical and experimental results to date concerning the nature of the small electric fields present in the interior space of a copper shielding tube oriented vertically in the Earth's gravitational field. Much of the interest in this question was stimulated when Witteborn and Fairbank[3] began an experiment to measure the force of gravity on a single electron by making time-of-flight measurements on very low energy electrons emitted from a pulsed cathode (the ultimate aim of the experiment is to study the force of gravity on antimatter). Since the force of the Earth's gravity on a single electron is so incredibly small (the same value of force would be exerted on the electron by an electric field of 5.6×10^{-11} V/m) it was clear that the portion of the electron's trajectory over which the flight time was to be measured would have to be enclosed by a very good electrostatic shield.

Witteborn and Fairbank[3] used a very carefully made 91-cm long vertical copper drift tube having a very uniform inside diameter (5 cm with variations less than 0.0003 cm). Electrons were constrained to move along the axis of the drift tube by an axial magnetic field provided by a superconducting solenoid operating in the persistent mode.

When an electron is exactly at the midpoint of the tube axis, it feels no axial force from its image charge (the net radial image force

is always zero as long as the electron is on the tube axis). When the electron is on either side of the midpoint there is a small image force contribution due to the finiteness of the tube length. However, this field, as well as fields from electrodes located outside the tube, is attenuated by the drift tube approximately as $\exp(-2.4z/a)$ where z is the distance from the nearer end and a is the tube radius.

Witteborn[4,7] has performed a detailed calculation of the residual electric field in the drift tube when the attenuation properties described above are applied to the specific case of the dimensions and electrode potentials utilized in the electron free fall experiment. His results indicate that the drift tube provided a region of space approximately 50 cm long that was adequately shielded from both external potentials and the fields of image charges induced when an electron was present in the region. However, this calculation was not intended to take into account the electric fields which were expected from the walls of the tube itself even when no electron is present in the interior region. We expect two types of such fields.

First, the copper tube used by Witteborn and Fairbank is composed of many small crystals. Contact potential differences between adjacent crystals give rise to so-called "patch effect" fields outside the surface of the metal. Second, the effect of the Earth's gravity on the walls of the drift tube produces electric fields outside the surface of the metal. We will discuss each of these effects separately in the following sections.

2.2 Patch Effect Fields

A spatially fluctuating electric field is found outside the surface of a polycrystalline metal because of the differences in the work functions of the various crystallite planes exposed at the macroscopic surface. Following the approach used by Herring and Nichols in their very comprehensive article on thermionic emission,[8] we define the electrochemical potential per electron of crystallite i by the equation

$$\bar{\mu}_i = [\partial F/\partial n_i]_{\text{all T's, other n's, etc.}} \tag{2.1}$$

with the free energy F given by $F = U - \sum_j T_j S_j$, where U is the total energy of the macroscopic metal, T_j and S_j refer to the temperatures and entropies of the various crystallites, and n_i is the number of electrons in crystallite i. The usefulness of this quantity stems from the fact that the electrochemical potentials of the electrons in any two regions 1 and 2 in thermal equilibrium with each other must be equal. We can now define the work function $e\phi$ of a uniform surface of an electronic conductor as the difference between the electrochemical potential $\bar{\mu}$ of an electron just inside the conductor and the electrostatic potential energy $-e\Phi_a$ of an electron in the vacuum just outside it. Thus

$$e\phi = -e\Phi_a - \bar{\mu} = e(\Phi_c - \Phi_a) - \mu \pm \begin{pmatrix}\text{potential terms}\\ \text{from other}\\ \text{external forces}\end{pmatrix} \tag{2.2}$$

where in the second part of the equality we have introduced Φ_c, the electrostatic potential of an electron in the conductor, and μ, the

ordinary chemical potential (Fermi level) related to $\bar{\mu}$ by

$$\bar{\mu} = \mu - e\Phi_c \pm (\text{potential terms from other external forces}). \qquad (2.3)$$

Let us now investigate the ramifications of the definition (2.2) for the work function of each crystallite when the various crystallites are assembled to form the macroscopic block of metal. When the electrochemical potentials of the electrons in the various crystallites are set equal we see that there must be a difference in electrostatic potential between a point just outside crystallite 1 and a point just outside crystallite 2 given by the difference of the two work functions:

$$\Phi_{a1} - \Phi_{a2} = \phi_2 - \phi_1 \, . \qquad (2.4)$$

This is called the "contact potential difference" between 1 and 2.

One may view the latter part of Eq. (2.2) as a resolution of the work function into two components: a volume term μ and a surface term $e(\Phi_c - \Phi_a)$. The volume term will vary from one crystallite to another depending on the crystallite size, imperfection density, etc., while the surface term will depend on the type of crystal plane which forms the surface (it will also be affected by any surface contamination).

Contact potential differences of a few tenths of a volt are expected between different grains of a copper surface. The work function of the 100 surface of a single copper crystal has been measured[9] and found to be about 4.8 V, while measurements on the 111 surface of a bulk sample gave a work function of 4.9 V.[10] The

work function of the 100 surface of an evaporated copper film was measured at 4.5 eV.[11]

Witteborn[4] has shown that, assuming a random distribution of patches of characteristic dimension a having electrostatic potentials just outside their surfaces of either + 0.1 V or - 0.1 V, the spatial variations in potential at a distance r above the composite surface may be estimated by

$$\Delta\Phi = 0.06\ (a/r)\ \text{eV} . \qquad (2.5)$$

For the case of the drift tube used in the Witteborn-Fairbank free fall experiment we have r = 2.5 cm; also, the assumption of + 0.1 V and - 0.1 V patch potentials should be a close approximation to the actual situation. The characteristic patch diameter, however, is a bit more difficult to ascertain. The drift tube was fabricated by electroforming copper onto an aluminum mandrel polished to a mirror finish; the mandrel was later dissolved away using KOH. The resulting surface was lightly etched with a mixture of nitric and phosphoric acid. This procedure was believed to produce a surface having very small crystallites. Examination of the drift tube surface with conventional optical metallographic techniques indicated that the crystallites were less than 1 micron in diameter.[12] Using this value in Eq. (2.5) we obtain

$$\Delta\Phi = 0.06\ \left(\frac{10^{-4}\ \text{cm}}{2.5\ \text{cm}}\right) = 2.4\times10^{-6}\ \text{eV} .$$

This result is too large by several orders of magnitude to be consistent with the results of the Witteborn-Fairbank experiment. Witteborn and Fairbank found that applied electric fields in the

drift tube as small as 2.5×10^{-11} V/m produced a significant effect on the electron time-of-flight distribution. This would seem to constitute an approximate experimental limit on the magnitude of random fluctuations in potential along the drift tube axis since potential fluctuations much larger than this value would totally mask the effect of the applied field.

The above calculation of patch effect potential fluctuations along the drift tube axis assumes total randomness in the distribution of patches. Much different results are obtained if some form of ordering is present in the patch distribution. For example, Herring and Nichols[8] have worked out the potential $\Phi(xyz)$ at a distance z above an xy plane which has its various types of patches recurring periodically with period X in the x direction and Y in the y direction:

$$\Phi = \overline{\Phi} + \sum_{m=1}^{\infty} \sum_{n=1}^{\infty} \{[a_n \sin(2\pi nx/X) + b_n \cos(2\pi nx/X)] \times [c_m \sin(2\pi my/Y) + d_m \cos(2\pi ny/Y)] \times \exp[-2\pi z(n^2/X^2 + m^2/Y^2)^{1/2}]\} . \quad (2.6)$$

If we assume a "checkerboard" distribution of + 0.1 V and - 0.1 V patches as shown in Fig. 2.1 then with the choice of origin indicated in the figure, Eq. (2.6) becomes

$$\Phi(xyz) = \overline{\Phi} + \sum_{m=1}^{\infty} \sum_{n=1}^{\infty} \{[a_{nm} \sin(2\pi nx/X) \sin(2\pi my/Y)] \times \exp[-2\pi z(n^2/X^2 + m^2/Y^2)^{1/2}]\} , \quad (2.7)$$

where a_{11} = 0.1 V and all other a's are zero. Inserting these values

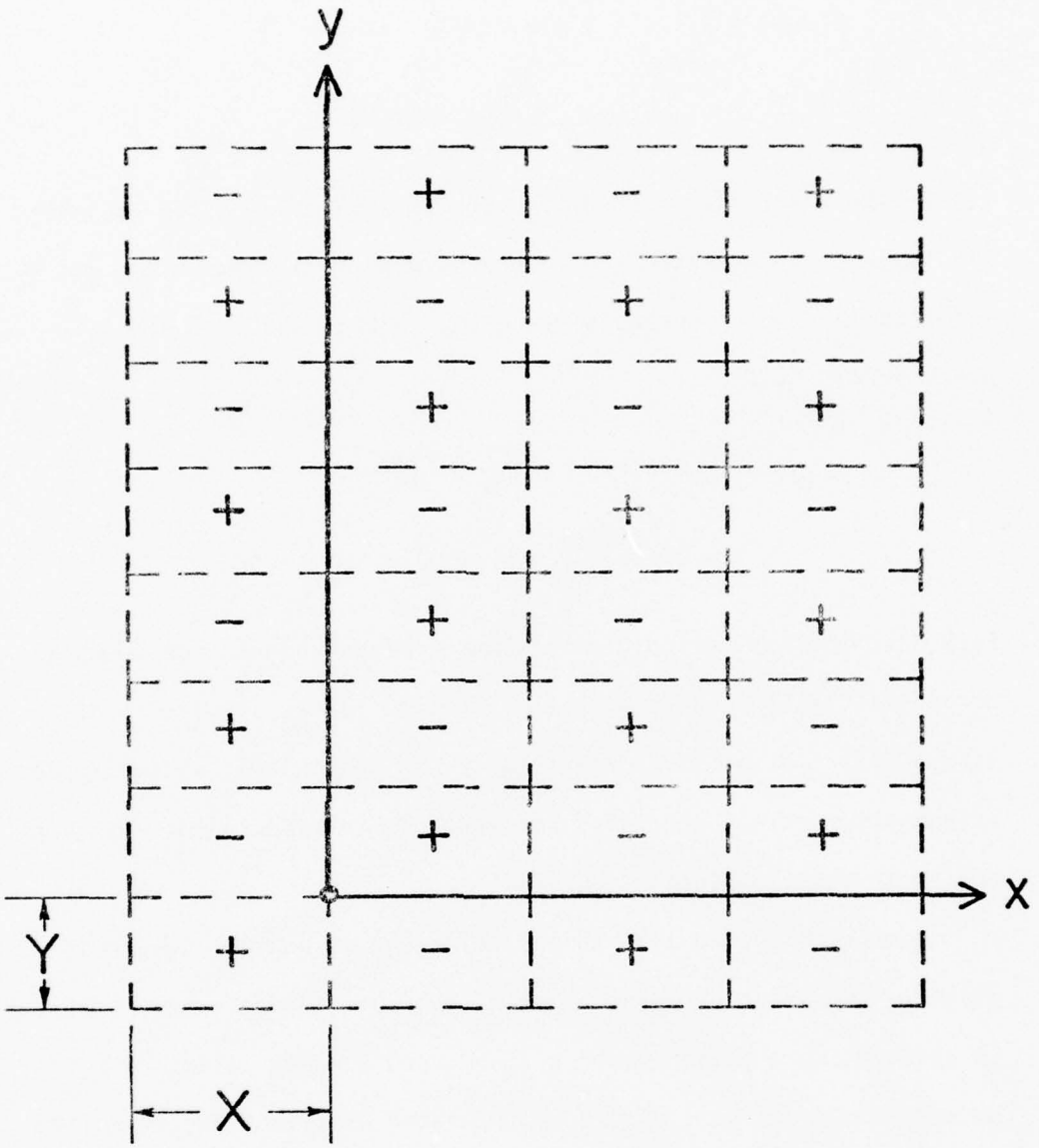


Fig. 2.1. A completely periodic patch distribution at a surface.

for the a_{nm} and taking X = Y we obtain:

$$\Phi(xyz) = \overline{\Phi} + 0.1\ V \sin(2\pi x/X) \sin(2\pi y/Y) \times \exp\left[-2\pi z \frac{\sqrt{2}}{X}\right] . \qquad (2.7)$$

If we take z = 2.5 cm (the drift tube radius) and X = 0.1 cm (about the largest patch period that could be expected) then we can calculate the maximum potential fluctuation in the tube produced by patch effect fields:

$$\Phi_{max} - \overline{\Phi} = 0.1 \exp\left[\frac{-2\pi(2.5\ cm)\sqrt{2}}{0.1\ cm}\right] V$$

$$= 0.1\ e^{-221}\ V \cong 10^{-82}\ V .$$

Such a completely periodic distribution of patches is, of course, not at all likely. However, as Witteborn[4] points out, it is of interest to see just how dramatically one can change the magnitude of the patch effect potential gradients by introducing ordering into the patch distribution.

A much more plausible form of ordering is nearest-neighbor ordering, in which each patch having a higher than average potential is adjacent to a patch having a lower than average potential. We do not demand any periodicity in the patch distribution; we merely require that the patches always occur in positive-negative pairs. Madey[13] has performed a calculation which is applicable to such a situation, since nearest-neighbor ordering is expected to produce the nearly sinusoidal potential auto-correlation function which is central to his argument. For the case of the drift tube used in the electron free fall experiment, Madey finds an rms potential

fluctuation

$$\Delta\Phi = 5.6 \times 10^{-12} \text{ V} ;$$

this value is essentially consistent with the Witteborn-Fairbank results.

As we mentioned earlier, surface contamination is capable of greatly modifying patch effect fields. While care was taken to avoid gross contamination of the surface of the free fall drift tube, contamination at the microscopic level was most certainly present. First, we would expect an oxide layer of 20 Å or so[14] since the drift tube was exposed to air for several days before it was placed in the high vacuum environment of the apparatus. The tube was baked out at 100°C for several hours after it was placed in the apparatus vacuum; however, this process primarily desorbs H_2O without having an appreciable effect on the CuO layer. Other adsorbed gases are also expected to be present, both as a result of the initial exposure to air and as a result of additional adsorption of residual gas when the apparatus is cooled. In particular, under the operating conditions of the Witteborn-Fairbank experiment the primary residual gas in the vacuum chamber which encloses the drift tube is He, mainly because the ion pump employed pumps He least efficiently. Since it has been determined in direct experimental studies[15] that He adsorbs on copper to a quite significant extent at 4.2°K, we would expect some additional adsorption of He on the walls of the Witteborn-Fairbank drift tube upon cooling the apparatus to 4.2°K. Since gas adsorption is observed to occur preferentially on certain crystallites of a

polycrystalline metal,[8] some smoothing of contact potential variations might be expected from such adsorption.

Direct experimental studies of contact potential variations along metal surfaces under various surface conditions,[16,17] including a study of the effect of various degrees of oxidation on the contact potential variations,[18] show large changes in contact potential with changes in surface conditions. However, these results do not seem to imply that contact potential differences in polycrystalline copper would be reduced much below 0.1 V by adsorbed gas smoothing.

Thus it appears that if one makes the customary assumption of randomness in the patch distribution on the walls of the Witteborn-Fairbank drift tube, axial potential variations of about 10^{-6} V should be present. The ability of Witteborn and Fairbank to pass 10^{-11} eV electrons through their drift tube is quite remarkable. Although we have seen how nearest-neighbor ordering can greatly reduce the potential fluctuations along the drift tube axis, it is not clear that there is any reason to believe that the electroforming fabrication process would lead to such nearest-neighbor ordering. The Witteborn-Fairbank results strongly suggest the presence of a surface shielding layer on the drift tube walls. Such a shielding layer would most likely involve electron states based on the surface layer of copper oxide although adsorbed gas might also have a small effect on the nature of possible electron states. The effects of adsorbed gas are assumed to be small since (as we will show in Chapter 4) the surface shielding layer appears to become inoperative above 9°K or so, while the change in the amount of adsorbed gas between 4.2°K and 9°K amounts to much less than a monolayer. We will say more about possible

surface shielding mechanisms later in this chapter when we discuss the shielding of gravitationally-induced electric fields in the drift tube.

2.3 Gravitationally-Induced Fields

Gravitationally-induced electric fields in metals were in a sense first studied in the Tolman-Stewart electron-inertial effect experiment.[19] In the electron-inertial experiments a conductor is accelerated and the resulting current in the conductor is measured (Tolman and Stewart rapidly decelerated a rotating coil of wire). Since we know from the equivalence principle of general relativity that a conductor in a gravitational field is equivalent to an accelerated conductor, a conductor placed in a gravitational field ought to develop an internal electric field.

The electric field induced in a metal by the action of gravity can be viewed as a special case of the more general phenomenon of a stress-induced shift in the work function of a metal. Gravity induces a stress gradient in a metal, thus giving rise to an electric field equal to the resulting work function gradient.

Stress-induced work function shifts in general and gravitationally-induced electric fields in particular have been investigated by several theorists and experimentalists during the last few years. We will look first at the theoretical results and then turn to a consideration of the experiments.

2.3.1 Theoretical Results

The electric field outside a conductor placed in a gravitational field was first calculated by Schiff and Barnhill[1] in 1966. They

approached the problem by first considering a test charge placed at an interior point along the axis of a vertical metal tube not subject to gravity and finding the consequent arrangement of the lattice and the electron gas of the metal and the resulting modified Hamiltonian for the interacting electrons and nuclei of the metal. A reciprocity relation was then employed to show that the electric field along the axis of the tube is proportional to the gradient of this modified Hamiltonian with respect to the position of the test charge. In this way they obtained a relation between the gravitationally-induced charge rearrangement in the tube and the electric field along the tube axis. For the case of a vertical copper tube in the earth's gravitational field they obtained the result $E = -mg/e$ where the minus sign indicates a downward field and m is the electron mass. This would imply that an electron traveling along the axis of the tube would feel zero net force since the electron field from the tube walls would just balance the force of gravity on the electron.

A later calculation by Dessler, Michel, Rorschach, and Trammel (DMRT)[2] showed that Schiff and Barnhill (SB) had in effect failed to take into account properly the distortion of the metal lattice caused by its own weight. By considering the effects of the differential lattice compression, DMRT obtained a result for the gravitationally-induced electric field outside copper which is larger than the SB estimate by about four orders of magnitude and has the opposite direction.

As we mentioned earlier, SB used reciprocity to calculate the gravitationally-induced field from the shift in the center of mass

of the tube produced by the motion of a test charge. They ascribed a negligible value to the effect of the test charge on the lattice since they assumed that the lattice charges would be almost completely shielded from the test charge field by the metallic electrons. However, this is not the case. When one looks at the details of the electron density distribution at the surface of the metal in the presence of the test charge and the way in which this distribution changes as the test charge is moved it turns out that there is a significant coupling between the test charge and the lattice. The way in which the test charge affects the lattice is described in the excellent and comprehensive paper by Herring.[20] Herring also shows how under the proper assumptions the SB approach leads to the same value for the gravitationally-induced field as that obtained by DMRT. In a second paper on the topic, Schiff[21] acknowledged the correctness of Herring's treatment.

The basic approach used in the DMRT calculation is to calculate the field inside the metal by making use of the fact that the electrochemical potential must be constant throughout the metal under conditions of thermodynamic equilibrium. The internal field is proportional to the work function gradient in the metal and as we saw in Sec. 2.2 a work function gradient in the metal can be related to an electric field outside the metal. However, the determination of the external field is much less precise than our knowledge of the internal field since surface effects greatly modify the value of the external field.

In Sec. 2.2 we wrote the electrochemical potential in a conductor as

$$\bar{\mu}(\underset{\sim}{r}) = \mu(\underset{\sim}{r}) - e\Phi_c(\underset{\sim}{r}) \pm (\text{potential terms from other external forces}) \qquad (2.3)$$

where $\mu(\underset{\sim}{r})$ is the Fermi level at $\underset{\sim}{r}$ and $\Phi_c(\underset{\sim}{r})$ is the electrostatic potential at point $\underset{\sim}{r}$ in the conductor. In this case the external force we are considering is the force of gravity on the electrons so the electrochemical potential becomes

$$\bar{\mu}(\underset{\sim}{r}) = \mu(\underset{\sim}{r}) - e\Phi_c(\underset{\sim}{r}) - m\underset{\sim}{g}\cdot\underset{\sim}{r} = \text{const.} \qquad (2.8)$$

where in making the second equality we have assumed thermodynamic equilibrium. Thus the internal field is given by

$$E_i = -\,\text{grad}\,\Phi_c = \frac{m\underset{\sim}{g}\cdot\hat{\underset{\sim}{r}}}{e} - \frac{1}{e}\,\text{grad}\,\mu \qquad (2.9)$$

where $\hat{\underset{\sim}{r}}$ is the unit vector in the $\underset{\sim}{r}$ direction.

We consider a cylinder oriented along the z-axis, which we take to be anti-parallel to $\underset{\sim}{g}$. Then $\underset{\sim}{g}\cdot\underset{\sim}{r} = -g$ and we have

$$\underset{\sim}{E}_i = E_{iz} = -\frac{my}{e} - \frac{1}{e}\,\frac{\partial\mu}{\partial u_{jk}}\,\frac{\partial u_{jk}}{\partial z} \qquad (2.10)$$

where u_{jk} is the strain tensor and the summation convention is employed. Since the only non-zero component of the stress tensor σ_{jk} is

$$\sigma_{zz} = -\rho g(h - z) = \rho g(z - h) \quad 0 \leq z \leq h \qquad (2.11)$$

where ρ is the mass density of the metal and h is the height of the cylinder, we have[22]

$$u_{zz} = \frac{\rho g(z-h)}{E_y} \qquad (2.12)$$

$$u_{xx} = u_{yy} = -\frac{\sigma}{E_y}\ \rho g(z - h) \tag{2.13}$$

where E_y is Young's modulus for the metal, σ is Poisson's ratio, and all other u_{jk} are zero. Then using[23]

$$\mu = \frac{\hbar^2}{2m}\ (3\pi^2 n)^{2/3} \tag{2.14}$$

and the relation

$$\frac{d\mu}{du_{zz}} = \frac{d\mu}{(dV/V)} = -\frac{d\mu}{(dn/n)} \tag{2.15}$$

where dV/V is the deformation produced by the change of strain du_{zz} and n is the number of conduction electrons per unit volume, we have

$$\frac{d\mu}{du_{zz}} = -\frac{2}{3}\mu\ . \tag{2.16}$$

Thus

$$E_{iz} = -\frac{mg}{e} + \frac{1}{e}\left(\frac{2}{3}\mu\right)\frac{\rho g}{E_y}(1 - 2\sigma)$$

$$= -\frac{mg}{e} + \frac{1}{e}\left(\frac{2}{3}n_0\mu\right)\frac{Mg}{E_y}(1 - 2\sigma) \tag{2.17}$$

where n_0 is the unstrained electron number density and M is the mass of a lattice ion.

For copper we have[24] $E_y/(1-2\sigma) = 4 \times 10^{12}$ erg/cm^3 and[25] $n_0\mu = 0.95 \times 10^{12}$ erg/cm^3; thus

$$E_{iz} \approx \frac{Mg}{e}\left(\frac{2}{3}\right)\left(\frac{0.95}{4}\right) \approx 0.15\ \frac{Mg}{e}$$

$$\approx 10^{-6}\ \text{V/m}\ . \tag{2.18}$$

This is about four orders of magnitude larger than the SB result and has the opposite direction.

Actually DMRT quote their result for the internal field as

$$E_z = (g/e)\ [\gamma M - m] \tag{2.19}$$

where they use γ to represent essentially the ratio of the elasticity modulus of the electron gas to that of the bulk metal. Their estimate of a γ based on a free-electron model of 1/7 for copper is basically the same as the effective estimate of γ we have used in Eq. (2.18). They also give an approximate estimate for γ of 0.085 based on an expression for μ due to Wigner and Bardeen[26] which should more nearly represent the actual situation.

The DMRT calculation predicts the internal field in the metal caused by a strain gradient; the external field, of course, will depend on the exact surface conditions which prevail, just as in the case of the patch effect fields. The external field will be the same as the internal field only for an "ideal" surface.

As we mentioned previously, Herring obtained a similar result using the SB method by carefully considering the role of surface stress in allowing a test charge to couple to the ion lattice. Calculations of the gravitationally-induced field have also been performed by, among others, Peshkin and Rieger. Peshkin[27] used the Thomas-Fermi model to determine the internal field in the metal; he obtained essentially the DMRT result. However, he also presented an argument which suggested that the external field would have approximately the value originally predicted by SB. His argument assumed a high degree of shielding provided by the conduction electrons very near the surface.

However, a later calculation by Schiff[28] indicated that this high degree of shielding is not present.

Rieger[29] calculated the internal gravitationally-induced field in several metals from the electron-phonon interaction. He obtained a value of 4×10^{-6} V/m for copper, although he comments that the field may well be an order of magnitude smaller if the electron-phonon coupling constant is determined from ultrasonic attenuation data (more nearly related to the case of gravitationally-induced lattice distortion) rather than from resistivity data.

Thus it seems that the theorists are now in basic agreement that, barring unusual surface shielding effects, an electric field of about 10^{-6} V/m should exist along the axis of a vertical copper tube. We will discuss in Sec. 2.4 (and again in Chapter 5) some of the possible surface shielding mechanisms which could yield a much smaller value of axial electric field under the conditions of the Witteborn-Fairbank experiment.

2.3.2 Experimental Results

As we have mentioned earlier, the Witteborn-Fairbank (WF) experiment found the ambient electric field along the axis of a vertical copper drift tube to have, within 10% or so, just the value first calculated by Schiff and Barnhill, -5.6×10^{-11} V/m. This result was obtained with a residual gas pressure of $10^{-11} - 10^{-12}$ Torr and a drift tube temperature of 4.2°K. The upward electric field of 10^{-6} V/m predicted by DMRT was somehow reduced below 5×10^{-12} V/m outside the surface of the copper tube.

This surprising discrepancy between a carefully performed experiment and a generally accepted theory has motivated several

experimenters to conduct experiments in which the strain-induced electric field outside a metal surface could be directly measured. In all such experiments to date strain gradients have been produced in a metal by some means other than the action of the Earth's gravity. However, this in itself should not be important since strain gradients should be equally effective in producing electric fields in the metal regardless of their origin. Also, many of the experiments employed strains several orders of magnitude larger than those present in the WF experiment; this difference is of more concern in making comparisons of results than the origin of the strain. The conditions of vacuum and temperature varied greatly from one experiment to the next.

Beams[30] used capacitive probes to measure the electrostatic potential at several different radial positions above a spinning aluminum cross. The experiment was conducted at room temperature with a background pressure of about 10^{-6} Torr. The rotor turned at 650 rps, producing an acceleration at its circumference of 10^5 g. Since there was a tensile strain whose magnitude increased with the distance from the rotation axis, a sizeable contact potential difference was expected between the axis and points near the circumference of the rotor. Beams indicates that his results agree substantively with the DMRT predictions (he does not quote quantitative results). He cites the presence of sizeable fluctuations in the data resulting from differences in residual gas bombardment of the rotor and in surface contamination.

Experiments in which uniform deformations were produced in a range of metals were performed by Craig[31] and by French and Beams.[32]

In these experiments Kelvin-type (vibrating electrode) probes were used to measure the contact potential difference between the reference electrode and the sample as a function of the stress applied to the sample. Both sets of experiments were conducted at room temperature and atmospheric pressure. In both cases the results were in good agreement with the predictions of the DMRT theory, although again considerably fluctuations were present. In particular, French and Beams found that the contact potential shift for copper could have either sign, depending on whether the sample was annealed or work hardened. Also, they found that a shift in the sign of the effect for annealed samples would occur when the sample was stressed to the point of plastic flow.

An experiment which closely simulated the small non-uniform compression gradient of the WF experiment was conducted by Guptill,[33] who mechanically accelerated copper tubes and measured the resulting change in the contact potential between exterior points with capacitive probes. The experiments were conducted at room temperature under atmospheric pressure. He obtained results which are consistent with the DMRT theory if their parameter γ is taken to be 0.1 (he obtained an experimental γ of 0.10 ± 0.01). Such a value of γ is intermediate between the two estimates provided by DMRT first on the free-electron model and then on the Wigner-Bardeen model. Guptill of course measured the external contact potential difference while the DMRT result applies directly only to the internal strain-induced field. The extent of the agreement between his results and the DMRT value is thus surprising.

Guptill's experiment is especially interesting in that he was able to measure separately the DMRT and the SB contributions to the acceleration-induced electric field (although the internal field from the SB effect is measured in contrast to the external measurement of the field from the DMRT effect). The SB effect is capable of serving as a source of emf; in particular, if a metal cylinder is caused to undergo an acceleration which varies sinusoidally, a sinusoidal current at the same frequency will be induced in a wire which connects the ends of the cylinder. Because there is no strain gradient along the connecting wire (any strain in the cylinder drops to zero at the junction of the cylinder and the connecting wire), no DMRT field will exist along it and hence no current (other than perhaps a small transient current) will flow in the wire as a result of the DMRT field in the cylinder. Guptill obtained exactly the predicted value for the SB field with an uncertainty of 5%.

Another experiment which employed a mechanically accelerated metal sample monitored with a capacitive pickup was performed by Brown[34] et al. The results of that experiment for the case of copper are smaller than Guptill's results by a factor of about 20 (only the external field from the DMRT effect was measured).

Enga[35] has made a careful study of five different mechanisms which can produce a strain-dependent potential on a metal surface. In particular, he points out the importance of the anisotropy in the deformations of the various crystal grains in a polycrystalline sample subject to stress (the variety of types and orientations of crystal face junctions in a polycrystalline metal results in a highly anisotropic stress tensor within the metal when a unidirectional

stress is applied to the bulk sample). To quote from Enga's paper: "Those crystallites strained in their hard direction will change their exposed surface area relatively less than those strained in their easy directions. The different crystal faces exposed have different work functions; hence, the relative change of area under [a] Kelvin probe of these faces can lead to a large signal [for the strain-induced potential shift] for a relative change of area of only about 10^{-4}." He suggests, on the basis of experiments reported in his paper, that the anisotropic elastic strain effect could be as large as ± 250 μV $(kgf/mm^2)^{-1}$ depending on the nature of the copper sample. In terms of the measurement of the gravitationally-induced external electric field in copper this translates to a possible variation of $\pm 2.2 \times 10^{-6}$ V/m in the observed field; i.e., a possible variation slightly larger than the expected magnitude of the DMRT field. The anisotropic elastic strain effect may help explain at least a portion of the variation in the results of different experiments on the magnitude of the strain-induced field outside copper.

A completely different technique was employed by Goldstein et al.[36] to measure internal strain-induced electric fields in aluminum. They applied compressional acoustic waves to Al-Pb superconducting tunnel junctions in such a manner as to produce a compressional strain gradient in the Al. By the DMRT theory this strain gradient results in an electric field in the Al; Goldstein et al. detected the electromagnetic waves induced by this field. They determined strain directly from the measured conversion efficiency of microwave power to acoustic power so that their results are quoted

in terms of the contact potential shift produced by a given strain. If we assume that the strain "s" referred to by Goldstein et al. can be related to an effective z-directed stress σ_{zz} by

$$\sigma_{zz} = [E_y/(1 - 2\sigma)]\, s \qquad (2.20)$$

then we can convert their result of a contact potential shift of 18 μV for an s value of $(1\text{-}2) \times 10^{-6}$ to the form of contact potential shift per unit stress. Taking a value of 2.4×10^{11} N/m^2 for $E_y/(1 - 2\sigma)$ for Al at about $2°K$[24] (the temperature used by Goldstein et al.), we find that their result becomes 0.375-0.75 mV $(kgf/mm^2)^{-1}$. If we convert this result to an effective gravitationally-induced electric field, we obtain the value $1\text{-}2 \times 10^{-6}$ V/m; this is approximately the result expected on the basis of the DMRT theory.

This experiment is the only one known to the author which actually measures the internal electric field predicted by DMRT; it seems to provide a nice verification of the correctness of their approach. Since the experiment does not look at the external strain-induced field, it does not provide any information about the possible role of low temperatures in the formation of surface states capable of shielding the outside of the metal from fields present in the bulk.

We present in Table 2.1 a summary of theoretical and experimental results on the work function shift produced when stress is applied to a metal. We include in the table values for both copper and aluminum. The table is not necessarily complete; however, all important results with which the author is familiar have been included.

TABLE 2.1

SUMMARY OF RESULTS ON THE WORK FUNCTION SHIFT OF A METAL SUBJECT TO STRESS[a]

Investigator	Method	Stress Level (kgf/mm^2)	Temperature (°K)	Result ($\mu V(kgf/mm^2)^{-1}$)	Notes
A. Copper					
Witteborn & Fairbank	Electron TOF	10^{-2}	4.2	$+(6 \pm 0.6)\times10^{-4}$	b
Beams	Rotor	10^{3}	300	No quantitative result	c
Craig	Compression	1	300	-(300 - 700)	d
French & Beams	Extension	1-15	300	-(120 ± 40)	e
				+1200	f
Guptill	Acceleration	10^{-1}	300	-(60 ± 6)	g
Brown et al.	Acceleration	6×10^{-2} (peak)	300	3 ± 15	h
Enga	Compression	1-8	300	No direct determination	i
DMRT	Theory	—	—	-60	j
Rieger	Theory	—	—	-400	k
				-17	l
B. Aluminum					
Goldstein	Tunnel Junction	$(2.5 - 5)\times10^{-2}$	2	-(375 - 750)	m
Craig	Compression	1	300	-(140 - 570)	d
Brown et al.	Acceleration	6×10^{-2} (peak)	300	4 ± 15	h

(cont'd)

Table 2.1 (cont'd)

Investigator	Method	Stress Level (kgf/mm^2)	Temperature (°K)	Result ($\mu V(kgf/mm^2)^{-1}$)	Notes
DMRT	Theory	—	—	-0.9×10^3	j
Rieger	Theory	—	—	-1.66×10^3	k
				-0.11×10^3	l

[a]Results converted to consistent units when necessary.
[b]Ref. 3.
[c]Ref. 30. Although no quantitative results were quoted, the author indicates basic agreement with the DMRT result.
[d]Ref. 31.
[e]Ref. 32. Work-hardened copper.
[f]Annealed copper, value obtained from Fig. 2 of Ref. 32.
[g]Ref. 33.
[h]Ref. 34.
[i]Ref. 35. The author points out that it is impossible in his case to separate the intrinsic strain-induced field from other strain-induced fields which arise from surface effects. He describes mechanisms which can account for variations in the strain-induced field outside a metal of ± 250 $\mu V (kgf/mm^2)^{-1}$.
[j]Ref. 2.
[k]Ref. 29, using a value for the electron-phonon coupling constant obtained from resistivity data.
[l]After Ref. 34, using an electron-phonon coupling constant obtained from ultrasonic attentuation data.
[m]Ref. 36.

2.4 Reconciliation of Witteborn-Fairbank Results with Theoretical Predictions and Results of Other Experiments

It appears now that all theorists who have considered the question of the gravitationally-induced electric field in a metal are in general agreement on the basic validity of the DMRT theory. The one experiment which has measured the internal field in a metal subject to a strain gradient produced results which are in reasonably good agreement with the DMRT predictions. The nature of the electric field outside the metal arising from the internal field is a more complex issue. Normal electrostatic continuity conditions imply that the tangential electric field should remain constant as the surface of the metal is crossed. However, there are problems in making a straightforward application of this principle to the situation at hand since it implies a very idealistic view of a metal. Enga[35] has shown how the details of the patch distribution at the surface of a polycrystalline metal can produce strain-induced potential variations as large as $\pm$ 250 $\mu V\ (kgf/mm^2)^{-1}$, particularly through the anisotropic elastic strain effect. Also, we discussed in Sec. 2.2 the ability of small levels of surface contamination to produce rather large shifts in the electric field outside a surface. Enga's work shows that the presence of a surface film can result in an additional mechanism for the production of strain-induced potential variations.

One feature which stands out rather strongly when the various experimental studies of the problem are reviewed is the tremendous variation in the magnitude (and even the sign) of the strain-induced contact potential shift with the surface and bulk properties of the sample. For example, in the careful series of experiments performed

by French and Beams[32], the strain-induced shift in contact potential in copper ranged from a value of - 120 μV $(kgf/mm^2)^{-1}$ for fully work-hardened copper to + 600 μV $(kgf/mm^2)^{-1}$ (calculated on the basis of their Fig. 2) for annealed copper with the contact potential shift per unit stress depending on the stress level. The uncertainties in the contact potential shift were especially large at stress levels below 1 kgf/mm^2. To quote from their paper concerning measurements on copper from 0-1 kgf/mm^2: "Actually, in some cases the initial observed change [in contact potential] was zero or slightly positive for small stresses, but changed sign before reaching stresses of 1 kg[f]/mm^2."

We should also note that the sign of the contact potential shift for work hardened copper varies from one experiment to another. In Craig's experiment[31], compression produced a positive shift, in Brown et al.[34] a negative shift, while in the experiment of French and Beams[32], tension produced a negative shift. Of course, a direct comparison of the experiments on work hardened copper is difficult because the degree of work hardening is likely to vary considerably from one experiment to another. All theories to date predict a decrease in work function with compression.

Thus we see that even after the considerable amount of experimental work on the strain-induced contact potential problem the situation is far from clear. Enga's work points out some of the considerations that must be taken into account in such experiments; however, in most cases the information needed to make numerical corrections based on these considerations is not available. It appears though that the bulk of the experimental evidence points to the

existence of strain-induced electric fields outside copper which are three to six orders of magnitude larger than the largest strain-induced field which would be consistent with the WF experiment. Thus it seems that some aspect of the conditions of the WF experiment prevented the appearance of the strain-induced field.

Several differences between the WF experiment and the other experiments have been pointed out as possible explanations of the discrepancy. These include the particular nature of the electroformed amorphous copper drift tube used by WF,[37] the high vacuum (10^{-12} Torr) and low temperature (4.2°K) operating environment of the WF experiment[21,38], and the small (10^{-2} kgf/mm^2), non-uniform stress which was present.[38] The experiments of Guptill[33] and of Brown et al.[34] suggest that the stress level is not the determining factor. Whatever the mechanism may be, the apparent complete absence of the DMRT strain-induced field in the WF experiment seems to imply the existence of a shielding layer of negative charge (apparently electrons) on the inside surface of the drift tube which does not share the gravitationally-induced deformation of the underlying metal (remember, of course, that for the copper tube we no doubt have a 10-20 Å layer of CuO on the surface). Rorschach and Trammel[37] have suggested a "whisker" model of the surface which could provide the requisite shielding. Schiff[21] mentions the possibility of a fluid layer (e.g. adsorbed gas) whose electrons would be decoupled from the underlying metal; he also suggests that such a layer might be stable at the 4.2°K temperature of the WF experiment but not at the higher temperatures present in the other experiments which studied the external strain-induced electric field.

As we mentioned in Sec. 2.2, the walls of the drift tube do have a surface layer of adsorbed gas which may have a role in the surface shielding effect. However, the possibility that increased adsorption of gas at low temperatures is directly responsible for a temperature-dependent shielding effect in the WF experiment seems unlikely, since the residual gas pressure in the WF apparatus prior to cooldown is far from high enough to allow an additional monolayer of gas to be adsorbed on the drift tube surface at 4.2°K.

In any event it seems clear from our discussion of the WF experiment, the theoretical predictions, and the work of other experiments that some form of unusual surface shielding is occurring in the WF experiment. After we have established in Chapter 4 the nature of the temperature dependence of this anomalous shielding we will return to a consideration of some possible surface state models which incorporate an appropriate temperature dependence.

CHAPTER 3

TECHNIQUE OF MEASUREMENT

3.1 Introduction

As stated in Chapter 1, the objective of this work is to determine the conditions under which the anomalous surface shielding effect found in the Witteborn-Fairbank (WF) experiment occurs. We have focused our attention thus far on the determination of whether the shielding effect becomes inoperative at some drift tube temperature above 4.2°K and if so, at what temperature.

We use the basic electron time-of-flight (TOF) technique employed by WF and a somewhat updated and modified version of their apparatus. Both their procedure and their apparatus have been described elsewhere[3,4,7]; however, for completeness we will review very briefly the main points of the technique. We will then describe the ways in which our technique differs from that of WF. The changes in the apparatus will be discussed in connection with the apparatus description presented in Sec. 3.3.

In the basic electron TOF technique a short burst of electrons is emitted from a pulsed cathode and guided by a persistent superconducting magnet through the shielding tube, or drift tube, to a windowless photomultiplier detector. The drift tube is electrically biased so that the electrons of interest move slowly only while they are in the drift tube. In addition, magnetic state selection is employed so that only electrons in the cyclotron ground state are studied. This reduces to a negligible level the effects of inhomogeneities in the guide field since the net magnetic moment of electrons

in the ground state is just the anomalous magnetic moment. The electrons which arrive at the detector are counted as a function of flight time by a multi-channel scaler. When the multi-channel scaler finishes counting in its final time-of-flight channel it resets to its first channel and another cathode pulse is initiated. It is possible to set up an accurately known constant electric field in the tube by passing an axial current through the tube walls.

The principal way in which our procedure differs from that of WF is in the analysis of the TOF spectra. We have chosen to sacrifice some directness of measurement in order to gain speed of data collection and analysis. WF used a multi-parameter nonlinear least squares fitting program in order to extract from the TOF distributions the average force acting on an electron while it was in the drift tube. The measured force can then be compared to the force which is applied by means of the axial current; such comparisons made over a range of applied force values allow a sensitive determination of the ambient force in the tube. However, this method requires both large amounts of data for each value of applied force and large amounts of computer time for each fit. Since we were interested in determining the nature of the TOF distribution under a wide variety of conditions, we decided to adopt a differential technique which would allow us to deduce from a relatively small amount of data taken under a given set of conditions a rough upper limit on the magnitude of any ambient electric fields present in the drift tube under those conditions. Our method consists of establishing a set of experimental conditions and then taking in the same run data with no applied electric field in the tube and data with three different values of applied field. Each

run thus consists of four sub-runs. In general, an experimental run lasts for several hours; during this time the applied field is cycled through its four values 15-20 times in order to minimize the effects of long-term drifts in the experimental conditions. Then, rather than trying to determine the observed force in the tube for each of these sun-runs, we determine for each of the three applied force spectra the ratio of the count rate in each TOF interval to the count rate in the corresponding TOF interval of the zero-applied-force spectrum.

In some cases (the room temperature, LN_2 temperature, and first LHe runs), examination of these ratio spectra allows us to determine only whether or not a given applied force causes a depression of the slow electron flux (slow electrons are defined here as those which arrive after the theoretical cutoff time discussed in the following section). In the case of the heated drift tube data we were able to obtain from each of the three spectra of force/no force ratios an actual estimate of the observed field. If we plot these estimates as a function of applied field and extrapolate to zero applied field we can obtain a determination of the ambient equivalent electric field in the drift tube.

Aside from its advantages in terms of the amount of data needed to obtain usable results, this method also seems to allow the TOF technique to be used in cases where the ambient field is quite large (10^{-6} V/m or so). It is quite difficult to use the multi-parameter computer fit method in such cases. Large ambient field values generally correspond to situations in which very little information

is available with which to construct the model of the potential distribution in the tube needed by the computer program.

When definite observed field estimates are obtained, the differential analysis technique does not require any knowledge of the detailed nature of the tube's potential distribution. In the cases where we can determine only whether or not an applied force causes a depression of the slow electron flux we must make a basic assumption about the level of applied force which will affect the TOF distribution when an arbitrary potential distribution is present in the tube. We assume that the potential difference produced along the length of the tube by the smallest value of applied electric field which has a significant effect on the slow electron flux must be comparable to the magnitude of the ambient axial potential variations. We present some justification for this assumption in Sec. 3.2; we are able to make a rather strong case for saying that the ambient potential variations cannot be more than an order of magnitude or so larger than the smallest applied potential gradient which significantly depresses the slow electron flux. Of course, this assumption is no longer valid when we consider applied forces so small that their effects are comparable to those produced by noise sources such as residual gas scattering, electrical noise in the biasing circuits, etc.

We discussed in Chapter 2 the nature of the expected ambient potential variations in the tube. We will now proceed to a discussion of the effect of these potential variations on the TOF distribution. We should note that a gravitationally-induced electric field will yield a linear potential gradient in the tube; thus it will produce the same effect as an applied linear potential gradient. After our

discussion of the TOF distributions, we will describe the apparatus in Secs. 3.3-3.5 and our procedure in Sec. 3.6.

3.2 Effect of Drift Tube Potential Variations on the TOF Distribution

In the ideal case the drift tube would act only as a perfect electrostatic shield so that the only force acting on an electron in the tube would be gravity. Since the drift tube is normally made 0.1 V or so more negative than the cathode, it also serves as an energy selector; only electrons which leave the cathode with 0.1 eV or more KE are able to enter the drift tube.

If we for the moment neglect the force of gravity on the electrons, then in the ideal case the TOF distribution will be determined only by the velocity spread of the electrons emitted by the cathode when we take into account the - 0.1 V drift tube bias. If we let E_0 represent the energy which is required if an electron is to enter the tube, the number of electrons which enter the tube with energies between E_0 and $E_0 + dE$ will be given by

$$dN = C(E_0)dE \ ; \tag{3.1}$$

$C(E_0)$ is determined by the cathode emission and bias parameters (we obtain this result in connection with our discussion of the cathode in Sec. 3.3.2). After integrating both sides of this equation, we get the number of electrons which have a kinetic energy in the tube less than E_k for small values of E_k:

$$N(E < E_k) = C(E_0)\ E_k \ . \tag{3.2}$$

These electrons will all arrive after a time t determined from

$$E_k = \frac{1}{2} m \left(\frac{s}{t}\right)^2 \tag{3.3}$$

where s is the drift tube length. Thus the number of electrons arriving at time t or later is given by

$$N(t) = \frac{1}{2} C(E_0) m s^2 t^{-2} = C_1 (E_0)\ t^{-2} . \tag{3.4}$$

We will frequently be interested in the number of electrons which arrive between t and t + Δt (this is how the data is taken), given by

$$\Delta N(t) = C_1(E_0)\ [t^{-2} - (t + \Delta t)^{-2}] \tag{3.5}$$

which for $\Delta t \ll t$ (true in all cases of interest) becomes

$$\Delta N(t) = 2C_1(E_0)\ \Delta t\ t^{-3} . \tag{3.6}$$

In practice there is an enhancement of the proportion of electrons having very long flight times; we will discuss some of the possible reasons for this enhancement in the data analysis chapter.

3.2.1 Effect of a Linear Potential Gradient

Any linear potential gradient in the tube, whether caused by gravity, an applied axial current, or a gravitationally-induced electric field, will exert a constant force on an electron in the tube. If we let F be the net force on the electron, we can find the TOF of an electron which has velocity v_i at the bottom of the tube from the equation

$$s = v_i t + \frac{1}{2} Ft^2/m \tag{3.7}$$

where s is the effective length of the drift tube. We thus obtain

$$t = \frac{-v_i + \sqrt{v_i^2 + 2Fs/m}}{F/m} \quad . \tag{3.8}$$

If F is negative (retarding) then the maximum TOF is obtained when $v_i^2 = -2Fs/m = 2|F|s/m$:

$$t_{max} = \sqrt{\frac{2ms}{|F|}} \quad . \tag{3.9}$$

Any electron having a smaller initial velocity is unable to reach the top of the tube. If F is positive (accelerating) then the maximum TOF occurs when $v_i = 0$:

$$t_{max} = \sqrt{\frac{2ms}{F}} \quad . \tag{3.10}$$

This is the theoretical "cutoff time" in the TOF distribution.

3.2.2 Effect of Random Potential Variations

We discussed in Chapter 2 how the patch effect produces random potential fluctuations in the tube which, depending on the model chosen, may be as large as 10^{-6} V or so. It is essentially impossible to make accurate predictions of the effects of these potential fluctuations on the TOF distribution since we have so little information concerning the nature of the patch distribution in the drift tube. We can only make a few general observations.

If the patch distribution is totally random we can reasonably expect that there will be a region of maximum potential in the tube;

the nature of this potential bump will then effectively determine the TOF distribution. Kincaid[39] has investigated the case of a parabolic potential hill; he finds that the resulting TOF distribution goes as t_ϕ^2/t^2 for short flight times and as e^{-t/t_ϕ} for long flight times, where t_ϕ is expressed in terms of ϕ_m, the amount by which the high point of the hill exceeds the average potential, and h, the axial extent of the hill:

$$t_\phi = h\sqrt{\frac{m}{2\phi_m}} \quad . \tag{3.11}$$

Thus if ϕ_m is sufficiently large and the potential bump is small in axial extent compared to the drift tube length, its presence will significantly reduce the slow electron flux (basically because the lowest energy electrons which can pass through the tube now have a small KE for only a small portion of the drift tube length).

The presence of a potential bump also determines a minimum linear potential gradient which will be able to produce a cutoff in the TOF distribution. If we view the potential bump as a minimum velocity selector, it is easy to see that a linear gradient will not cause a cutoff unless it raises the potential of the top (or bottom) of the drift tube above the level of the bump.

A linear gradient which is not large enough to produce a cutoff will have an appreciable effect in modifying the flight times of low energy electrons which pass through the tube if it produces a potential at the end (the top end for our common case of retarding applied fields) of the tube which is a sizeable fraction of the potential of the bump. We can estimate the magnitude of this effect by first

calculating the effect of a linear gradient on the flight time of an electron having an arbitrary initial energy (in a tube having no random potential variations) and then seeing how this effect is modified by the presence of a potential bump in the tube. The flight time of an electron which enters the drift tube with energy E_i is given by

$$t = \sqrt{\frac{m}{2}} \int_0^s \frac{dz}{\sqrt{E_i - \phi(z)}} \tag{3.12}$$

where $\phi(z)$ is the potential seen by the electron at axial position z ($-|e|$ times the electrostatic potential). If there are no ambient potential variations in the tube then $\phi(z) = \bar{\phi}$ and

$$t = \sqrt{\frac{m}{2}} \frac{s}{\sqrt{E_i - \bar{\phi}}} \tag{3.13}$$

(we are neglecting gravity for the moment). Let us now take $\bar{\phi} = 0$ and assume a linear gradient

$$\phi(z) = \phi_a z/s \ ; \tag{3.14}$$

then an electron which starts out with total energy E_i will arrive at

$$(t + \Delta t) = \sqrt{\frac{m}{2}} \int_0^s \frac{dz}{\sqrt{E_i - \phi_a z/s}}$$

$$= \left(\frac{s}{\phi_a}\right)\sqrt{2mE_i}\ \left[1 - \left(1 - \frac{\phi_a}{E_i}\right)^{1/2}\right]. \tag{3.15}$$

If we assume $\phi_a/E_i \ll 1$ and expand the root in brackets, keeping the first three terms, we obtain

$$(t + \Delta t) = \left(\frac{s}{\phi_a}\right)\sqrt{2mE_i}\left[\frac{\phi_a}{2E_i} + \frac{\phi_a^2}{8E_i^2}\right] \quad ; \tag{3.16}$$

thus the added transit time due to the presence of the gradient is

$$\Delta t = \left(\sqrt{\frac{m}{2}}\right)\frac{s\phi_a}{4E_i^{3/2}} \tag{3.17}$$

and

$$\Delta t/t = \frac{\phi_a}{4E_i} \quad . \tag{3.18}$$

This gives us a quick way to estimate the effect of a linear gradient on the flight time of an electron which enters the tube with a KE of E_i.

Now let us look at the case of a potential bump along the tube axis. We will assume that, although the presence of the bump gives a few very slow electrons (according to the results at the beginning of this section), the principal influence which the bump has on the TOF distribution is its action as a minimum velocity selector which allows only electrons which enter the tube with a KE of E_0 or greater to pass through. In the presence of such a potential bump, a linear gradient which is to have a 10% effect on the TOF of an electron of KE E_0 must produce a maximum potential of

$$\phi_a \cong 0.4\ E_0$$

according to Eq. (3.18).

Such a linear gradient will have only about a 5% effect on the TOF of electrons having a KE twice as great. The effect on the TOF values of even higher energy electrons will be essentially negligible.

Thus we see that, since there will generally be very few electrons in the energy range E_0 - $2E_0$ [because of the small values of E_0 which we employ and the distribution function of Eq. (3.1)], applied gradients (or ambient linear gradients) which produce a maximum potential less than about 0.4 E_0 will not make observable changes in the TOF spectra.

The effect of a linear gradient which has $\phi_a > 0.4\ E_0$ will depend on the location of the potential bump in the drift tube. For example, if the bump is located at the top of the drift tube, a retarding applied field will not be able (even theoretically!) to produce a sharp cutoff. For other locations of the primary potential bump, an applied gradient which raises the top of the tube above the potential of the bump should be able to produce a reasonably good cutoff (at least in theory). If the applied gradient produces a maximum potential slightly smaller than the bump potential, its main effect will be the production of a depression in the flux of electrons having long flight times. The electrons which formerly arrived between t_1 and t_2 will now arrive between [by Eq. (3.17)]

$$t_1 + \sqrt{\frac{m}{2}} \left(\frac{s\phi_a}{4\left(\frac{m}{2}\ \frac{s^2}{t_1^2}\right)^{3/2}} \right)$$

and

$$t_2 + \sqrt{\frac{m}{2}} \left(\frac{s\phi_a}{4 \left(\frac{m}{2} \frac{s^2}{t_2^2} \right)^{3/2}} \right) \quad ;$$

this time interval is larger than the $t_1 - t_2$ interval by an amount

$$\Delta\tau = \frac{\phi_a}{2ms^2} (t_2^3 - t_1^3) \ . \tag{3.19}$$

This time spreading effect tends to show up as a reduction in the flux of electrons having long flight times in the applied gradient distribution as compared to the distribution obtained with no applied force. However, there is a counterbalancing effect: the group of electrons we are considering has been shifted to its new region of arrival times from a region of the TOF spectrum in which the distribution function has larger values than in the new region, thus tending to make the flux in the new region larger than it would otherwise be. Because of the type of decay in the TOF distribution seen in most of our work (decaying exponential with a rather large time constant), the time dilation effect is much more important than the effect of the difference in the distribution function. We can determine the approximate extent of the reduction in the slow electron flux as follows.

Let D (t) be the delay function which gives the new arrival time in the presence of an applied linear gradient of an electron which formerly arrived at t, as obtained from Eq. (3.17):

$$D(t) = t + \sqrt{\frac{m}{2}} \left(\frac{s\phi_a}{4 \left(\frac{m}{2} \frac{s^2}{t^2} \right)^{3/2}} \right) = t + \gamma t^3 \tag{3.20}$$

where $\gamma = \phi_a/2ms^2$. The number of electrons which arrive between t and $t + \Delta t$ with no applied force, given by

$$A\int_{t}^{t+\Delta t} e^{\alpha t}\, dt$$

(assuming an exponential distribution function for the slow electrons) will, with the applied gradient, arrive between $D(t)$ and $D(t + \Delta t)$, resulting in an average flux in that time interval of

$$A\int_{t}^{t+\Delta t} e^{\alpha t}\, dt/[\,D(t + \Delta t) - D(t)]\ .$$

The average flux in the same time interval in the zero-applied-force distribution is

$$A\int_{(t)}^{(t+\Delta t)} e^{\alpha t}\, dt/[\,D(t + \Delta t) - D(t)]\ .$$

Thus the ratio of the average flux in the time interval $D(t)$ to $D(t + \Delta t)$ in a spectrum taken with an applied gradient to the average flux in the same interval in a similar spectrum taken with no applied gradient is

$$R = \frac{\int_{t}^{t+\Delta t} e^{\alpha t}\, dt}{\int_{D(t)}^{D(t+\Delta t)} e^{\alpha t}\, dt}\ . \qquad (3.21)$$

If we consider only flight times less than about 100 ms then for typical values of α we will have $\alpha t \ll 1$, allowing us to approximate the exponential with the first two terms of its expansion. Then we have

$$R = \frac{\Delta t}{t + \Delta t + \gamma(t+\Delta t)^3 - (t+\Delta t^3)}$$

$$\approx \frac{\Delta t}{\Delta t + \gamma[(t+\Delta t)^3 - t^3]} \quad .$$

We are interested in Δt for which $\Delta t/t \ll 1$, so this becomes

$$R = \frac{\Delta t}{\Delta t + \gamma[t^3(1+3\frac{\Delta t}{t}) - t^3]} = \frac{1}{1+3\gamma t^2} \quad . \tag{3.22}$$

It is interesting to consider a representative example. Say the largest potential hill in the tube has a maximum potential of 2.5×10^{-8} eV and assume that the only effect of this potential hill is to determine the minimum energy needed by an electron which is to reach the detector. Now let us apply a linear gradient having a maximum potential of $0.4\ \phi_a = 10^{-8}$ eV. Electrons which have energies of $(2.5\text{-}3.0) \times 10^{-8}$ eV take about 10 ms to reach the detector. For $\phi_a = 10^{-8}$ eV and $s \cong 1$ m we have $\gamma = 870\ \text{sec}^{-2}$, so these electrons will, with the applied gradient, arrive at

$$D(10\ \text{ms}) = 10\ \text{ms} + 870\ \text{sec}^{-2}(10^{-6}\ \text{sec}) \cong 11\ \text{ms}.$$

Thus the ratio of the applied force spectrum to the spectrum with no applied force for a small time interval near 11 ms will be

$$R = \frac{1}{1+3(870)(.01)^2} = \frac{1}{1+0.26} = 0.79.$$

For this case we get a significant depression of the slow electron flux several ms before the theoretical cutoff at 34 ms.

The general ideas we have discussed concerning the effect of linear applied potential gradients on the TOF distribution in the

presence of ambient potential fluctuations in the drift tube are used extensively in Chapter 4. Much of the room temperature and LN_2 temperature analysis is based on the assumption that an applied gradient will not produce an observable effect on the slow electrons unless it produces a maximum potential which amounts to at least a few tenths of any potential fluctuation in the tube. We feel that the validity of that approach is established by the foregoing analysis.

The spatially fluctuating radial electric fields produced by the patch effect may also affect the TOF distribution although the likelihood of this is small. Since the electrons passing through the tube are in quantized cyclotron states, changes in the xy motion can occur only if there is a cyclotron transition. If the fluctuations in the radial electric field occur quasi-adiabatically, cyclotron transitions will in general not be stimulated. Such transitions will occur only if there is a sudden change in the radial field such that the Fourier spectrum of the field change contains a component which has $h\nu$ close to the cyclotron level spacing. It seems quite unlikely that such large transitions will exist 2.5 cm above a surface whose patches are smaller than 1 μ since the cyclotron level spacing in our experiments ranged from $\sim 10^{-7}$ eV at room temperature to $\sim 4 \times 10^{-7}$ eV at 4.2°K (because of the different values of guide field utilized at the different temperatures), while the patch effect potential fluctuations should be smaller than $\sim 3 \times 10^{-6}$ eV. If cyclotron transitions are in fact excited, the TOF spectrum can be affected since some of the z energy can be coupled

into the cyclotron motion; however, such effects should be the same whether or not an applied linear potential gradient is present. The radius of the cyclotron orbit also changes; however, it remains quite small in all cases (it is given by $r = (5 \times 10^{-5}\ \text{cm})\sqrt{n}$ where n is the cyclotron quantum number) so that an orbit change should not be important per se.

The situation in which there is some periodicity in the patch distribution is of course more favorable for TOF experiments. We can view the periodic patch distribution as a superposition of single potential hills of the type previously discussed. The presence of additional potential hills equal in extent and maximum potential to the original will result in a greater flux of slow electrons since the amount of time the low energy electrons spend in regions where they have very little KE increases linearly with the number of such hills. As the period of the patch distribution gets smaller and smaller in relation to the tube length, we approach more and more closely the ideal case of a constant potential along the length of the tube. The periodic situation makes it much easier to obtain cutoff effects (or more precisely, slow electron flux changes) with small applied linear potential gradients. Consider the case of two equal potential hills. If a small applied gradient rasies even slightly the potential of the hill which is nearer to the top of the tube, there will be a consequent reduction in the slow electron flux since low energy electrons will then move slowly in only one region of the tube rather than two.

In any case, the fundamental point is that even if gravitationally-induced electric fields and large patch effect potential

fluctuations are present in the drift tube, we should still be able to estimate the magnitude of the net potential variations by comparing TOF runs taken with an applied linear gradient to runs taken under the same conditions with no applied force and looking for changes in the slow electron flux. The success achieved with this approach would seem to establish its validity.

3.3 Electron Time-of-Flight Apparatus, 4.2°K Version

The objective of this section is to present a reasonably complete description of the major subsystems of the electron TOF apparatus with particular emphasis on areas in which substantial changes have been made since the original electron free fall work. Those details of the TOF apparatus which have been described by Witteborn[3,7] and which remain the same for the present work will be mentioned very briefly if at all.

In Sec. 3.1 we gave an overview of the electron TOF technique. The following discussion will present the basic apparatus as used in experiments at 4.2°K. Later, in Secs. 3.4 and 3.5, we will discuss the modifications which we made to enable us to work at room temperature and LN_2 temperature and to conduct the heated drift tube experiments.

Figure 3.1 is a view of the upper portion of the apparatus and the associated electronics. The LHe dewar extends to the floor of the room below. The ion pump which maintains the very high vacuum needed for the experiment is visible at the top of the apparatus. The photograph also shows an assembly of magnetic shields surrounding the dewar and extending a few feet above floor level.

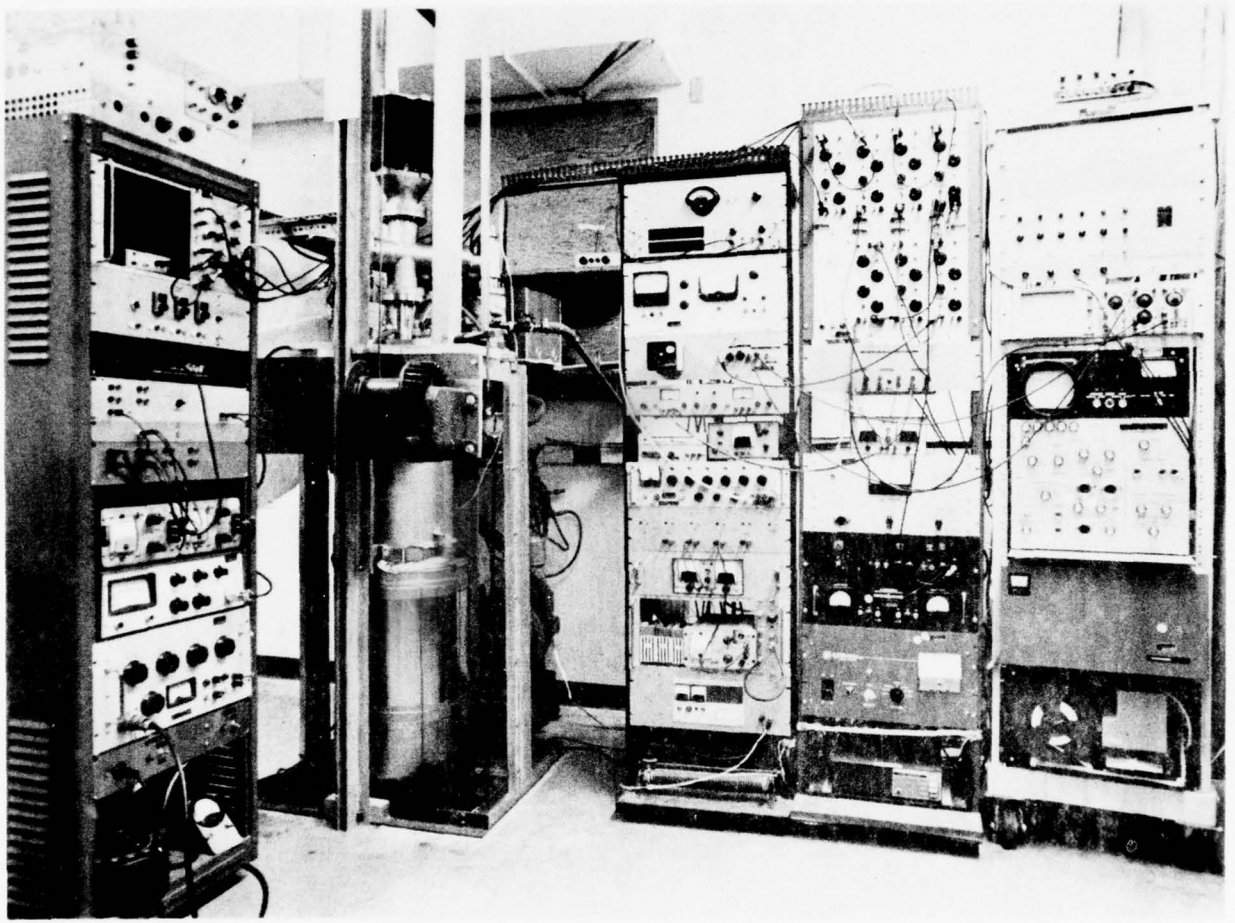


Fig. 3.1. A view of the upper portion of the apparatus and the associated electronics.

3.3.1 Cryogenic and Vacuum Systems

The basic structure of the cryogenic and vacuum systems is illustrated in Fig. 3.2, which shows a cross-section of the essential mechanical structure of the apparatus.

The helium dewar is a custom-manufactured nitrogen-shielded aluminum and fiberglass unit made by Linde; it has a demountable lower section which was added to accommodate the proposed slow position source. The helium vessel has an inside diameter of 8" and a total inside length of 17'. With the apparatus inserted approximately 60ℓ of LHe is required to fill to the necktube of the dewar once the apparatus has cooled to 4.2°K. The boiloff rate under running conditions is just under 1 liquid liter/hour.

The vacuum housing for the apparatus is made of OFHC copper below the top of the main guide solenoid and thin wall stainless steel above (300 series to minimize magnetic field distortion near the detector). The top of the stainless steel tube connects to a stainless steel flanged cross. At the top of this cross is located a Varian 80 l/sec ion pump which is on continuously (except during data taking). One side arm of the cross leads to the rotary motion feedthrough with which the position of the upper drift tube is adjusted. The other side arm goes to an all metal bakeable valve which seals off the high vacuum system. At the bottom of the apparatus a demountable flange is included to permit replacement of the thin-film cathode.

The only construction materials used on the high vacuum side of the bakeable valve are OFHC copper, 300 series stainless steel, indium,

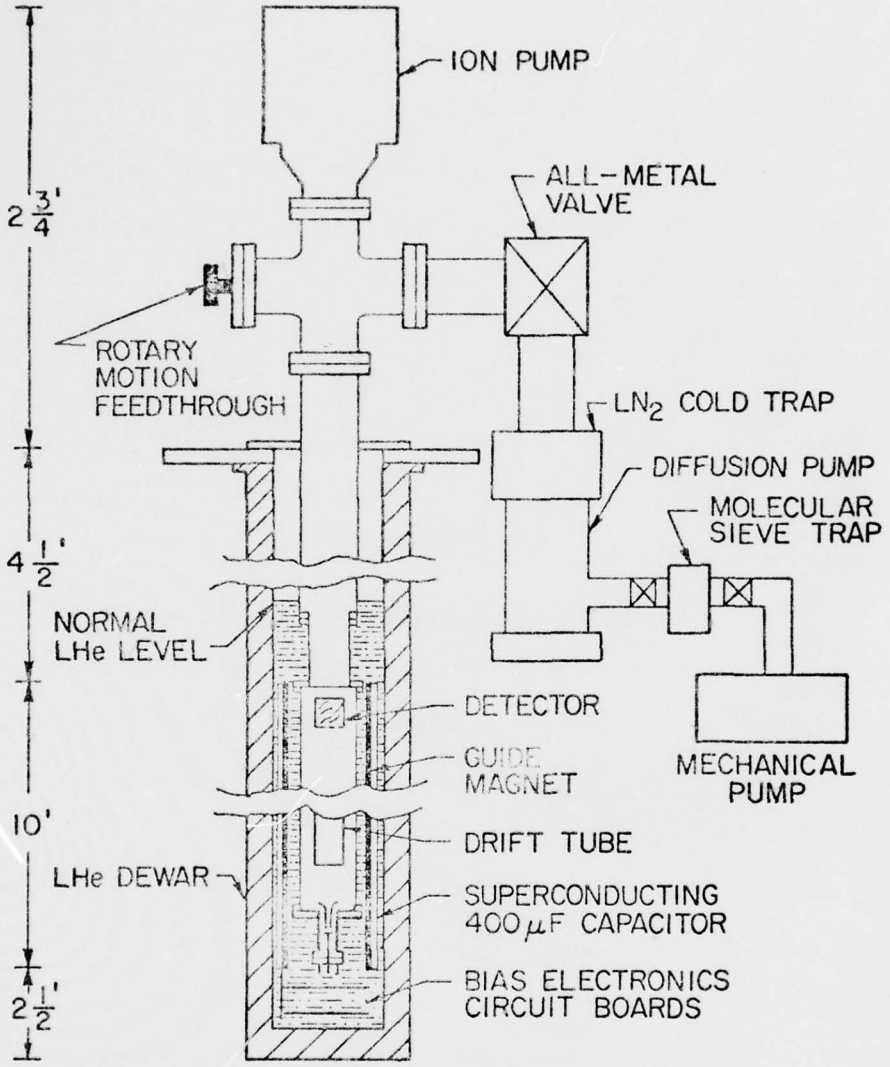


Fig. 3.2. A cross-section of the mechanical structure of the apparatus and the vacuum system.

glass, and ceramic. Careful attention to cleanliness allows the attainment of a 10^{-9} Torr room temperature pressure.

The pumping system on the far side of the bakeable valve consists of a liquid nitrogen cold trap, a 750 l/sec oil diffusion pump, and a molecular-sieve-trapped 375 l/min mechanical forepump. The diffusion pump is charged with low vapor pressure Dow Corning DC704 fluid. It is necessary to use this pumping system only during the initial 1-2 hours of a pumpdown from atmospheric pressure. The ion pump is started as soon as the pressure reaches approximately 5×10^{-8} Torr and the bakeable valve is sealed. Care is taken to ensure that the diffusion pump is never turned on until the cold trap has cooled to liquid nitrogen temperature. The cold trap is also thoroughly cleaned after each use to further guard against migration of the diffusion pump oil. The molecular sieve trap is baked out prior to each use.

The actual operating vacuum at 4.2°K is about 10^{-11} Torr. The ion pump is turned off during runs; however, we see only a very slight increase in residual gas pressure when the pump has been off for 24 hours or so.

3.3.2 Cathode

Our electron source is a thin-film tunnel cathode, consisting of a glass substrate on which is deposited a 600-2000 Å film of Al followed by a 75 Å layer of Al_2O_3 and a 70-100 Å layer of Au. A schematic diagram of the structure is shown in Fig. 3.3. The operation and properties of this type of device have been discussed elsewhere.[40-42] (In particular, Onn et al.[43] have carefully studied

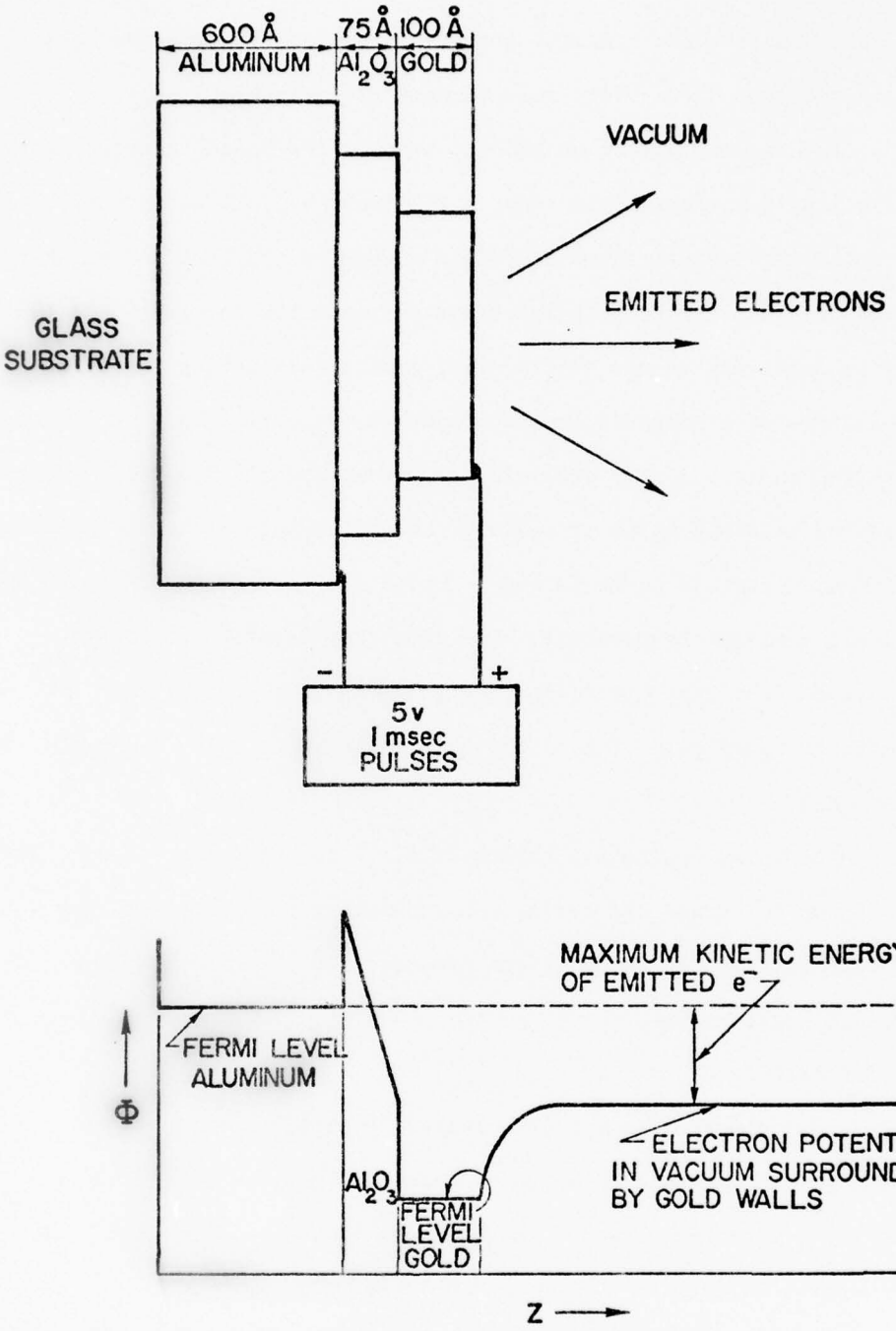


Fig. 3.3. A schematic diagram of a tunnel cathode. The upper diagram is a greatly magnified cross section of the tunnel cathode structure. The lower portion of the figure shows the potential energy at positions corresponding to the upper diagram when the emission pulse is on.

the properties of tunnel cathodes at 4.2°K.) Emission is obtained when the potential of the Au film relative to the Al is raised to a level larger than the work function of Au. Electrons from the Al enter the conduction band of the Al_2O_3, either by direct tunneling or by thermal excitation (or by other possible mechanisms as described by Onn et al.). Since the mean free path for these electrons in the Au film is of about the same magnitude as the film thickness, a usable number of electrons are able to escape from the Au surface into the vacuum above. In our apparatus, a positively-biased electrode is located just above the cathode to reduce the space charge in that area.

The actual devices which we use were fabricated to our specifications by Forrest Futtere of the Stanford solid state shop. We typically obtain an emission current of 50-100 nA with a drive current of about 4 mA. The cathode is of course operated in the pulsed mode with drive pulses 0.1-1.0 ms wide delivered by a constant voltage driving circuit (a constant voltage circuit must be used to avoid the damaging effects of large voltage transients).

Figure 3.4 shows the differential energy distribution for electrons emitted from a typical cathode. This distribution was obtained by biasing the drift tube with respect to the cathode and using time of flight to perform the energy analysis. This energy distribution shows a quite small width (0.35 eV). We expect a reasonably small width since we use a thin layer of oxide ($\sim$70 Å). The width of our distribution is consistent with Fig. 9 of Kanter and Feibelman[41] since our diode voltage is only $\sim$3.0 V. The shape of our energy distribution is also basically consistent with the

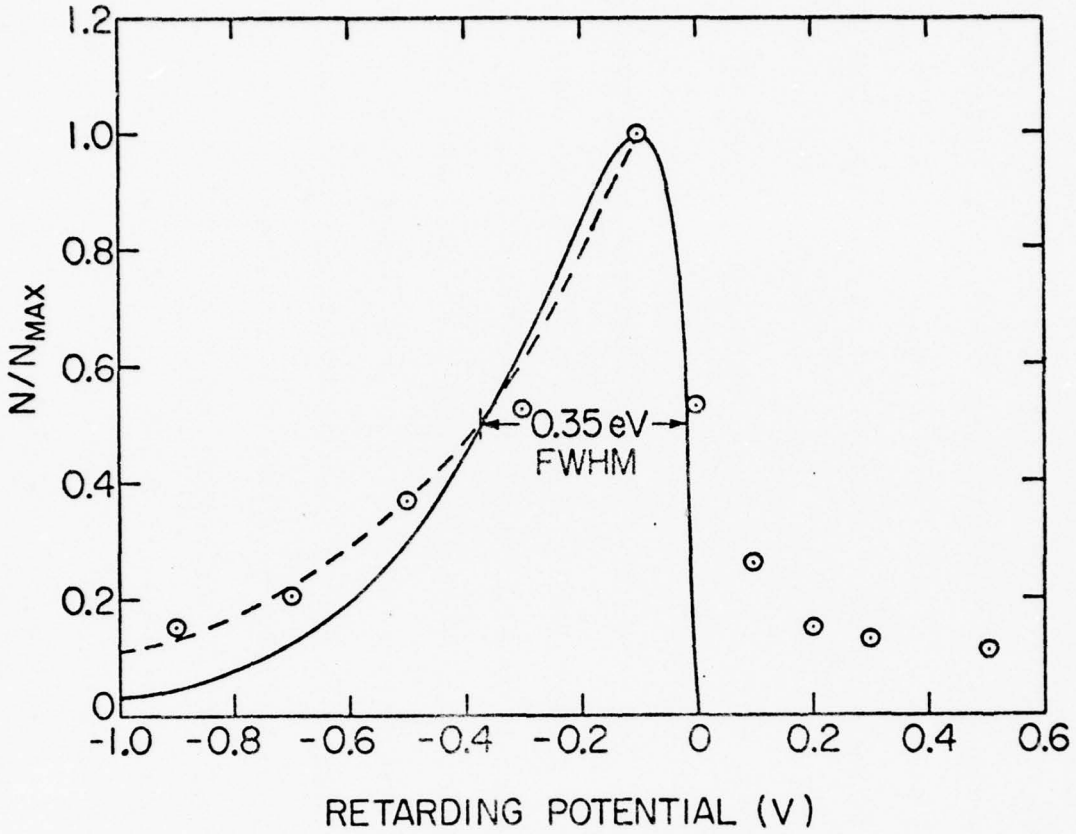


Fig. 3.4. The energy distribution of electrons emitted from the tunnel cathode. This distribution was obtained by using the drift tube as a retarding electrode; the retarding potential is the potential of the drift tube relative to the cathode. The solid curve is a normalized modified Maxwellian distribution while the dashed curve is a normalized Maxwellian distribution.

differential energy distribution which Kanter and Feibelman present in their Fig. 11 (although the device used to obtain that figure was operated at 7 V).

The solid line in Fig. 3.4 is a normalized modified Maxwellian distribution

$$N/N_{max} = \sqrt{E}\ e^{-E/kT} \tag{3.23}$$

with kT = 0.2 eV. This would represent the distribution expected from a thermal source at 2300°K having a work function barrier if all electrons having the same energy were affected in the same way by a retarding voltage on the drift tube, independent of the direction in which the electrons were emitted from the cathode. The dashed line is a normalized Maxwellian distribution

$$N/N_{max} = e^{-E/kT} \tag{3.24}$$

with kT = 0.4 eV. This would be the distribution of only the z-component of kinetic energy of electrons emitted from a thermal source at 4600°K. It appears that this distribution describes the data quite well, at least on the left-hand side of the peak. To explain the right-hand side we must consider the Schottky effect; we will not pursue the discussion since it is not important to our work. We might expect some tendency for the left-hand portion of the distribution to follow the solid curve in preference to the dashed one because of the magnetic focusing properties of the guide field in the apparatus (our energy distribution was taken with small

guide fields in both the main solenoid and the cathode magnet); however, there seems to be only a very slight, if any, tendency toward this.

We will need two results in our later analysis: the form of the total energy distribution for small energy ranges and the fraction of the total emission current made up of magnetic ground state electrons which have 10^{-7} eV or less z-axis kinetic energy. We will assume that the cathode differential energy distribution is well represented by a Maxwellian with kT = 0.4 eV. Then assuming the z-axis is normal to the surface of the thermal emitter, the number of electrons emitted per second from 1 m^2 of surface with a z-component of velocity between v_z and $(v_z + dv_z)$ is[44]

$$dv_z = \frac{4m^2\pi kT}{h^3} e^{-\phi/kT} e^{-\frac{m}{2}v_z^2/kT} v_z\, dv_z$$

$$= \frac{Nm}{kT} e^{-\frac{m}{2}n_z^2/kT} v_z\, dv_z \qquad (3.25)$$

where ϕ is the work function of the metal and m is the electron mass. If the drift tube is at a potential V_d relative to the cathode (V_d is normally selected to maximize the slow electron fraction) then we want the number of electrons within a small energy range ΔE above V_d. In terms of velocity, we want $(m/2)v_z^2 = V_d$ and $\Delta E = (m/2)(v_z + \Delta v_z)^2 - (\frac{m}{2})v_z^2$. In all cases of interest, $v_z \gg \Delta v_z$ so that $\Delta E = mv_z\Delta v_z$; thus

$$\Delta v_z = \frac{\Delta E}{(2mV_d)^{1/2}} \quad . \qquad (3.26)$$

We then find, using Eq. (3.25), the number of electrons with energies between V_d and $V_d + \Delta E$, given by

$$\Delta N = \int_{v_z}^{v_z+\Delta v_z} dN_z = \left[-N\, e^{-\frac{m}{2}v_z^2/kT}\right]_{\sqrt{2V_d/m}}^{\sqrt{2V_d/m} + \Delta E/\sqrt{2mV_d}} . \quad (3.27)$$

Using the fact that $\Delta E/V_d \ll 1$ we can reduce this to

$$\Delta N = N\, e^{-V_d/kT}\, [-e^{-\Delta E/kT} + 1]$$

which upon using the approximation $e^{-x} = 1 - x$ becomes

$$N = \frac{N\Delta E}{kT}\, e^{-V_d/kT} .$$

Then we have

$$\frac{\Delta N}{N} = \frac{e^{-V_d/kT}}{kT}\, \Delta E = C(V_d)\Delta E . \quad (3.28)$$

The fraction that have energies of 10^{-7} eV or less is (assuming that V_d is kept quite close to zero):

$$\frac{\Delta N}{N} = \frac{10^{-7}\ \text{eV}}{0.4\ \text{eV}} = 2.5 \times 10^{-7} .$$

The fraction of these in the magnetic ground state is (following Witteborn's calculation[4]):

$$f_g = \exp\left[\frac{-\mu_B B}{kT}\left(1 - \frac{g_s}{2}\right)\right] \div Z_{rot} \quad (3.29)$$

where

$$Z_{rot} = \sum_{n=0}^{\infty} \sum_{s=-\frac{1}{2}}^{+1/2} \exp\left[\frac{-2\mu_B B}{kT}\left(n + \frac{1}{2} + \frac{sg_s}{2}\right)\right] \qquad (3.30)$$

and μ_B is the Bohr magneton, s is the spin quantum number, g_s is the spin g-factor, and n is the cyclotron state index. For our B of 4000 gauss we have $\mu_B B = 4.6 \times 10^{-5}$ eV $\ll$ kT so f_g simplifies to

$$f_g = \frac{1}{Z_{rot}} \approx \frac{\mu_B B}{kT} \approx \frac{4.6 \times 10^{-5} \text{ eV}}{0.4 \text{ eV}} \approx 10^{-4} \; . \qquad (3.31)$$

Thus the fraction of electrons usable for our experiment is

$$f \cong (2.5 \times 10^{-7})(10^{-4}) \approx 2.5 \times 10^{-11} \; .$$

Were there no enhancement of the low energy electron fraction by rethermalization, this would require rather large currents from the tunnel cathode in order to obtain a usable count rate.

3.3.3 Beam Handling System

The main components of the beam handling system are illustrated in Fig. 3.5, along with the biasing circuits for the drift tubes. Only the stationary drift tube was used in the present work.

The magnetic guide field is provided by a 10' long superconducting solenoid manufactured by Linde. It is operated in the persistent mode during runs. The solenoid is capable of a 1.0 kilogauss field; however, typical operating values are 30-40 gauss. The homogeneity is better than 1 part in 10^4 over the central 8 feet.

The high cathode field (4000-5000 gauss) needed for magnetic state separation is provided by a quadrupole configuration

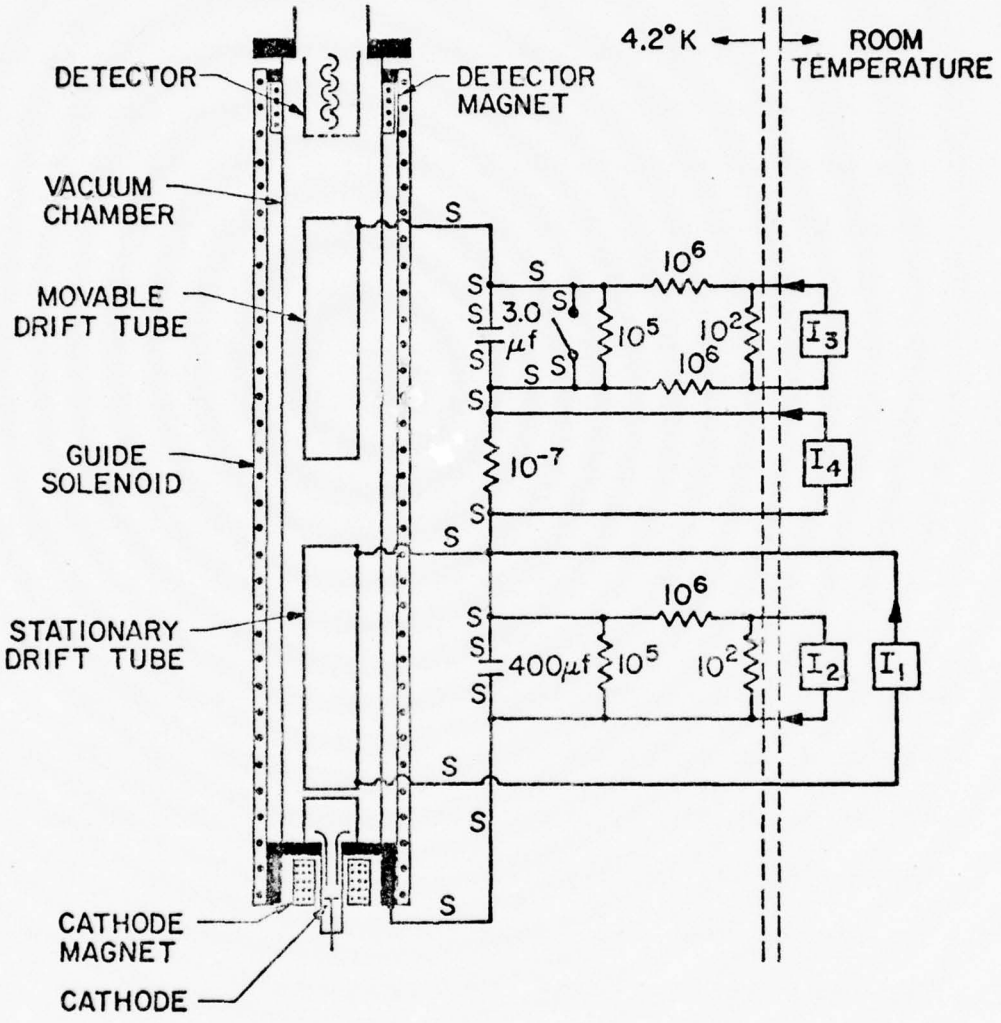


Fig. 3.5. A schematic diagram of the electron time-of-flight apparatus and the electrode biasing circuitry. Wires labeled s are superconducting. I_1-I_4 are constant current power supplies.

superconducting magnet, again operating in the persistent mode. This magnet was wound with Nb-Zr wire and is 2" long with a 1.25" bore. The quadrupole configuration is necessary in order to get the fringe field from the cathode magnet down to a very small value at the position of the lower (stationary) drift tube so that the magnetic potential seen by a ground state electron in the central portion of the drift tube does not vary by more than 10^{-12} eV.

A superconducting persistent mode quadrupole configuration detector magnet is used to reduce the net field at the detector below the value where significant magnetic field quenching of the detection efficiency occurs. This arrangement was found to be more satisfactory than merely terminating the guide solenoid below the detector entrance.

Magnetic field values are monitored by a system of bismuth magnetoresistors using 4-terminal constant current readouts. Magnetic fields from the Earth are reduced to less than 0.01 gauss over the flight path by two concentric Conetic® foil shields located just outside the dewar.

Typical magnetic and electric field profiles for the electron flight path are shown in Fig. 3.6. Electrical biasing is arranged so that the stationary drift tube is higher in (negative) potential than any other electrode near the flight path. This ensures that the electrons of interest travel slowly only inside the drift tube so that only the shielded portions of the flight path contribute significantly to the time of flight. The drift tube shields its interior from the large potentials present near the cathode and

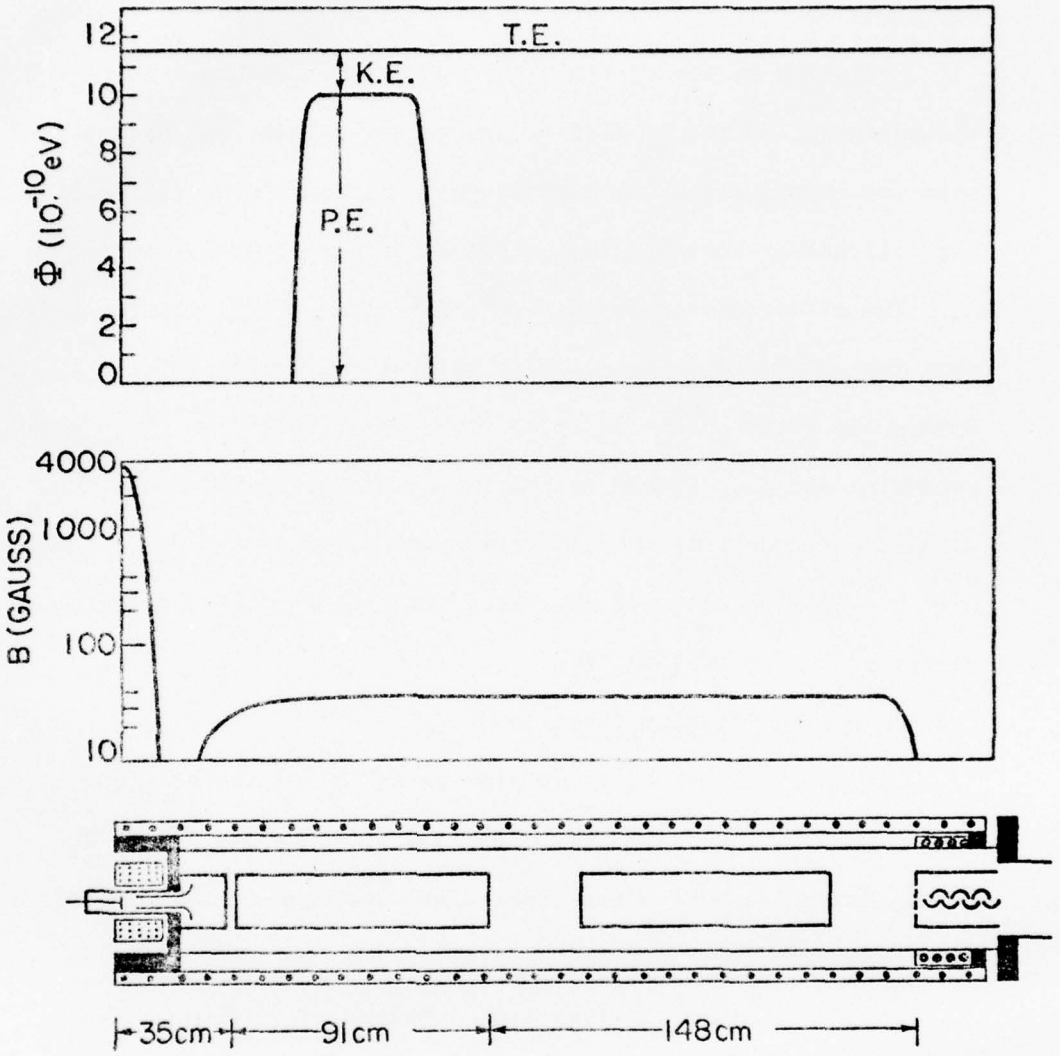


Fig. 3.6. The electric and magnetic field profiles along the electron flight path, which is illustrated in the bottom diagram. The top diagram shows the electric field profile typically used; it also shows the kinetic energy of an electron having a total energy of about 11.5×10^{-10} eV. The middle diagram shows on a logarithmic scale the magnetic field profile typically used.

detector to the extent that over at least a 50-cm length in the middle of the tube the electrostatic potential is flat to within a few parts in 10^{12}.

A diagram of the electron injector system is shown in Fig. 3.7. The potential of the Au film of the tunnel cathode can be adjusted relative to ground by the cathode pulse and bias circuit; pulsing is accomplished by lowering the potential of the Al film relative to the Au. The extractor serves to reduce the space charge retarding fields near the cathode and thus aids in obtaining good emission. The cathode shield and flare electrode shields the drift tube from the extractor potential and also serves to smooth the transition from the small diameter cathode region to the larger diameter of the drift tube.

The biasing circuits for the drift tube and the flare will be discussed in the next section.

3.3.4 Electrode Biasing Circuits

We will discuss only the bias circuits for the stationary drift tube and the flare; the movable drift tube was biased to ground potential during the experiments described in this thesis and was thus effectively not in the flight path.

The flare and drift tube bias circuits are similar to those designed by F. C. Witteborn for the electron free fall experiment. We have made a few changes in order to optimize the circuits for the experiments described in this thesis.

In order to avoid the deleterious effects of varying resistance in the bias supply leads, it was decided that all biasing would be done by using constant current sources to drive passive bias circuitry

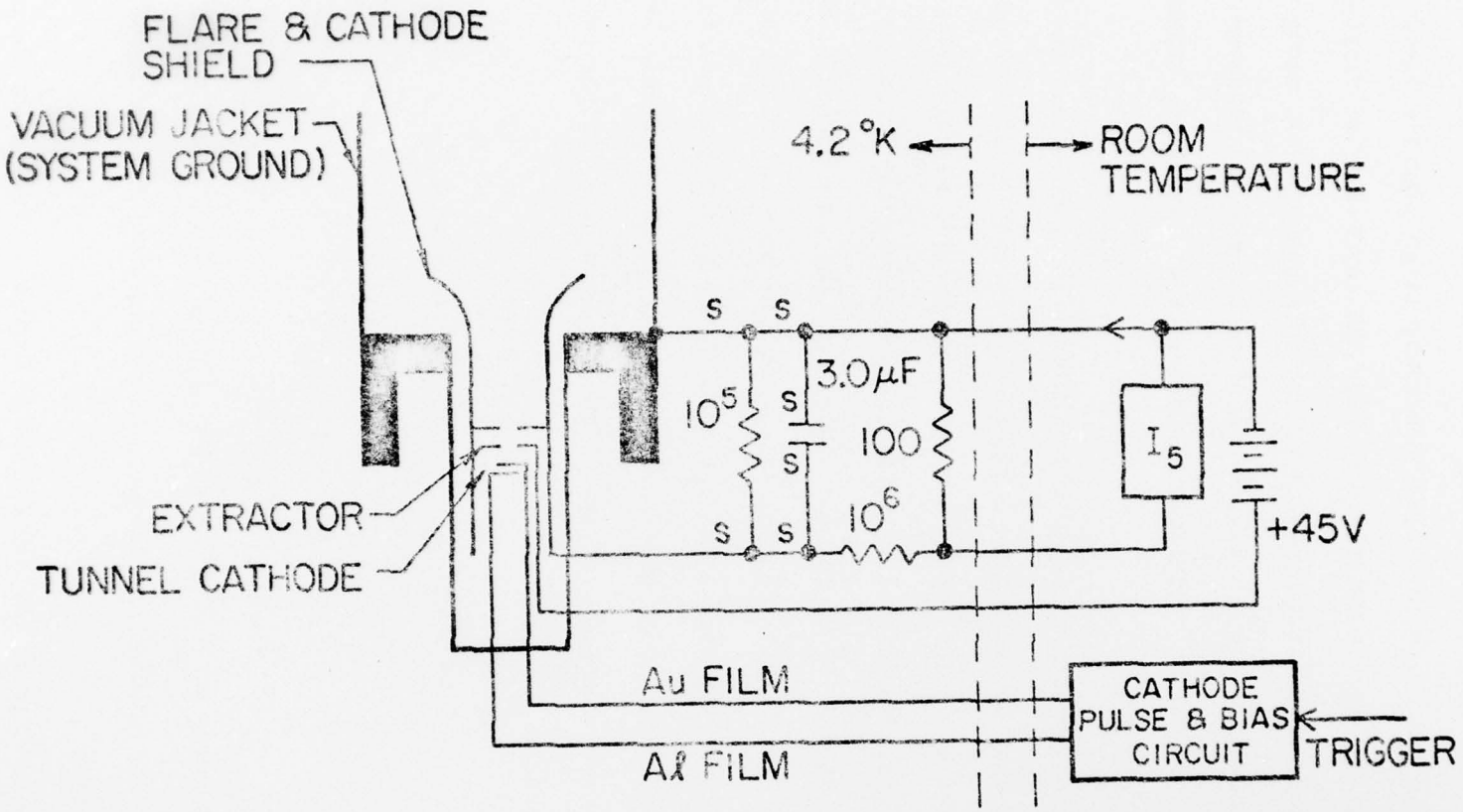


Fig. 3.7. The electron injection system. Wires labeled s are superconducting. I_5 is a constant current power supply.

located at a single level in the LHe bath. The currents used should be less than 1 A or so to avoid undesirably large magnetic fields from the wires. It is desirable to have the capability of varying the electrode potentials by 0.1 V or so; this requirement, along with the need to keep Joule heating to a minimum in order to conserve LHe, sets a minimum on the resistance between each electrode and ground of about 0.5 Ω.

The problem with using just a single resistor to obtain the bias voltage is that the resulting Johnson noise is too large. TOF experiments in the 10^{-11}-10^{-12} eV/m net force region will be adversely affected by sinusoidal noise voltage components having frequencies between 50 Hz and 10^{6} Hz (at the lower limit the tube potential does not change significantly during the passage of an electron while at the upper limit the time which the tube spends at the peaks of the sinusoid is small enough that the flight time of the electrons of interest is not changed greatly). Thus the Johnson noise per ohm of resistance is

$$\frac{\langle \Delta V^2 \rangle}{R} = 4\ kT\Delta f = (5.52 \times 10^{-23})(4.2)(10^{6}) \qquad (3.32)$$

$$\frac{\Delta V_{rms}}{\sqrt{R}} = 1.5 \times 10^{-8}\ \text{V} . \qquad (3.33)$$

Since we require $\Delta V_{rms} < 10^{-12}$ V, we could only use a 10^{-8} Ω or so resistor. The solution is to use some capacitance in parallel with the resistance.

Robinson[45] gives the Johnson noise across a complex impedance Z as

$$\langle \Delta V^2 \rangle = \int_{f_1}^{f_2} w(f)\, df \tag{3.34}$$

where $w(f) = 4\ kT\ Re(Z)$. If $1/Z = 1/R + j\omega C$ then

$$Re(Z) = \frac{R}{1+\omega^2 R^2 C^2} \quad .$$

Thus

$$\langle \Delta V^2 \rangle = \frac{4kTR}{2\pi} \int_{\omega_1}^{\omega_2} \frac{d\omega}{1+\omega^2 R^2 C^2}$$

$$= \frac{4kTR}{2\pi RC} \left[\tan^{-1} RC\omega\right]_{\omega_1}^{\omega_2} \quad . \tag{3.35}$$

Expanding $\tan^{-1} RC\omega$ and keeping the first two terms yields (for $\omega RC > 1$)

$$\langle \Delta V^2 \rangle = \frac{4kT}{2\pi RC^2} \left[\frac{1}{\omega_1} - \frac{1}{\omega_2}\right] \approx \frac{2kT}{\pi RC^2 \omega_1} \quad . \tag{3.36}$$

This interesting result says that by having some capacitance in parallel, we can use as large a value of R as we like. However, this assumes that there is no resistance in the leads of the capacitor. A more reasonable model is one in which each lead of the capacitor has a resistance $R_c/2$. For such a circuit we have

$$\frac{1}{Z} = \frac{1}{R} + \frac{1}{\left(\frac{1}{j\omega c} + R_c\right)}$$

which gives

$$\langle \Delta V^2 \rangle = \frac{4kTR}{2\pi} \int_{\omega_1}^{\omega_2} \left[1 - \frac{\omega^2 C^2 (R^2 + RR_c)}{\omega^2 C^2 (R+R_c)^2 + 1} \right] d\omega \ , \qquad (3.37)$$

yielding, under the same approximation used to obtain (3.36) and for $\omega RC > 1$ the result

$$\langle \Delta V^2 \rangle = \frac{4kTR}{2\pi} \left[\omega - \frac{\omega R}{(R+R_c)} + \frac{R}{C^2 (R+R_c)^3 \omega} \right]_{\omega_1}^{\omega_2} \ . \qquad (3.38)$$

If we assume $R_c/R \ll 1$ this becomes approximately

$$\langle \Delta V^2 \rangle \cong \frac{4kTR_c}{2\pi} \omega_2 + \frac{4kT}{2\pi RC^2 \omega_1} \ , \qquad (3.39)$$

so that by considering lead resistance we have essentially added to (3.36) an amount of noise $4kTR_c\omega_2/2\pi$; we saw in (3.33) that this would require $R_c < \sim 10^{-8}$ Ω in order to keep the noise below the necessary maximum. There is one way to obtain an even smaller R_c: make the capacitor superconducting. This is the basic idea behind the bais circuits of Fig. 3.5 in which all the wires labeled "S" (including the capacitors) are superconducting. The 10^5 Ω value of R and 400 μF capacitor in the bias circuit for the lower drift tube give from (3.36) a noise of

$$\Delta V_{rms} = \left[\frac{(5.52 \times 10^{-23})(4.2)}{10^5 (4 \times 10^{-4})^2 (50)} \right]^{1/2}$$

$$= 1.7 \times 10^{-11} \text{ V.}$$

This is not quite as small as we would like but is tolerable. Practical considerations limit the size of R and C.

The effectiveness of the superconducting capacitor in reducing the noise in the drift tube bias circuit is also limited by the inductance of the capacitor leads. The lead inductance can be shown[7] to be particularly important at noise frequencies above 10^4 Hz. Since our effective bandwidth for sensitivity to bias circuit noise extends to 10^6 Hz, the rms noise voltage observed on the drift tube will be somewhat larger than indicated above. However, the rms noise voltage obtained by adding the effects of lead inductance to Eq. (3.37) is still small enough to have a negligible effect on the experiments discussed here. Our conclusion about the great advantage which can be gained by making use of a large superconducting capacitor remains valid.

The 10^6 Ω resistor is present to attenuate by a factor of 10 any voltage noise present on the bias supply leads. The 100 Ω resistor forms a current divider which is used to reduce the voltage required from the current source.

A similar circuit is used to bias the flare (see Fig. 3.7). In the case of the flare, the considerably less stringent requirements on the amount of noise which can be tolerated allow the use of a much smaller superconducting capacitor.

The specially-constructed low-noise constant current sources used to power the bias circuits are shown in Fig. 3.8. These units have a stability against line and load variations of approximately one part in 10^5 and a ripple of less than 0.001%. Extreme precautions must be taken to minimize both differential mode and common mode noise on the outputs of these supplies. There are three separate current sources; each is totally surrounded by a shielding enclosure

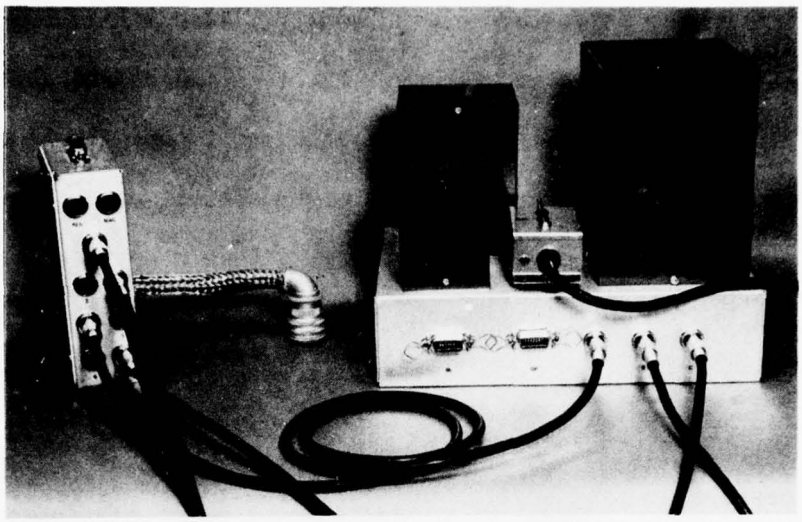


Fig. 3.8. The low-noise totally-shielded power supplies for the low-temperature bias circuits. The unit on the right contains three separate power supplies; the unit on the left is a distribution panel which allows each supply to power any one of several different bias circuits.

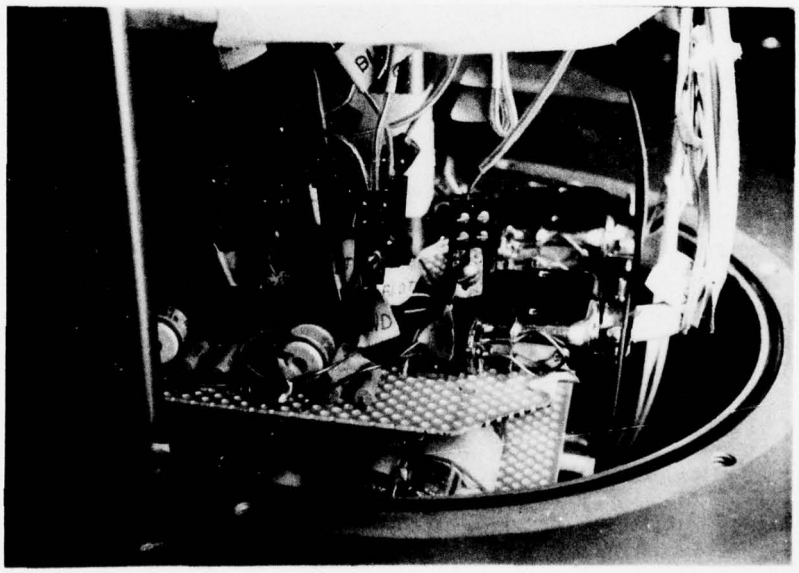


Fig. 3.9. The LHe bias circuit board in place below the bottom feedthrough flange of the high vacuum enclosure. Below the main circuit board is a second board which holds several superconducting capacitor assemblies.

whose only openings are those necessary for power and control leads. The output leads are balanced and have a non-current-carrying shield. Shielded connectors are used throughout. The power transformers in each supply have a triple electrostatic shield between the primary and secondary windings which reduces the coupling capacitance between windings to less than 10^{-14} F. The 110-V leads to the primary windings are also totally shielded; this power line shielding is completely independent of the output circuit shielding. The 110-V power for the three supplies is obtained from yet another triple shielded isolation transformer in order to further reduce common mode noise originating in the power line.

Figure 3.8 also shows the shielded distribution panel which allows any one of the three current sources to be bussed to any one of several different bias circuits. The different current sources vary in maximum output level and optimum control range; it is thus convenient to be able to utilize different supplies to power a given bias circuit as the experimental requirements change.

A totally-shielded remote control box is used to adjust and monitor the outputs of the current sources.

Figure 3.9 shows the circuit board on which the bias circuit components are mounted and a second board on which some of the superconducting capacitor assemblies are mounted. The 400 μF superconducting capacitor is mounted on the outside of the guide solenoid as shown in Fig. 3.2. We discussed earlier in this section the need for superconducting capacitors in order to keep Johnson noise to suitably low levels; we also use superconducting leads in other portions of the bias circuit for the same reason. In order to make

demountable connections from the circuit board to the electrodes inside the vacuum enclosure we employ superconducting mechanical clamps; these clamps can be seen in Fig. 3.9 and also in Fig. 3.10. In Fig. 3.10 the clamps are shown attached to the superconducting feedthroughs with which leads to the internal electrodes are brought out of the vacuum enclosure.

The axial drift tube current with which we apply force to electrons moving through the tube is furnished by the current source labeled I_1 in Fig. 3.5. This current source is extremely well filtered and regulated (one part in 10^5 stability against line and load variations and less than 0.001% ripple) and also has very high resolution. There is an additional lead to each end of the drift tube (not shown in Fig. 3.5) to permit the voltage developed along the drift tube to be monitored.

The vacuum enclosure serves as the instrumentation ground for the bias circuits. The actual ground connection is made at a single point on the massive feedthrough flange at the bottom of the vacuum enclosure.

3.3.5 Detector and Counting Electronics

A schematic of our detection and counting system is shown in Fig. 3.11. The detector is a windowless 14-stage photomultiplier. The first two dynodes are controlled by a separate high voltage supply which can be disabled by a pulse from the timing circuit. This allows a large multiplier gain reduction during the arrival of the large burst of electrons which follows each cathode pulse. This procedure is necessary to avoid overload of the amplifier and excessive heating of the dynodes.

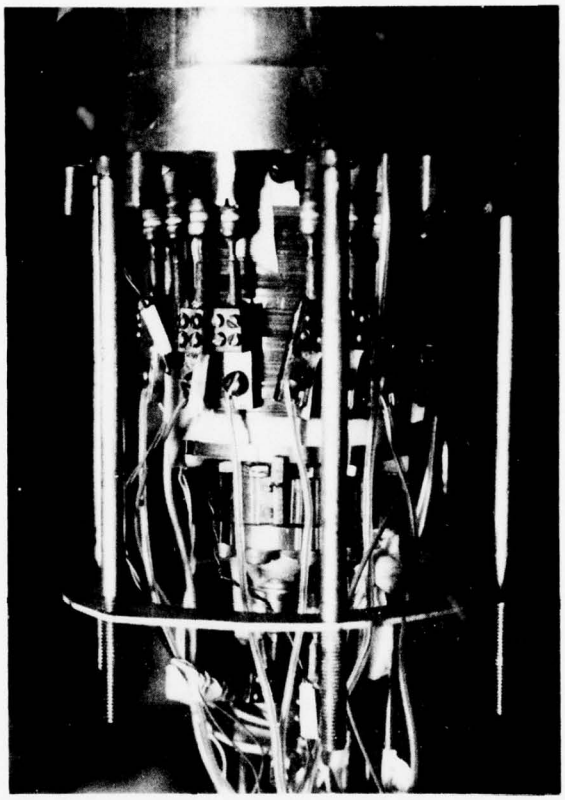


Fig. 3.10. A view of the bottom feedthrough flange showing several superconducting clamps attached to the superconducting feedthroughs.

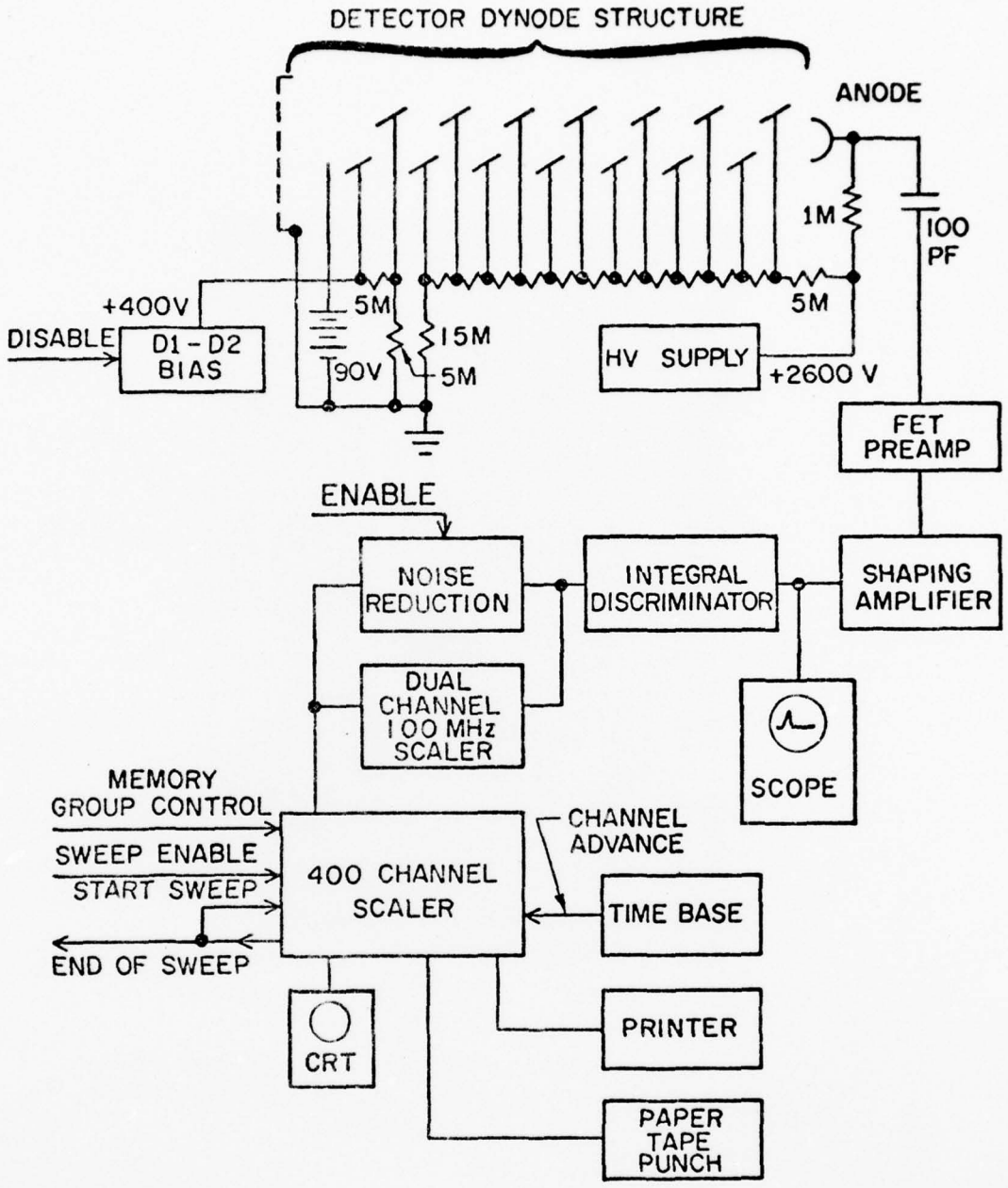


Fig. 3.11. The detector and counting electronics.

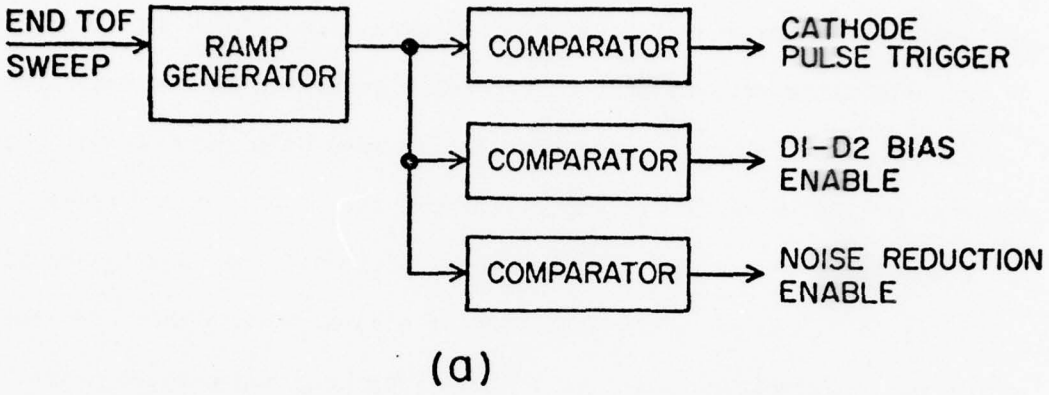
The preamplifier is a Tennelec TC164 FET charge-sensitive unit, while the shaping amplifier is a Canberra 1410. An Ortec integral discriminator removes most of the noise generated in the detection system. Further noise reduction is provided by a special unit which, when activated by the timing circuitry, allows only one further count to be accepted. The circuit is activated only during the TOF interval for which the probability of obtaining more than one real count is extremely small; it is reset for each new cathode pulse. The action of this circuit can be monitored with the 100 MHz dual channel scaler.

The TOF spectra are accumulated in 4 groups of 100 channels each in the 400 channel scaler. The memory group used is correlated with the value of axial drift tube current in use by the control electronics. The end of TOF sweep signal from the 400 channel scaler is fed back to the scaler to start a new sweep and is also sent to the timing circuit to initiate a new cathode pulse and subsequent operations. Data is both printed and punched in ASCII on paper tape.

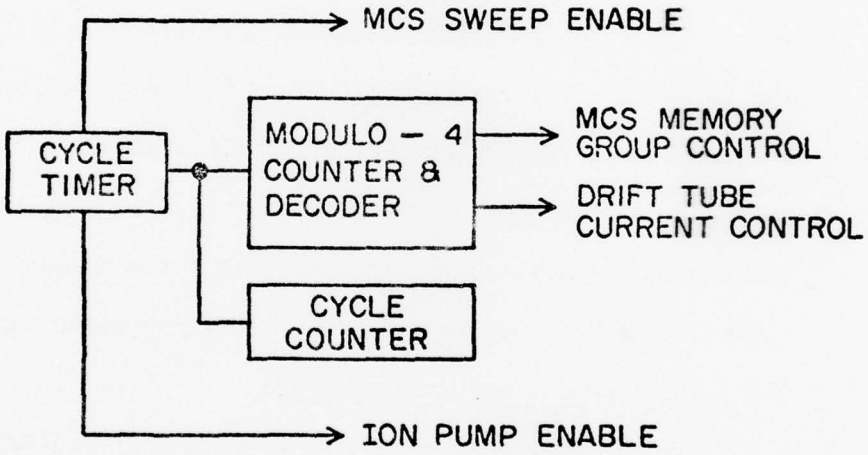
3.3.6 Timing and Control Electronics

The timing electronics are shown in Fig. 3.12(a). The end-of-sweep signal from the 400 channel scaler triggers a ramp generator. The cathode pulse trigger, D1-D2 detector bias enable signal, and noise reduction enable signal are obtained from comparators which are set to trigger when the ramp reaches the appropriate voltage.

The control electronics are shown in Fig. 3.12(b). A crystal-controlled timer starts a sub-run by first disabling the ion pump. At the same time a pulse is sent to a modulo-4 counter and decoder which determines both the value of applied axial current to be used



(a)



(b)

Fig. 3.12. The control electronics for the TOF experiments.

and the quadrant of the scaler memory in which the TOF spectrum will be stored. After an appropriate settling time, the multi-channel scaler sweep is enabled. TOF sweeps continue until the timer disables the MCS; at that time, the ion pump is turned on. At the end of the pumping period, the ion pump is disabled, the modulo-4 counter advances, and another sub-run is ready to begin. A cycle counter keeps track of the number of sun-runs which have been made. When sufficient data has been accumulated, the cycle is manually terminated.

3.4 Modifications for Room-Temperature and LN_2-Temperature Operation

The components inside the high vacuum system were not changed for the room-temperature and LN_2-temperature experiments. The principal changes were made in the magnet system and in the electrode biasing network.

A two-layer copper wire magnet was wound onto the full length of the vacuum jacket of the apparatus to serve as the guide solenoid. This magnet produces 15 gauss/A and is typically run at 5-10 gauss. When the main guide field is kept small it is not necessary to use a detector counter-magnet.

The room temperature cathode magnet is again a 2-layer copper wire magnet. Because of space limitations, it had to be wound over the lower portion of the superconducting solenoid. This magnet produces 14.2 gauss/A; at room temperature it was typically run at 70 gauss. Even at that modest field level a compressed air cooling system had to be installed to prevent excessive heating of the magnet.

Cooling was of course no problem in LN_2 operation; during that work cathode fields of 100-200 gauss were used.

There were two problems involved in getting good electrode bias circuits at 300°K. First, the superconducting capacitors could no longer be used, and second, kT was up by a factor of 75. On the other hand, the design sensitivity at room temperature was 10^{-8} eV/m rather than 10^{-12} eV/m. This meant that ΔV_{rms} could be as large as 10^{-8} V; also, the upper limit of the noise bandwidth became 10^4 Hz rather than 10^6 Hz. Using these values in Eq. (3.32) we obtain

$$\Delta V_{rms} = [(5.52 \times 10^{-23})(300)(10^4)R]^{1/2}$$

$$= 1.3 \times 10^{-8}\sqrt{R} \quad .$$

Thus we can use an R of 0.1 Ω or so. Since there is no need to conserve LHe, the resultant 0.1-0.2 W of heating is no problem. This is essentially the method that was used although it proved useful to incorporate some room temperature capacitance. As in the case of the LHe bias circuit, a 10-1 voltage divider was included in the circuit to attenuate noise on the bias supply leads. Again, well-shielded constant current sources with very good stability and low ripple were used to power the bias circuits.

3.5 Apparatus Modifications for Heated Drift Tube Experiments

In order to perform the heated drift tube experiments it was necessary to thermally isolate the drift tube and to install a heating and temperature monitor system. In particular, care had to be taken

to avoid large thermal gradients along the tube; otherwise an excessively high thermoelectric voltage would exists along the tube.

In the LHe version of the apparatus the (stationary) drift tube was thermally isolated except for one high-thermal-conductivity link from the lower end of the drift tube to the LHe bath. We removed this link in setting up for the heated drift tube work in order to obtain the desired degree of thermal isolation.

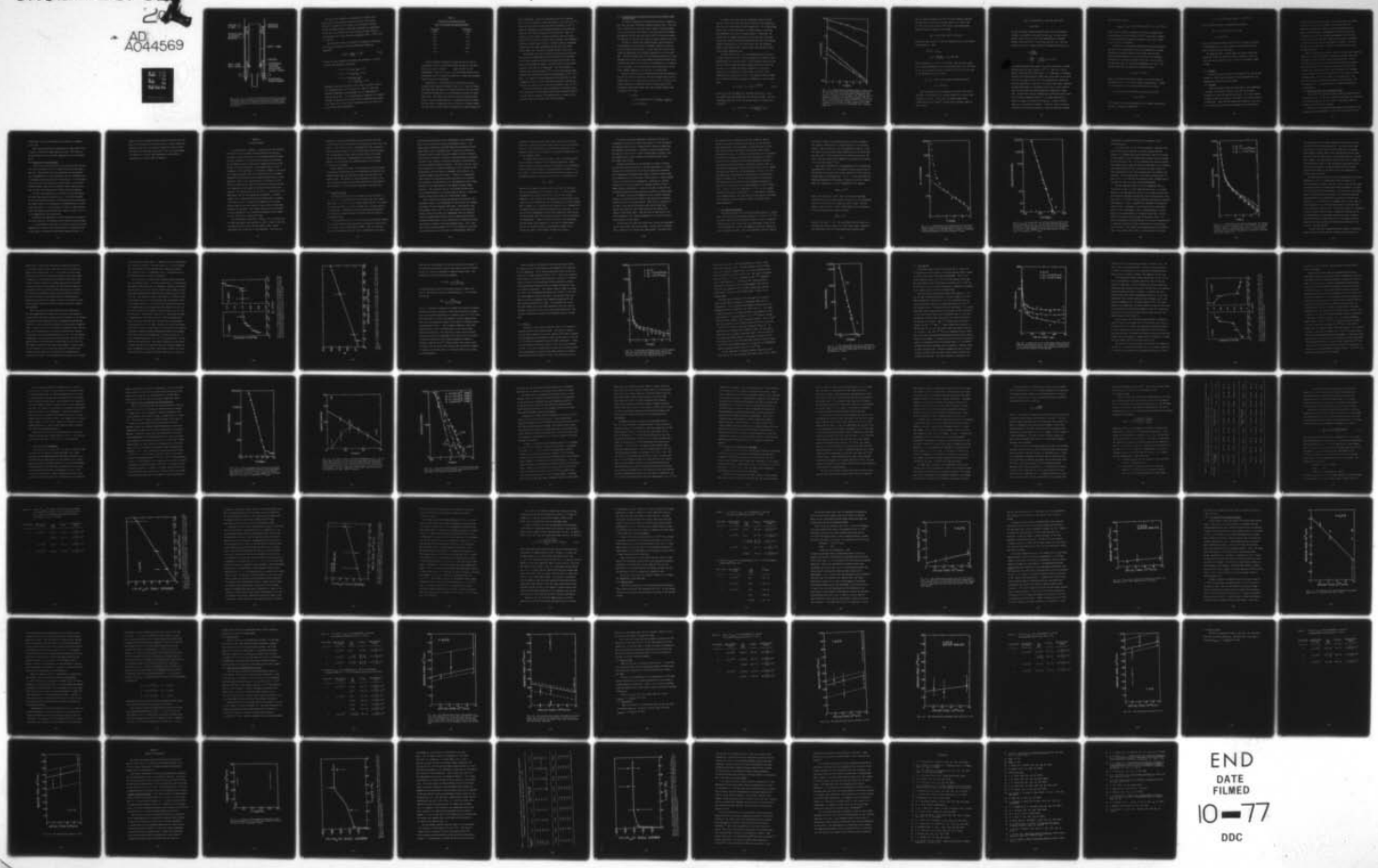
The small thermal conductivity which remains between the tube and the bath is due to the relatively low-thermal-conductivity links which are illustrated in Fig. 3.13; this figure also shows the location of the heater and monitor resistors.

As it turns out, the primary source of thermal conductance away from the tube is the set of four drift tube bias leads plus the leads to the heater and monitor resistors. The thermal conductance of the ceramiseal insulator and the ceramic balls is much smaller.

A 100 Ω metal film resistor is used as the heating element. This resistor has very robust leads which permit convenient heat sinking to the drift tube. Both leads are cut very short; one is securely fastened to the lower circumferential clamp. This clamp also serves to attach the lower set of bias leads to the tube. The other resistor lead is soldered to a #24 copper wire which goes to a feedthrough. This resistor has a very small variation of resistance with temperature. Thus, by driving the resistor with a constant current source we can put a known amount of power into the heater. The heater-drift tube system will then come to an equilibrium temperature which can be controlled by varying the power input.

AD-A044 569 STANFORD UNIV CA LOW TEMPERATURE PHYSICS GROUP F/G 20/3
EXPERIMENTAL EVIDENCE FOR A TEMPERATURE-DEPENDENT SURFACE SHIEL--ETC(U)
AUG 77 J M LOCKHART F44620-75-C-0022
UNCLASSIFIED AFOSR-TR-77-1208 NL

2 OF 2
AD A044569



END
DATE FILMED
10-77
DDC

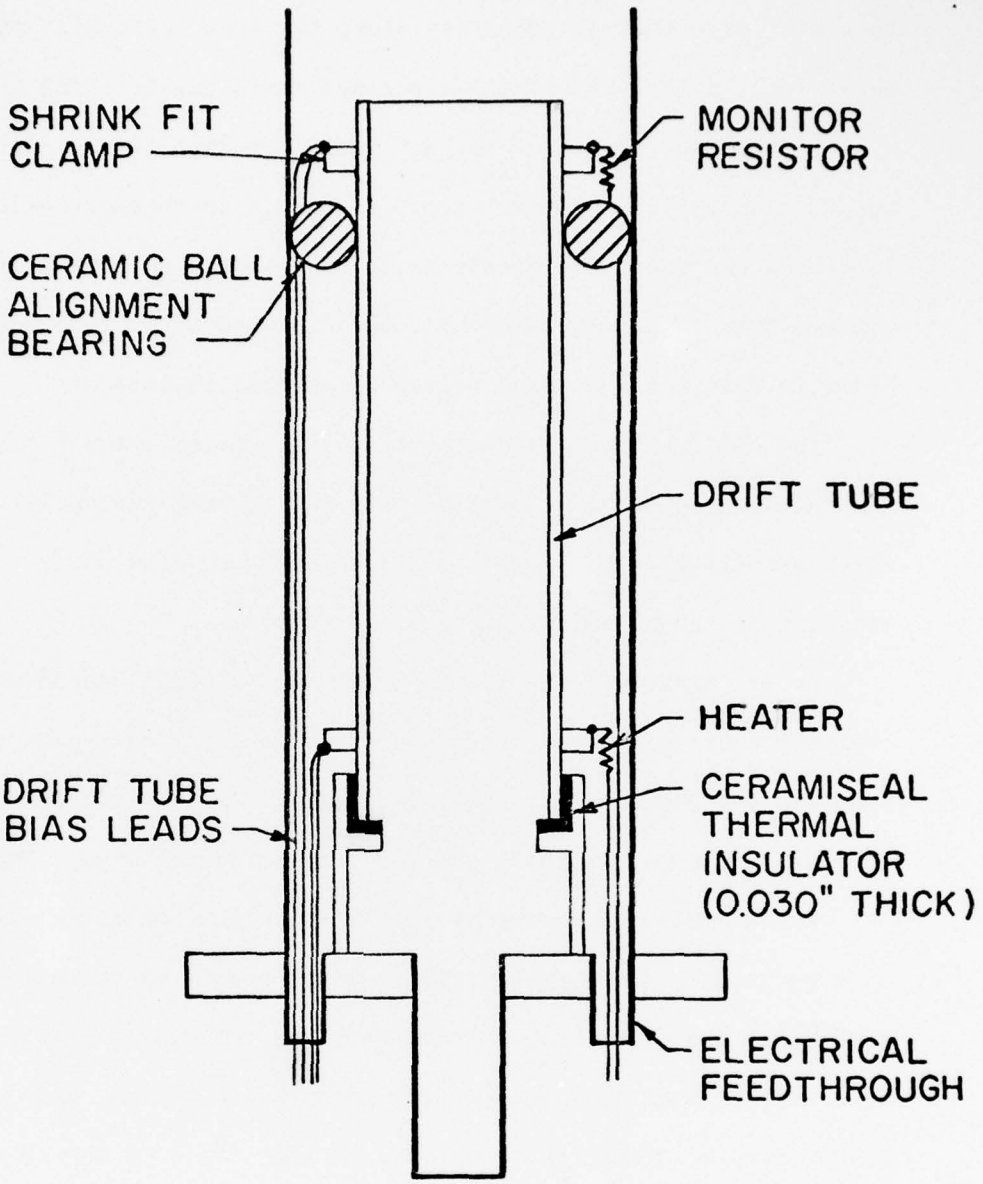


Fig. 3.13. A cross section of the drift tube area (not to scale) showing the thermal insulation of the tube, the principal sources of thermal conductivity between the tube and the LHe bath which surrounds the apparatus, and the location of the heater and monitor resistors.

The drift tube temperature is monitored by a nominal 650 Ω carbon resistor from which the ceramic casing has been removed. A precisely regulated 10^{-5} A current is run through the resistor and the resulting voltage is monitored to determine the temperature of the tube. The resistor has a LHe resistance of about 20 KΩ, so self-heating by the readout current is negligible ($I^2R = 10^{-10}(2 \times 10^4) = 2 \times 10^{-6}$ W).

This resistance value is converted to a temperature through the use of the semi-empirical equation developed by Clement and Quinnell[46]:

$$\log_{10} R + \frac{k}{\log_{10} R} = A + \frac{B}{T} . \qquad (3.40)$$

We also use their method for determining the constants A, B, and K from the room temperature resistance:

$$A \pm 3\% = 1.62 \log_{10} R_{290} + 0.27$$

$$B \pm 9\% = 1.60 \log_{10} R_{290} + 0.48$$

$$K \pm 6\% = 0.594(\log_{10} R_{290})^2 + 0.377 \log_{10} R_{290} - 0.121$$

although we adjust the constants a bit to get the correct values at our calibration points of 77°K and 4.2°K. Table 3.1 shows the resistance-temperature correspondences for the temperatures at which we report data. It was experimentally determined by a sequence of checks on the monitor resistance that the temperature was stable to at least 0.01°K at the lower temperatures and to at least 0.1°K at the three higher temperatures.

TABLE 3.1

TEMPERATURE CALIBRATION FOR OUR

DRIFT TUBE TEMPERATURE MONITOR RESISTOR

Resistance (KΩ)	Temperature (°K)
24.0	4.20
23.0	4.27
20.9	4.44
9.6	6.35
5.4	8.95
4.0	11.0

We must consider the possibility that the circuit used to apply power to the drift tube heater might add noise to the drift tube bias circuit in amounts large enough to affect the TOF measurements. Since such an effect would presumably depend on the heater power level, it might be mistaken for a temperature-dependent ambient field in the drift tube.

Heater power is supplied by one of the low-noise totally-shielded current sources described in Sec. 3.3.4. Only the common-mode noise from the supply is of concern here since the only effect of differential-mode noise is to cause minute variations in heater power level. The supply uses linear dissipative regulation exclusively so that no common-mode noise is generated within the supply. The main source of common-mode noise is thus 60 Hz leakage currents and power line transients which are capacitively coupled through the

power transformer. Since the transformers used in our supplies have a primary-secondary coupling capacitance of less than 4×10^{-15} F while the capacitance from the drift tube to ground is 4×10^{-4} F, potentials appearing on the transformer primary are attenuated by a factor of 10^{11} before they appear on the drift tube. Thus, for example, the 60 Hz ripple voltage on the drift tube will be less than 10^{-9} V rms; noise on the drift tube from power line transients should not be much larger (there is a second isolation transformer between the power supply transformer and the power line which reduces power line transients by another factor of 100 or so).

The presence of a noise voltage on the lower end of the drift tube because of common-mode noise on the heater circuit produces both a slight change in the drift tube bias potential and a very small voltage along the length of the tube (since the bias circuit connects to the tube at its upper end). The latter effect is insignificant since only about 10^{-15} V is produced along the tube, while we are working with electrons having energies of 10^{-11} eV or more. The change in the bias potential of the drift tube is also unimportant since the velocity spectrum of electrons entering the tube does not change when the drift tube potential varies by 10^{-9} V.

We thus conclude that noise introduced by the heating circuit will not perturb TOF measurements which study the ambient fields in the tube when the ambient field magnitudes are as large as those which we found in the heated drift tube experiments.

3.5.1 Determination of the Thermoelectric Potential Gradient along the Drift Tube

In order to determine the thermoelectric potential gradient we must first determine the thermal gradient along the tube. Since the tube is heated only at the lower end, we expect a thermal gradient to be set up along the tube because of the small but finite thermal conductivity from the top of the tube to the 4.2°K bath and because the lower part of the tube must supply the power radiated by the top.

In order to calculate the thermal gradient expected from the first mechanism we need to know the thermal conductivity from the top of the tube to the LHe bath. We will find this by first calculating the approximate total thermal conductivity out of the drift tube. We can check the result of this calculation against the result obtained from an analysis of experimentally-determined thermal decay curves for the drift tube and adjust the coefficients in the calculation as necessary. We can thus obtain a good approximation to the actual thermal conductivity out the top of the drift tube.

For our calculation we will assume that the thermal conductivity away from the tube is provided by 3 15-cm #24 copper wires (0.25 cm radius) and 3 1-m #24 copper wires (see Fig. 3.13). We will use the thermal conductivity coefficient given by Stewart et al.[47] for electrolytic tough pitch copper (the type of copper normally used in wires) at 6°K. Thus

$$K = \lambda A/L$$

$$= (4.8\ \text{W-cm/°K})(3\pi)(.025\ \text{cm})^2\left(\frac{1}{15\ \text{cm}} + \frac{1}{100\ \text{cm}}\right)$$

$$= 2.2 \times 10^{-3}\ \text{W/°K}\ .$$

To compare this value with the experimental result we start with Fig. 3.14, which shows the decay of the drift tube temperature with time for four different initial temperatures. It is interesting to note that in each case there is a slight increase in the drift tube temperature just after the heating power is turned off. We assume that this happens because the ends of the small wires near the LHe cool slightly before the heating resistor, thus lowering the thermal conductivity out of the drift tube a bit; the resulting change in the amount of heat conducted away from the heater causes a very slight temperature rise.

The lines shown in Fig. 3.14 are exponential fits to all but the first point of each set. Obviously each of these decays is well represented by an exponential decay. Since the heat capacity of the tube is orders of magnitude larger than the total heat capacity of the wires, we can model the initial situation as a large heat capacity at T_i connected by a large thermal resistance (small conductance) to a heat sink at 4.2°K. The problem is then the same as the decay of the initial voltage on a capacitor in an RC circuit. Thus

$$(T - 4.2°K) = (T_i - 4.2°K)\, e^{-t/R_t C_{DT}} \qquad (3.41)$$

where C_{DT} is the heat capacity of the drift tube and $R_t = 1/K$ is the thermal resistance between the tube and the LHe bath. Over the temperature range 0°K to 10°K the specific heat of Cu follows the equation[48]

$$C_p = 10.8 \times 10^{-6}\, T + 30.6 \left[\frac{T}{344.5}\right]^3 \text{ J/g-°K} .$$

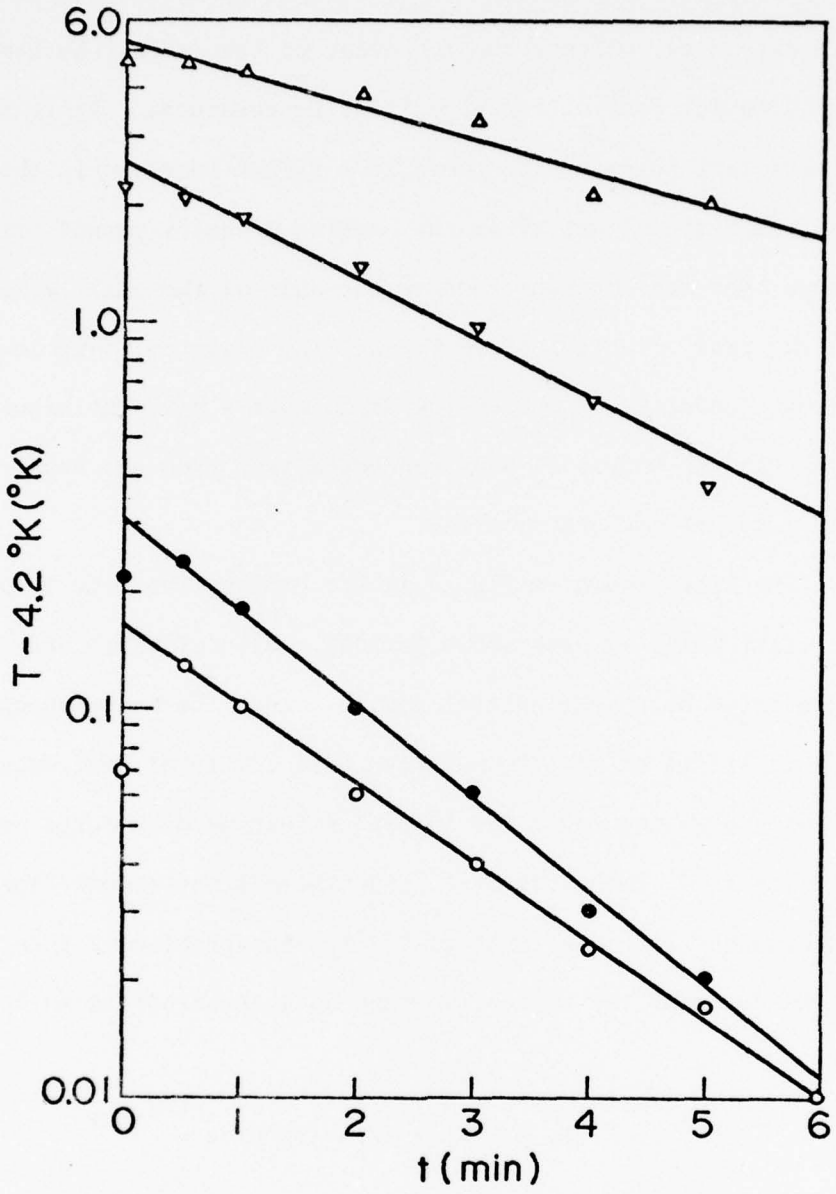


Fig. 3.14. Experimentally-determined thermal decay curves for the drift tube. The curves were obtained by heating the tube until the desired equilibrium temperature was reached, switching off heater power, and observing the temperature of the tube as a function of elapsed time. The circles correspond to an initial temperature of 4.3°K, the dots 4.4°K, the downward triangles 6.3°K, and the upward triangles 9°K. The lines are least squares fits to the points of each set for which the elapsed time is greater than zero.

Over our range of interest of 4.2°K to 9°K this equation indicates that the specific heat will be between about 1×10^{-4} J/g-°K and 6×10^{-4} J/g-°K; we will take 4×10^{-4} J/g-°K as an average value. The drift tube has a mass of 4.1 kg; thus

$$C_{DT} = (4 \times 10^{-4})(4.1 \times 10^{3}) = 1.64 \text{ J/°K} .$$

The decay curves of Fig. 3.14 are all consistent with a time constant of about 800 sec. Thus

$$800 \text{ sec} = R_t \, C_{DT}$$

$$R_{DT} = \frac{800 \text{ sec}}{1.64 \text{ J/°K}} = 4.9 \times 10^{2} \text{ °K/W}$$

which corresponds to a K of 2.0×10^{-3} W/°K. Note that this result is in excellent agreement with our calculated value of 2.2×10^{-3} W/°K. We can now calculate the thermal resistance from the top of the tube to the LHe bath via the bias leads:

$$R_{t1} = \frac{1}{K_1} = [(4.8 \text{ W-cm/°K})(3\pi)(.025 \text{ cm})^2(1/100 \text{ cm})]^{-1}$$

$$= 3.5 \times 10^{3} \text{ °K/W} .$$

Next we need the thermal resistance of the drift tube itself. The tube is 91 cm long, with an average radius of 2.7 cm and a wall thickness of 0.38 cm. Thus, using the thermal conductivity coefficient given by Stewart[47] for high purity annealed copper at 6°K, we have

$$R_{tDT} = [(96\ W/cm°K)2\pi(2.7\ cm)(0.38\ cm)/91\ cm]^{-1}$$

$$= 0.15\ °K/W\ .$$

To find the thermal gradient along the drift tube we can view the situation as a thermal resistance of value $R_{t\,DT}$ in series with a thermal resistance of R_{t1}; the series combination is connected between a heat reservoir at T and a heat sink at 4.2°K. Then the fraction of the total thermal gradient that appears across $R_{t\,DT}$ is

$$f = \frac{R_{tDT}}{R_{tDT}+R_{t1}}$$

$$\approx \frac{R_{tDT}}{R_{t1}} = \frac{0.15}{3.5\times10^{3}} = 4.3\times10^{-5}\ .$$

Thus when the bottom of the tube is at 6.3°K we would have a thermal gradient along the tube of about 9×10^{-5} °K. From Fig. 1 of the paper by Gold et al.[49] we deduce that -2μV/°K represents a reasonable estimate of the thermoelectric coefficient of the copper in our drift tube over the range 4.2°K to 11°K. The thermoelectfic coefficient would be significantly larger only if the drift tube copper contained an appreciable impurity concentration of Fe; this is quite unlikely since the drift tube was electroformed from a high-purity copper bath. On the other hand, the thermoelectric coefficient could be more than an order of magnitude smaller if our copper happened to be similar to sample 1 discussed by Gold et al. A value of -2μV/°K seems to be a conservative estimate. Using this value we obtain an estimate of the Thomson thermoelectric potential difference between

the ends of the tube of

$$\phi_{bottom} - \phi_{top} = (2.0 \times 10^{-6})(4.3 \times 10^{-5}) = 8.6 \times 10^{-11} \text{ V/°K.}$$

Thus even at our highest temperature of 11°K the thermoelectric potential gradient would be only 6×10^{-10} V, quite small compared to our observed ambient potential different in the tube of about 5×10^{-7} V at 6.3°K and above.

We have not yet considered radiation from the upper portion of the tube. For a rough upper limit to the thermoelectric voltage developed by radiation effects we will assume that the power radiated by the upper half of the drift tube must be furnished through the full thermal resistance of the tube. We will look at the radiation effect at the highest temperature used, 11°K. The radiated power from the upper half of the drift tube is

$$\Delta P = \varepsilon\sigma(T - 4.2°K)^4 \, A$$

where σ is the Stefan-Boltzmann constant, ε is the emissivity of the copper surface, and A is the effective radiating area. Taking 0.1 as a conservative emissivity for the drift tube we have

$$\Delta P = (0.1)(5.67 \times 10^{-8} \text{ W/m}^2\text{°K}^4)(2\pi)(.027 \text{ m})(0.5 \text{ m})(7°K)^4$$

$$= 1.15 \times 10^{-6} \text{ W} .$$

If this power is to be drawn through the full thermal resistance of the tube, a temperature gradient of

$$\Delta T = (1.15 \times 10^{-6} \text{ W})(0.15 \text{ °K/W}) = 1.7 \times 10^{-7} \text{ °K}$$

will be produced and thus a thermoelectric voltage of

$$\Delta\phi = (2.0 \times 10^{-6} \text{ V/°K})(1.7 \times 10^{-7} \text{ °K})$$

$$= 3.4 \times 10^{-13} \text{ V}$$

will result from the radiation effect; this is negligible compared to the thermoelectric voltage produced by the thermal conduction away from the top of the drift tube.

We should add that a limited amount of thermal conductivity between the drift tube and the LHe bath is desirable so that the drift tube can be allowed to cool to 4.2°K in a reasonable length of time.

3.6 Procedure

We will first discuss the basic procedure for LHe runs and then mention the differences encountered in the room temperature, LN_2 temperature, and heated drift tube work.

3.6.1 LHe Runs

After all possible checks have been made at room temperature, a cooldown is started by sealing the LHe space of the dewar, evacuating it, and refilling with dry N_2 gas. It is then possible to begin filling the LN_2 jacket of the dewar; this process requires several hours. Jacket boiloff remains quite high for 2 days or so. At the end of this period the pre-cooling can be accelerated by

transferring LN_2 into the LHe space. When the apparatus has cooled to 77°K most of the excess nitrogen is back-transferred; the remainder is pumped out in order to drop the temperature in the dewar a few more degrees. (Temperature at the top outer portion is monitored with an iron-constantan thermocouple and at the lower inner area by carbon resistors.) When the LN_2 is gone the LHe space is filled with He gas and the LHe transfer is started. The first LHe fill requires 8-12 hours. LHe level is checked with a set of 27 carbon resistors.

Next the electron beam system is turned on and the superconducting magnets are charged, adjusted for optimum slow electron count rate and magnetic state selection, and then made persistent. At this point the electrode biases are set and the discriminator and amplifiers are adjusted. The timing electronics are set to give the desired pulse sequencing and the control electronics are arranged to cycle through four selected values of drift tube current (always including zero). We are then ready to begin taking runs. The persistent magnets are checked periodically for field decay. The ion pump control is arranged so that it is always off when data is being taken.

3.6.2 Room Temperature and LN_2 Temperature Runs

In this work the copper wire magnets and room temperature bias circuits are used. In the room temperature experiments the compressed air cooling system must be used if even a very modest degree of magnetic state selection is desired.

Because of the considerably higher residual gas pressure in the apparatus at these temperatures ($\sim 10^{-9}$ Torr) we can run only on a

30-50% duty cycle; the ion pump must be on during the remainder of the time.

Since these experiments use applied forces larger than 10^{-7} eV in general, shorter TOF sweep times can be used. This speeds up the data collection rate and helps compensate for the limited duty cycle.

3.6.3 Heated Drift Tube Experiments

These runs were quite similar to the LHe runs except that the drift tube temperature had to be established and monitored before each run. Each time the drift tube temperature was increased we saw a considerable rise in the residual gas pressure (presumably due to desorption of gas from the drift tube surface). It was necessary to wait for this excess pressure to subside before a run could be started; however, this time was profitably used in making certain that the drift tube temperature had indeed reached equilibrium.

The drift tube temperature was rechecked periodically during the short time intervals between sub-runs. It was not desirable to have the temperature monitor circuit hooked up during the actual TOF sweeps because of the possibility of introducing noise into the drift tube circuit. It was necessary, of course, to apply heating power continuously; the noise from this source was shown in Sec. 3.5 to be unimportant for the present work.

The drift tube temperature was always observed and recorded at the end of each run. The thermal stability proved to be quite good.

It is undesirable to take all of the data at a given drift tube temperature at one time since long-term shifts in experimental conditions might be mistaken for temperature-dependent effects. In

taking our data we normally alternated between runs with the drift tube at 4.2°K and runs with the drift tube at a higher temperature although in some cases we alternated between two values of drift tube temperature which were larger than 4.2°K. We cycled through the complete set of drift tube temperatures several times in accumulating the data presented in Chapter 4.

CHAPTER 4

DATA AND ANALYSIS

As we pointed out in Chapter 1, a large part of the motivation for the series of experiments described herein arose from the discrepancy between the results of the Witteborn-Fairbank electron free-fall experiment on one hand and the theoretical predictions for the ambient electric field inside a copper drift tube and the results of the room temperature strain-induced electric field experiments on the other hand. We discussed in Chapter 2 the nature of a surface shielding effect which could resolve the discrepancy between the WF experiment and the theoretical predictions; we also pointed out that if this shielding effect is operative at 4.2°K but not at 300°K the discrepancy between the WF experiment and the room temperature strain-induced field measurements would also be resolved. The combination of all the results — the WF result, the DMRT theory, and the room temperature measurements — strongly suggests that a temperature-dependent shielding effect is present in the tube and that consequently the magnitude of the ambient electric field in the tube changes by several orders of magnitude between 4.2°K and 300°K. This chapter presents the data obtained in our investigation of the temperature dependence of the ambient electric field inside a copper drift tube.

Our investigation proceeded as follows: first, electron time-of-flight experiments were conducted at 300°K in order to check for the presence of the surface shielding effect; next, similar experiments were carried out at LN_2 temperature. This work was

followed by a return to LHe operation in order to make sure that we could obtain 4.2°K data similar to that obtained by WF in 1967. The success of the 4.2°K work led to the heated drift tube experiments which explored the range 4.2°K-11°K and found the transition region for the appearance of large ambient electric fields in the tube (and thus presumably the disappearance of the surface shielding effect). We will present the experimental data in the sequence in which it was obtained.

Before turning to the data, we will present a brief discussion of the nature of electrons which are emitted from electrostatic and magnetic traps along the beam path at times after the end of the cathode pulse. The presence of trap-originating electrons in the TOF distribution greatly modifies both the form of the distribution and the effect of a linear potential gradient in the drift tube.

4.1 Trapped Electrons

One feature which seems to be present in all our TOF data is the existence of many more electrons with long flight times than we would expect on the basis of the cathode energy spectrum. We presume that this enhancement of the slow electron flux is brought about by two mechanisms: rethermalization of the electron beam emitted by the cathode and delayed emission of electrons from electrostatic and magnetic traps.

As we discussed in Sec. 3.3.2, electrons emitted from the cathode have a modified Maxwellian distribution of velocities characteristic of a thermal source at approximately 5000°K. Once the electrons have left the cathode, they will tend to rethermalize to an energy

distribution characteristic of the temperature of the surrounding walls (4.2°K) if they are acted on by dissipative forces. (An application of Liouville's theorem[50] shows that conservative forces cannot effect such a rethermalization.) Sources of an effective dissipative force include three-body electron collisions (actually multi-electron collisions in general), electron-residual gas molecule collisions, eddy currents in the drift tube walls, and interaction with the background blackbody radiation. The next to the last source can be shown to be of negligible importance in the situation of the WF experiment; the last source is important only because it can stimulate changes of cyclotron state. If there is an appreciable cross-section for three-body electron collisions or for electron-gas collisions, we would expect to see the proportion of low energy electrons in the beam increase at the expense of higher energy electrons. The particular regions of the energy spectrum which will be affected most will of course depend on the way in which the relevant cross-sections vary with center-of-mass energy.

Multi-electron and electron-gas molecule collisions are also presumably central to the enhancement of slow electron flux through the process of delayed emission from traps. Electrostatic traps having depths of up to 10^{-6} eV or so may exist in the drift tube because of the patch effect (at temperatures where the anomalous surface shielding effect does not exist); larger traps may exist outside the tube because of the interaction of fringing fields from the various electrodes of the beam handling system. Also, a magnetic trap of potential depth 5×10^{-7} eV for electrons in the first excited cyclotron state (the depth is correspondingly larger for

electrons in higher cyclotron states) often existed just below the drift tube. Electrons can enter either kind of trap via an inelastic collision with a gas molecule, a multi-electron collision, or a change of cyclotron state stimulated by background radiation (in the case of a magnetic trap).

We assume that electrons will leave a trap via either electron-gas collisions or interaction with background radiation. (Multi-electron collisions do not constitute an important ejection mechanism since a given trap is unlikely to have more than one electron in it at a time.) In either case the number dn of electrons which will be ejected from traps of a given kind in the short time interval dt is

$$dn = - \lambda N \, dt$$

where N is the number of electrons in all the traps of the given kind at the beginning of the interval dt and λ is a decay constant determined by the type of trap and the nature of the ejection mechanism. Thus we expect that the number of electrons emitted from traps will decay exponentially with the elapsed time since the cathode pulse (actually in the general case the decay will be a superposition of exponential decays which have different decay constants). In the case of the TOF experiments we had on the average less than one slow electron (whether from direct cathode emission or from trap emission) per cathode pulse. However, the distribution of trap-originating electron flight times obtained over thousands of cathode pulses follows the exponential decay law nevertheless because of the statistical nature of the trapped electron decay process.

If one type of ejection mechanism is prevalent there will be an exponential decay with a single time constant; if other mechanisms are important there will be a superposition of decaying exponentials with different time constants. In general electrons emerging from the traps will tend to have a rather limited range of energies, with the maximum energy closely related to the potential depth of the most common type of trap.

Electrons which arrive at the detector as a result of delayed emission from traps will show up in the TOF distribution as a sudden increase in the electron flux at a time of flight value determined by the maximum of the normal energy range of electrons leaving traps. This increased flux will then decay in time either as a single exponential or as a combination of exponentials. There may be a further variation in the arrival times of the delayed electrons if their energy spread is significant. In most of our work it appeared that the energy spread of the trap-originating electrons was rather small.

The effect on the TOF distribution of slow electrons obtained through rethermalization will depend on the nature of the prevalent source of effective dissipative force. About the only statement we can make is that the TOF distribution will tend to decay more rapidly than normal at short flight times and less rapidly than normal at long flight times. There may also be small peaks in the TOF distribution if the energy dependences of the various collision cross-sections are not smooth.

We have seen that there are several ways in which an enhancement of the slow electron flux can come about. On the whole the enhancement is useful for our ambient force measurements. Electrons which

are slowed down by a dissipative force will respond to applied forces in the tube in essentially the same way as slow electrons which come directly from the cathode; in particular they will not smear out the sharp cutoff effects which applied forces should theoretically produce. The flux of these electrons will be decreased by an applied retarding force in the tube; thus they are useful in ambient force measurements made with the differential technique. Slow electrons emitted from traps, while they do tend to smear out any otherwise sharp cutoffs (because they are emitted with an unknown time delay with respect to the cathode pulse), are also useful for the ambient force measurements since their flux is reduced by an applied retarding force. We will see in the next few sections of this chapter that the response of trap-originating electrons to applied forces can provide a considerable amount of useful information. In fact, in the room temperature and 77°K work the apparent existence of reasonably large numbers of trap-originating electrons in the distribution may have been crucial to our success in obtaining some information about the ambient fields in the drift tube at those temperatures.

4.2 Room Temperature Results

The room temperature electron time-of-flight experiments studied drift tube electric fields ranging from about 10^{-7} V/m to 5×10^{-5} V/m. The lower limit on the fields studied is about 4 orders of magnitude larger than the lower limit in the 4.2°K experiments because of the several disadvantages of the room temperature system as compared to the low temperature system. The room temperature operation suffered

from poorer vacuum, noisier biasing circuits for the electrodes, and a greatly reduced ability to provide magnetic state selection. However, since the purpose of the room temperature work was to look for lattice distortion and/or patch effect fields in the drift tube, the lower limit on field sensitivity was adequate since one or the other of the two ambient field components was expected to be present at a level higher than 10^{-7} V/m.

Data from a representative room temperature run is plotted semi-logarithmically in Fig. 4.1. The number of counts which arrived at the detector in a 50 μsec time interval centered on time t after the cathode pulse is plotted against t. For t = 1.5 msec and beyond the functional dependence of the number of counts per (50 μsec) channel, dN/dt, as a function of t is well represented by the equation

$$dN/dt = C\, e^{-t/\tau}$$

where τ has the value 1.5 msec. The initial form of the dN/dt distribution can be seen more clearly in Fig. 4.2, a full logarithmic plot of the distribution for values of t up to 2 msec. Over the range 0.4 msec to about 1.4 msec a rather good fit to the distribution can be obtained with a power law decay

$$dN/dt = Ct^{-b}$$

where in this case $b \approx 3.2$. The data before 0.4 msec decays considerably more rapidly; however, at these flight times a portion of the distribution consists of non-ground state electrons whose

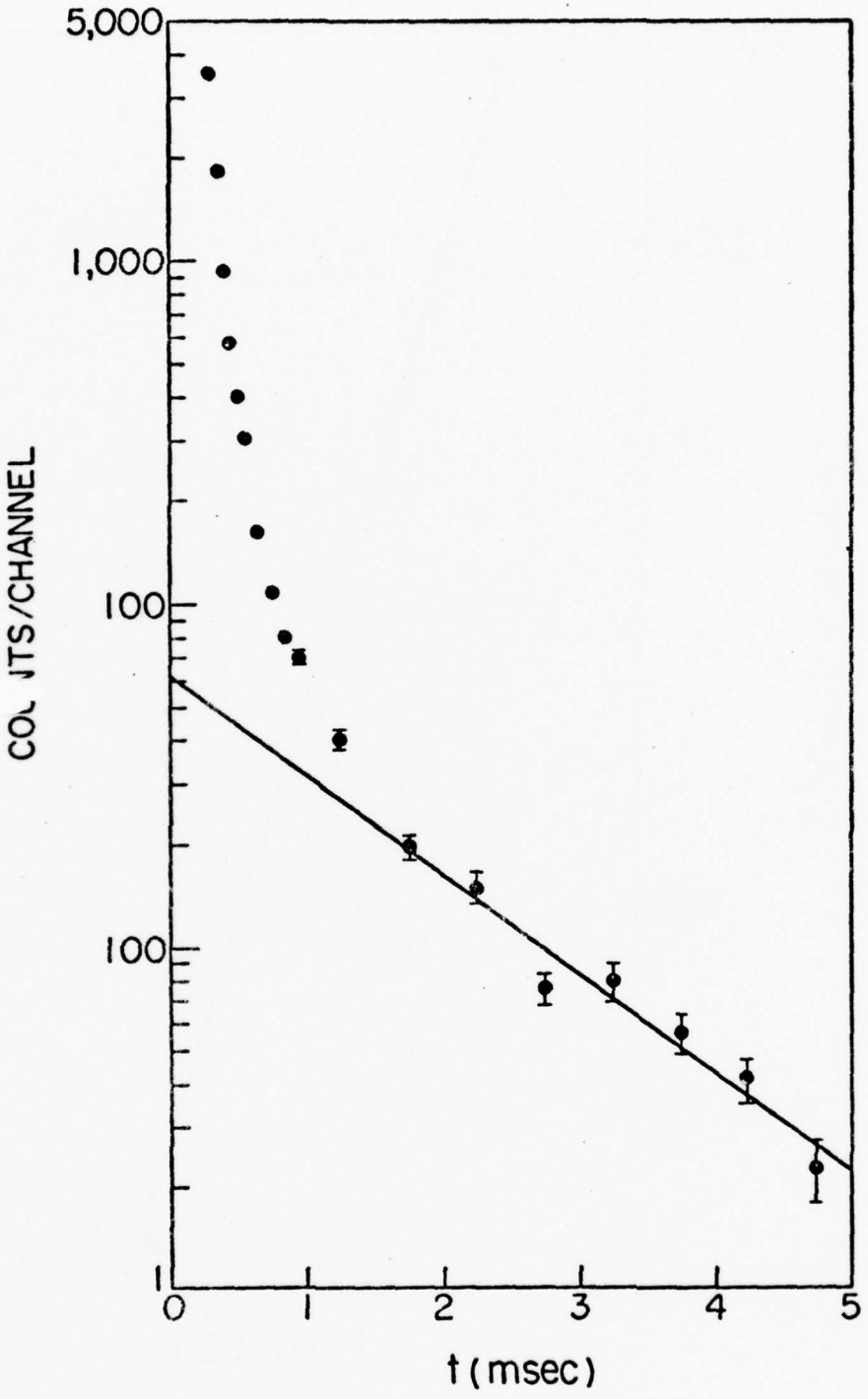


Fig. 4.1. A representative room temperature time-of-flight spectrum taken with no applied force in the tube. The line is a least squares fit to the data after 1.5 msec; it represents a decaying exponential with time constant 1.5 msec.

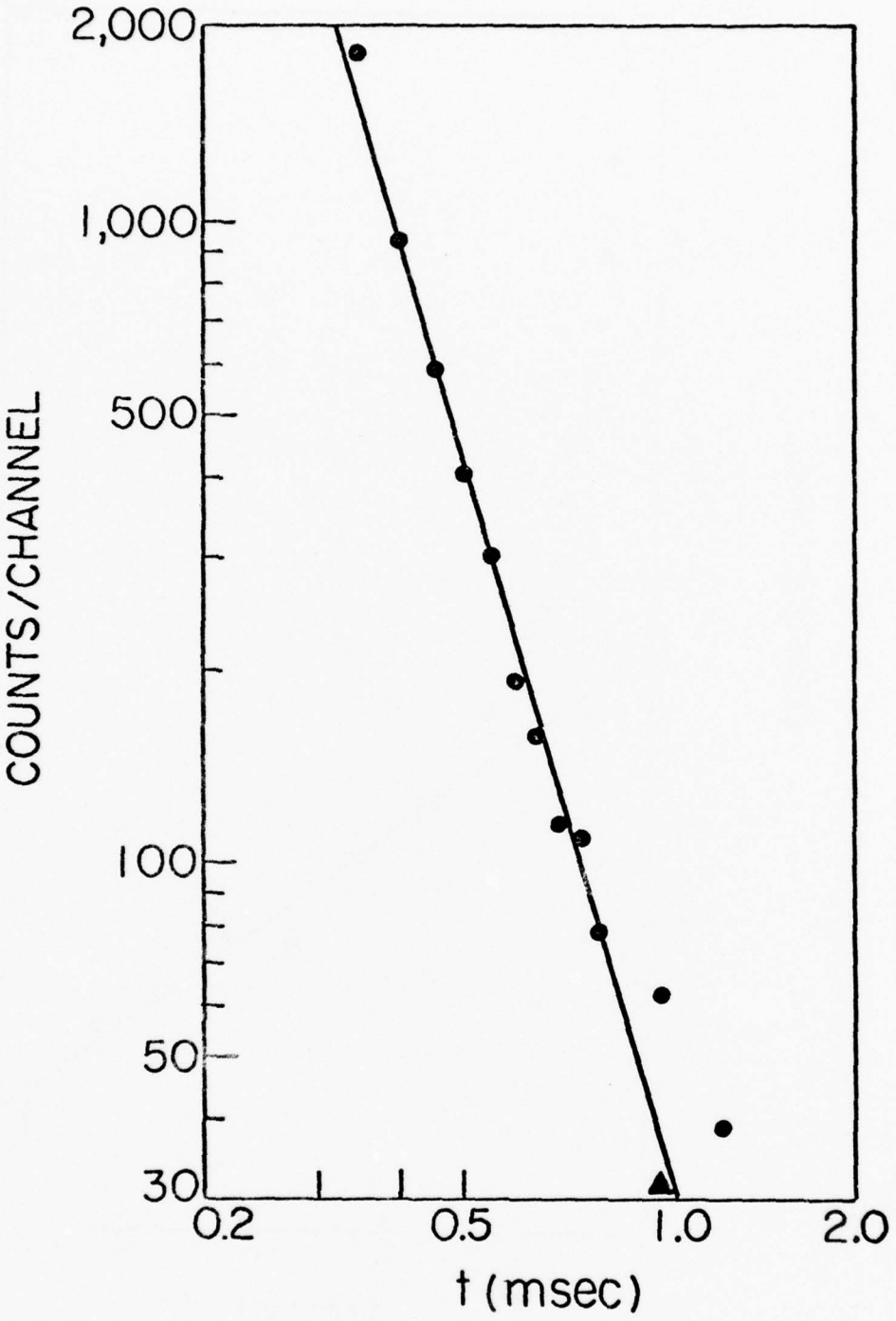


Fig. 4.2. A full logarithmic plot of the initial portion of the TOF distribution of Fig. 4.1. The triangle indicates the point obtained by subtracting from the t=1.0 msec point an amount equal to the value of the exponential curve of Fig. 4.1 at 1.0 msec. The line is a least squares fit to the data between 0.35 and 1.0 msec; it represents a $t^{-3.2}$ decay.

distribution is determined primarily by the magnetic state selection process.

As we saw in Sec. 3.2 a t^{-3} decay of dN/dt is expected on the basis of the velocity spectrum of electrons emitted from the cathode, so it appears that within statistical limits the electrons arriving before 1.5 msec represent direct emission from the cathode. We also discussed in Sec. 4.1 the likelihood that electrons emitted from potential traps along the beam path would appear in the distribution rather suddenly at time t_t and would then decay either as a single exponential or as a sum of exponentials with differing time constants. It thus appears that the electrons arriving after 1.5 msec in Fig. 4.1 are emitted from potential traps, although some of the added flux here may result from rethermalization.

The most important aspect of the room temperature data is illustrated in Fig. 4.3, which shows the data of Fig. 4.1 plotted along with two additional sets of data from the same run which show the TOF spectra obtained with applied electric fields present in the drift tube. It is clear from this graph that the number of electrons arriving after 1.5 msec is progressively decreased as the applied electric field is increased. If the portion of the distribution after 1.5 msec corresponded to direct cathode emission, we would expect to see cutoff effects in the applied field runs, with the cutoff time shifting with the value of the applied field. The observed dependence of the distribution on the value of applied field is much more consistent with the idea that most of the electrons arriving after 1.5 msec result from delayed emission from potential traps. The crucial point is that an electric field in the drift

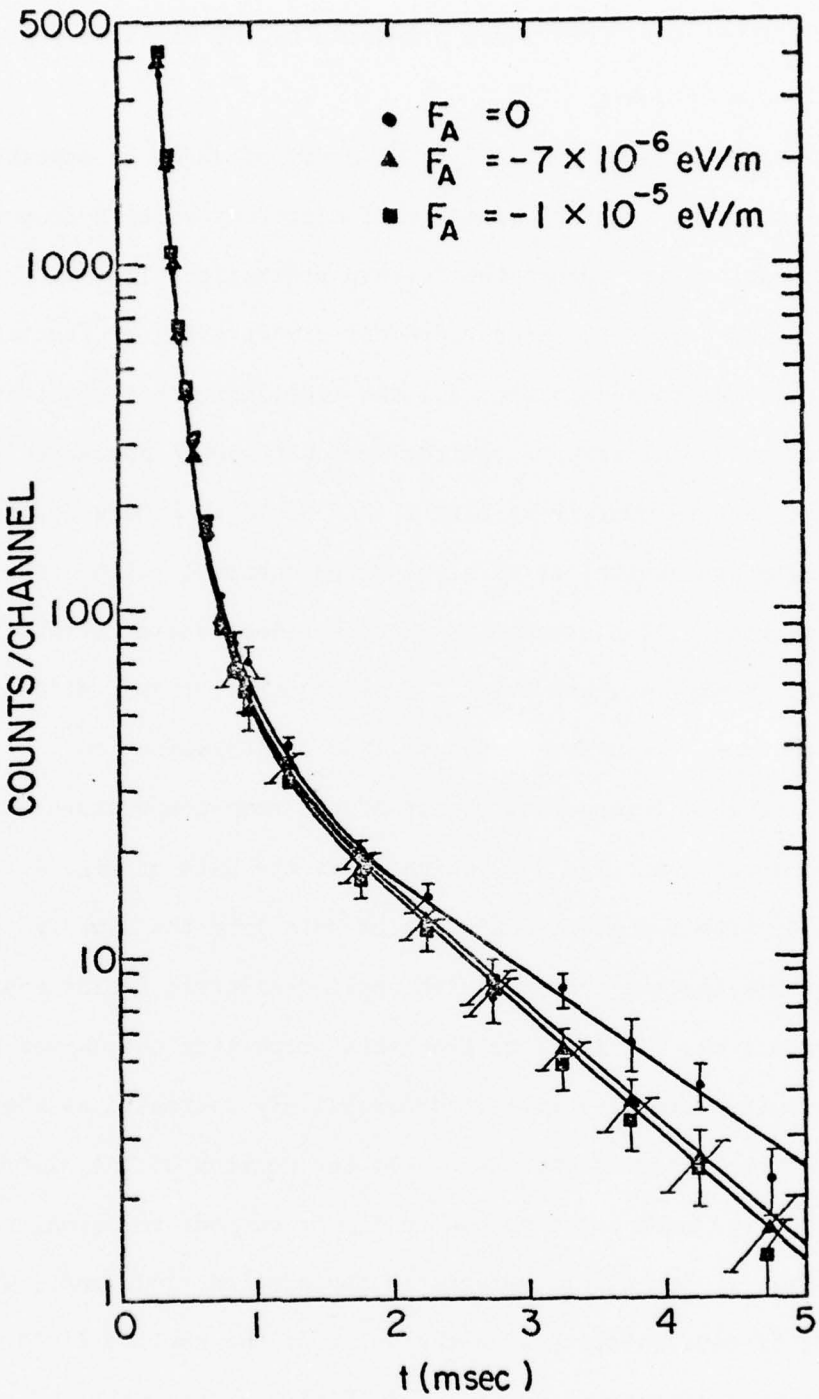


Fig. 4.3. A representative set of room temperature TOF spectra showing the effect of applied forces. The straight line through the $F_a = 0$ points is the same fit as in Fig. 4.1. The two other straight lines are visual best fits. The curve drawn through the initial portion of the distribution is essentially the same fit as that in Fig. 4.2.

tube can prevent the low-energy component of the delayed electron distribution from reaching the detector. The exact energy range of the delayed electrons which will be turned back by an applied field depends on whether most of the trapping occurs below or near the lower end of the drift tube or at some higher position along the tube. However, the experimentally observed fact that the number of electrons arriving after 1.5 msec is reduced by the application of an electric field permits a rough determination of the ambient electric field present in the drift tube at room temperature, as we shall show a bit later.

The effectiveness of applied fields in modifying a TOF spectrum obtained over 10^6 or so cathode pulse rests on another as yet unstated assumption, which is that the extent to which various traps are populated after each cathode pulse does not depend on the state of the traps before the cathode pulse. In other words, each cathode pulse and associated counting interval constitutes an independent experiment which is not affected by the history of previous such experiments. This assumption is reasonable since a large number of relatively high energy electrons sweep through the beam path immediately after each cathode pulse. As this space charge wave approaches a trap it tends to empty the trap. Although the trap may well be re-occupied because of three-body electron collisions or perhaps electron-gas atom collisions which occur as the space charge wave passes by the trap, any memory of the previous occupation of the trap will certainly be lost.

It seems clear that an applied field will remove a significant number of slow electrons from the distribution that reaches the

detector only if that field constitutes an appreciable fraction of any ambient field present in the drift tube (we discussed this point at some length in Sec. 3.2). If we assume that the energy distribution of electrons emitted from traps is essentially linear in energy up to some maximum value of energy we would expect that a given fractional change in the energy required for an electron to reach the detector would produce the same fractional change in the number of trap-originating electrons arriving at the detector. We can thus gain information about the level of ambient fields in the tube by plotting the percentage effect on the distribution produced by an applied field against the value of the applied field. The zero-effect intercept of this plot should indicate the ambient field present.

When it was seen that cutoff effects were not appearing in the room temperature data (because the slow counts are apparently almost entirely provided by trap-originating electrons) it was decided to analyze the room temperature data by determining the percentage reduction in slow electron flux produced by various values of applied field. In this method "slow" electrons were defined as those arriving after a time corresponding to the cutoff expected for the smallest of the three values of applied force used in a run. The four spectra accumulated in a given run (three with applied force and one with no applied force) were normalized by requiring that they all have the same number of counts in their first three channels. Then the number of slow electrons in each of the four spectra was determined and the ratio of the number of slow electrons in the applied-force spectrum to the number in the no-applied-force spectrum was calculated

for each value of applied force. A summary of results obtained with this analysis technique is presented in Fig. 4.4. We have plotted the slow electron ratio as described above against the applied force values plotted on a logarithmic scale. An applied force in the upward direction is taken to be positive.

We see from the illustration that downward applied forces produce the expected effect — the slow electron ratio is progressively decreased as the applied force is increased. Looking at the upward applied forces, we see that the slow electron ratio suddenly begins to increase rapidly when the applied force reaches a value of about 10^{-5} eV/m. The implication here is that there is an effective downward ambient force in the tube of roughly the same magnitude (that is, an ambient force of -5×10^{-5} eV/m) and thus when the magnitude of the upward applied force approaches this value the net force in the tube is significantly reduced, causing an increase in the slow electron ratio. Unfortunately, the work with upward applied forces is complicated to some extent by the fact that an applied field which accelerates electrons along the tube causes an enhancement of emission from potential traps. However, as we shall see shortly, there is good reason to believe that the value we have just obtained represents a reasonable order-of-magnitude estimate of the ambient field in the tube at room temperature. We also see from Fig. 4.4 that a downward applied force of $\sim 10^{-6}$ eV/m just begins to have an effect on the distribution. Any lattice distortion or patch effect potential fluctuations in the drift tube must be within roughly an order of magnitude of this value. We can get a better idea of the ambient potential variations in the tube from Fig. 4.5, which is a

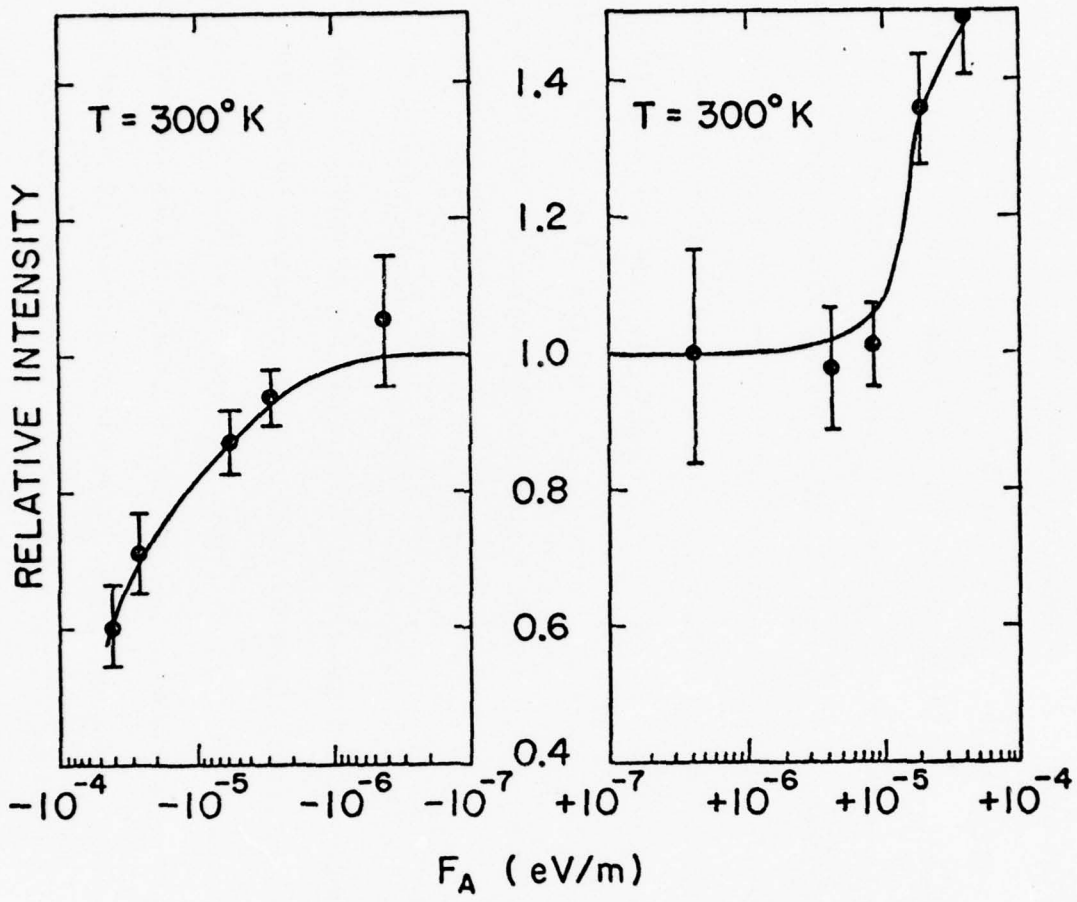


Fig. 4.4. A summary of results obtained at room temperature. The y-axis is the ratio of the slow electron flux with a gived applied force to the flux obtained with no applied force. The curve shown is only a guide for the eye and does not represent a theoretical fit to the data.

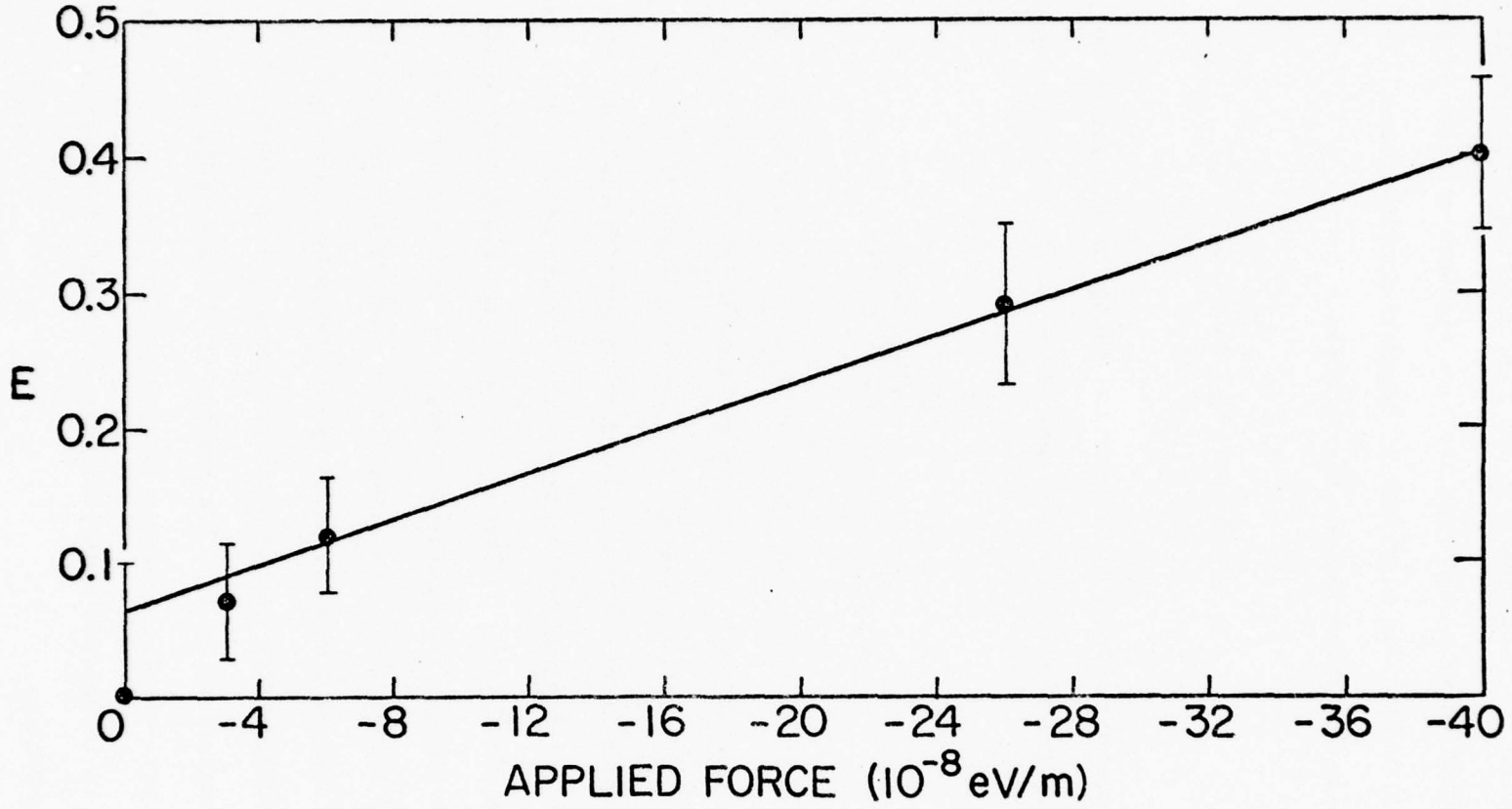


Fig. 4.5. A linear plot of the data of Fig. 4.4 over the range -(0-40) x 10^{-6} eV/m. The y-axis E is equal to 1-R where R is the y-axis of Fig. 4.4. The straight line is a visual best fit to the data.

linear plot of the reduction E in the slow electron ratio (equal to the difference between unity and the slow electron relative intensity of Fig. 4.4) versus the magnitude of downward applied force. The straight line fit shown follows the equation

$$E = 0.065 + \frac{F_a}{11.6 \times 10^{-5}\ \text{eV/m}} \quad .$$

We argued previously that the fractional change in E ought to be equal to the fractional change in applied force F_a. In the present case we have

$$\frac{\Delta E}{E} = \frac{\Delta F_a}{(F_a + 7.5 \times 10^{-6}\ \text{eV/m})}$$

so that the fractional changes will be equal if we assume that ambient potential variations are present in the tube which produce an effect on the slow electrons equivalent to a downward force of 7.5×10^{-6} eV/m. (Note that this is in rather good agreement with the ambient force value which we obtained by looking at the effects of different values of upward applied force.) These potential variations could arise either from the lattice distortion effect or from patch effect potential fluctuations. The direction is correct for the lattice distortion field but the magnitude is too large by one to two orders of magnitude according to the estimates presented in Chapter 2. Potential variations of 10^{-5} V along the drift tube would be quite consistent with the patch effect estimates also presented in Chapter 2, leading us to believe that it is the patch effect we are seeing at room temperature.

Before leaving our discussion of the room temperature results we should mention the effectiveness of the magnetic state separation at room temperature. All of the data presented in this section was taken with a cathode magnetic field of ~ 70 G. This value of magnetic field caused all non-ground state electrons to arrive at the detector within 1.8 msec of the cathode pulse (with the possible exception of non-ground-state electrons which were caught in potential traps as a result of collisions). The shortest value of flight time which was used in the room temperature analysis was 1.5 msec, so the value of cathode magnetic field we were able to use was just barely adequate to provide the magnetic state separation necessary for the data analysis procedure to be valid. It is possible that some of the noise effects seen in the room temperature work were caused by electrons in excited cyclotron states which were emitted from traps and then interacted with magnetic field gradients along the flight path.

4.3 77°K Data

A relatively small amount of data was taken at 77°K because of premature failure of the tunnel cathode. The effects of applied electric fields turned out to be very similar to the effects observed at room temperature even though the actual TOF distributions obtained at 77°K differed considerably from their 300°K counterparts. Figure 4.6 shows some of the best (in terms of noise level) data obtained at 77°K. Let us first examine the data taken with no applied fields. After approximately 1.0 msec the data can be fitted by a decaying exponential with time constant 5.3 msec. This represents quite a

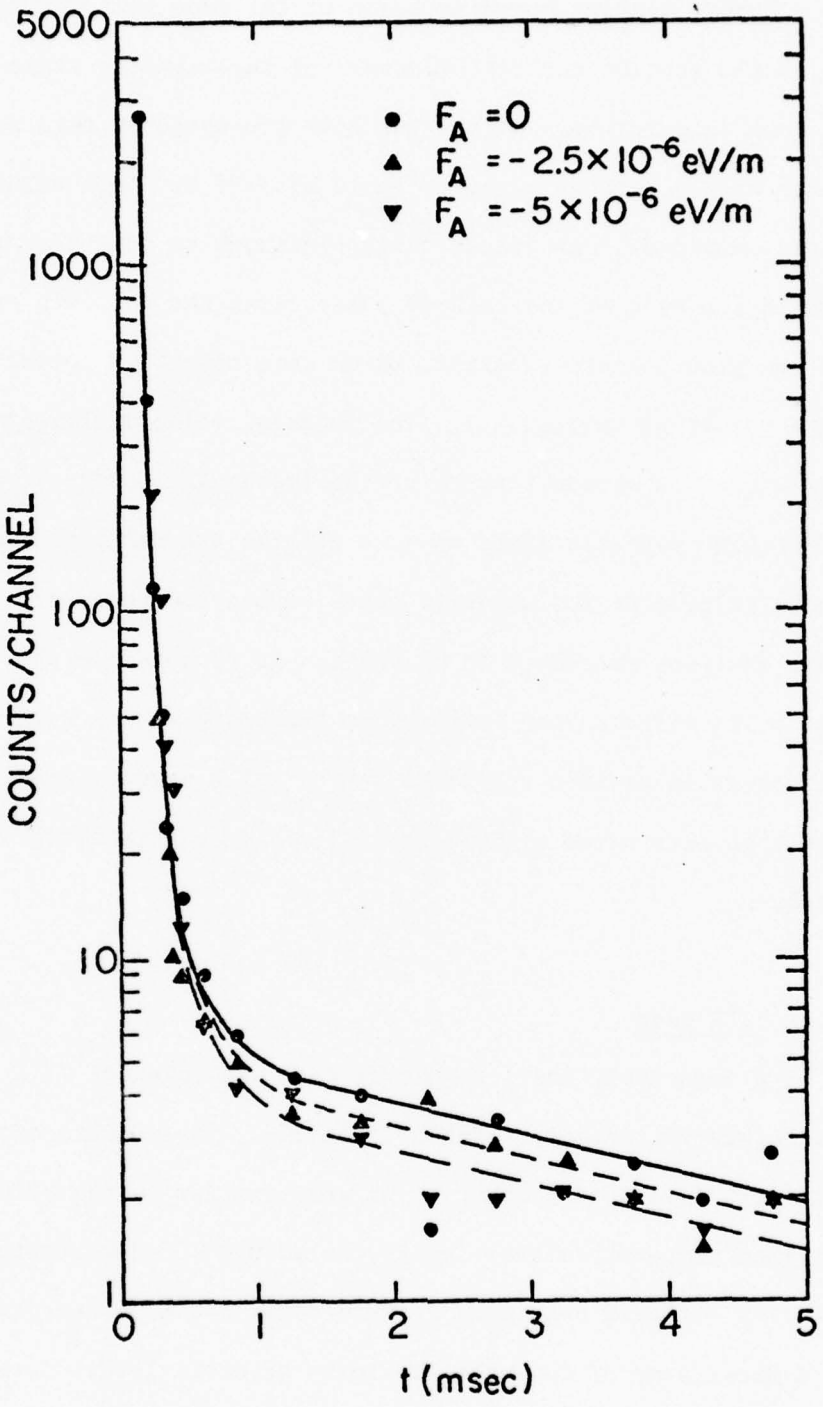


Fig. 4.6. A relatively low-noise set of 77°K TOF spectra taken with three different applied force values, The straight lines shown are visual best fits to the data; the initial curve is only a guide for the eye.

slower decay than the 1.5 msec time constant seen after 1.5 msec in the room temperature data. The early behavior of the distribution can be seen more clearly in Fig. 4.7, a full logarithmic plot of the zero-applied-force data of Fig. 4.6. The early distribution seems to follow a t^{-5} curve, in contrast to the $t^{-3.2}$ dependence seen at room temperature. A portion of this difference may be explained by the higher value of cathode magnetic field used at 77°K (140 G as compared to 70 G at 300°K), which causes all non-ground-state electrons to arrive within about 1.0 msec of the cathode pulse.

The main item of interest in the 77°K data is the smallest value of applied force which has a significant effect on the distribution. A slow electron ratio analysis as described in the preceding section was applied to the data of Fig. 4.6. Once again a flight time value of 1.5 msec was taken as the beginning of the slow electrons. (An applied force of 2.5×10^{-6} eV/m has a cutoff time of 2.1 msec, while 5×10^{-6} eV/m gives 1.5 msec.) The -5×10^{-6} eV/m force produced a slow electron ratio of 0.82 ± 0.11, while the -2.5×10^{-6} eV/m applied force gave a ratio of 1.00 ± 0.11. All smaller values of applied force studied in other 77°K runs gave a ratio which was 1.0 within statistical limits. Thus the limit of resolution for applied forces at 77°K seems to be about 5×10^{-6} eV/m, quite close to the room temperature resolution limit of about 4×10^{-6} eV/m (as determined from Fig. 4.5) and the room temperature effective ambient electric field of 7.5×10^{-6} V/m.

It thus seems that the ambient potential variations in the drift tube at 77°K are essentially the same as those found at 300°K.

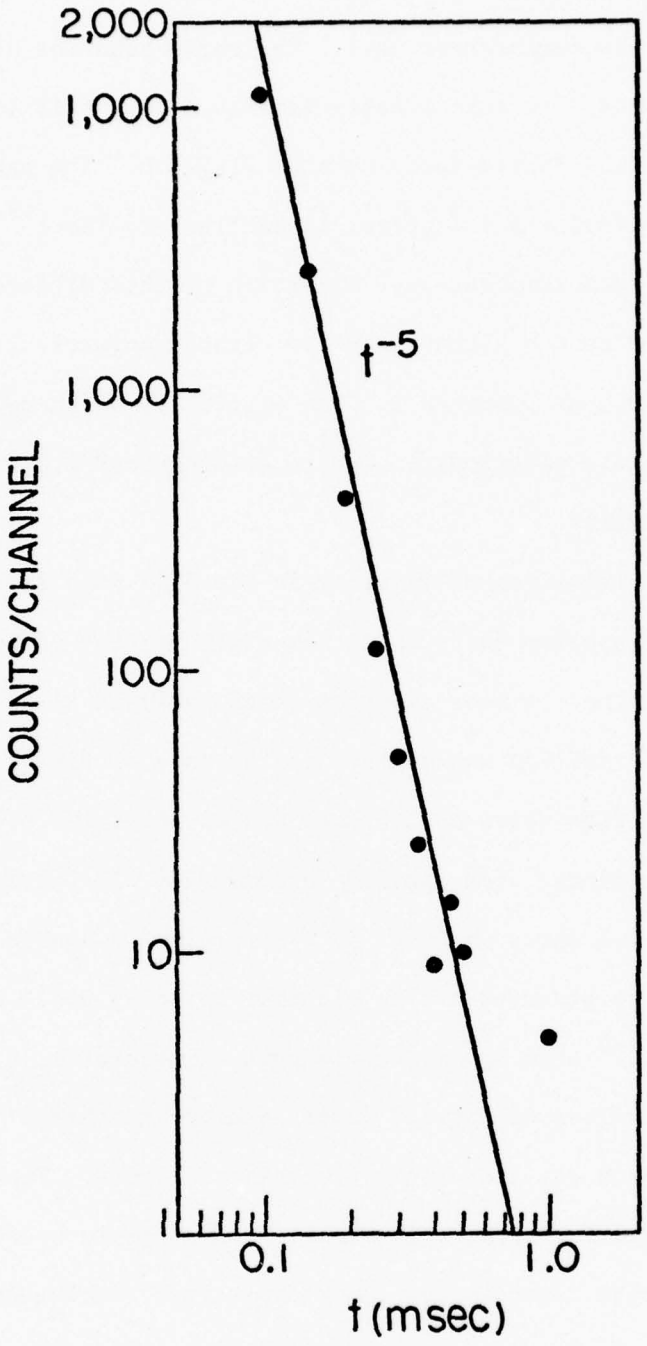


Fig. 4.7. A full logarithmic plot of the initial portion of the zero-applied-force distribution of Fig. 4.6. The straight line is a visual best fit to the data; it represents a t^{-5} decay.

4.4 First LHe Run

The primary purpose of our first LHe run was to verify that the apparatus was still capable of resolving applied electric fields as small as those used by Witteborn and Fairbank. If 10^{-11} V/m fields could be resolved at 4.2°K in the same apparatus which had exhibited apparent drift tube potential variations of $\sim 5 \times 10^{-6}$ V/m at 300°K and 77°K we would have evidence for a temperature dependence in the ambient electric field in the drift tube.

The various zero-applied force spectra taken during this run did not show a uniform distribution. The most common form of the TOF distribution is shown in Fig. 4.8. This distribution has an initial decay which upon closer examination proves to go as $t^{-1.6}$ out to about 30 msec. We should point out that because we in general study much smaller applied forces at 4.2°K than at room temperature or 77°K, the time of flight values discussed in this and the next section will extend to much larger values than those discussed in the previous two sections. The $t^{-1.6}$ initial decay is the most common; however, $t^{-1.3}$ and $t^{-2.9}$ forms of decay each occurred in several runs (in all cases the initial power law behavior held out at $\sim$ 30 msec). Only the $t^{-2.9}$ form is in agreement with the 300°K and 77°K results and with expectations based on the velocity distribution of the cathode. It appears that we are getting a significant amount of rethermalization of the electron beam; i.e., the 3000°K electron distribution emerging from the cathode is "cooling" before it enters the drift tube. Possible mechanisms for this are multi-electron collisions and collisions between emitted electrons and residual gas molecules. The former mechanism is expected to be

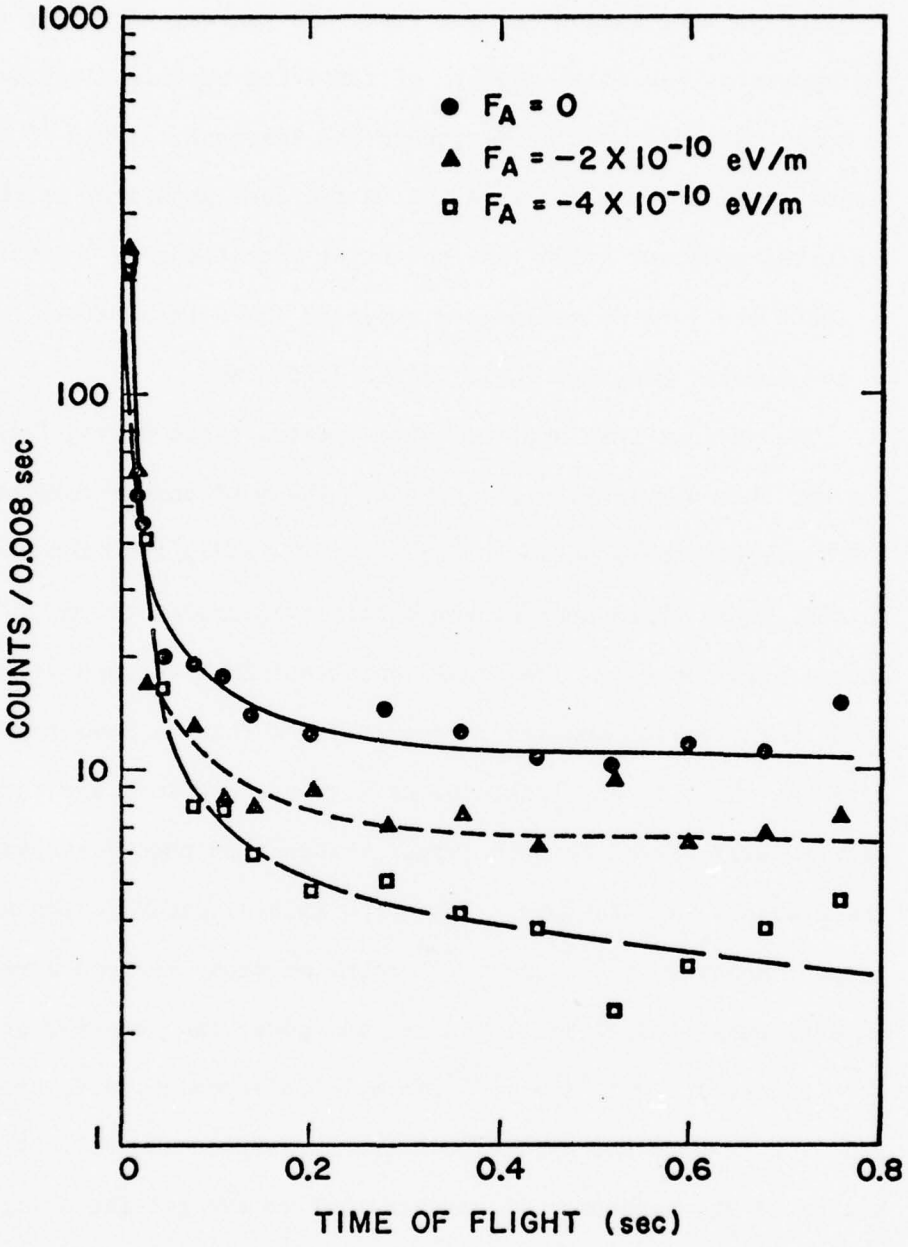


Fig. 4.8. A typical set of 4.2°K TOF spectra taken with three different applied force values. The straight line fits after 0.2 sec were obtained visually; they represent exponential decays with time constants of 250-300 msec.

dominant unless the residual gas pressure is unusually high. One would expect a considerable number of delayed, trap-originating electrons in the distribution if significant rethermalization is taking place; as we shall see below, such appears to be the case.

The distribution between 30 msec and 200 msec in Fig. 4.8 can be well represented by a decaying exponential with a long time constant ($\sim$300 msec). All the distributions studied showed this exponential decay between 30 msec and $\sim$200 msec with time constants ranging from 300 msec down to $\sim$40 msec. We assume that these electrons have been emitted from potential traps; if so, the long exponential time constants indicate that de-trapping events occur much less frequently at 4.2°K than at 300°K or 77°K. This lends support to the hypothesis that some electrons are emitted from traps via collisions with residual gas molecules, since the residual gas pressures at 4.2°K are one to two orders of magnitude lower than those observed at 300°K and 77°K.

Since we expect the trap-originating electrons to respond to applied forces, we once again use the slow electron ratio analysis. In this case the best results were obtained by ratioing the number of counts which arrived after the theoretical cutoff time when a force was applied to the number of electrons which arrived after the cutoff with no force applied. Normalization was employed to account for large cathode emission variations within a run.

The results of the slow electron ratio analysis are summarized in Fig. 4.9. We note from the figure that (1) the effect appears to by symmetric in the direction of the applied force and (2) a force

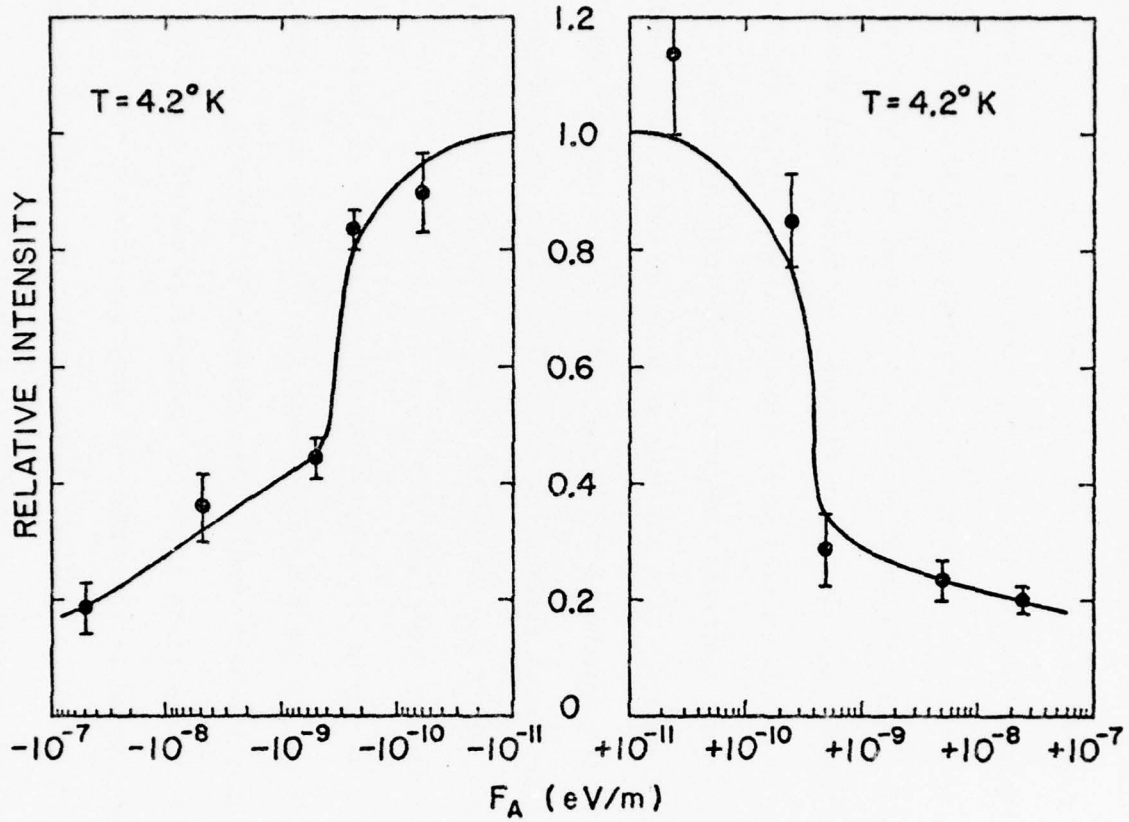


Fig. 4.9. A summary of results obtained in the first 4.2°K run. The y-axis is the ratio of the slow electron flux with a given applied force to the flux with no applied force present. The curve shown is only a guide to the eye and does not represent a theoretical fit to the data.

as small as 2×10^{-10} eV/m has a statistically significant effect on the distribution.

Because data from this LHe run was accumulated over such a large range of applied forces (three orders of magnitude), which in turn required the use of rather different time periods for the TOF scan, it is not practical to make a linear graph of applied force values versus the corresponding reductions in slow electron ratio as we did in Fig. 4.5. Thus we do not have as direct a means of evaluating the ambient potential variations in the drift tube as we did at room temperature. Had more running time been available, we would have taken measurements at much more closely spaced intervals. However, our experience at room temperature indicates that the minimum applied force which produces a statistically significant reduction in the slow electron ratio will be within a factor of two or three of the value of the maximum ambient potential fluctuations in the tube. As we have already noted, this minimum observable applied force is about 2×10^{-10} eV/m, indicating that the ambient potential fluctuations are below 5×10^{-10} V/m. We say "below" rather than "approximately equal to" for two reasons: (1) a moderate reduction in the error assigned to the -5×10^{-11} eV/m point would make it the minimum applied force which produces a significant effect and (2) we rely on the results of the Witteborn-Fairbank experiment, which indicated that the only ambient forces larger than 10^{-11} eV/m acting on an electron in the tube were the force of gravity and a force due to the Schiff-Barnhill electric field of -5.6×10^{-11} V/m which just cancels the force of gravity.

The fact that the effect of an applied force on the slow electron ratio is symmetric in the direction of the applied force is further evidence that the effective ambient force in the tube is smaller than the smallest value of applied force which significantly affects the distribution. This situation is in contrast to the highly asymmetric effect of applied forces at room temperature (see Fig. 4.4) caused by the presence of a relatively large ambient force in the tube at that temperature. (Note that although the curve in Fig. 4.9 is symmetric the data actually shows a slight tendency for the slow electron ratio to be largest when the applied force is about $+ 3 \times 10^{-11}$ eV/m. However, the uncertainty in the relevant data point is large enough to make the point consistent with the indicated symmetric curve.)

Since the objective of the first LHe run was to verify our ability to observe small applied forces at 4.2°K, we felt that the run was successful when $\sim 10^{-10}$ eV/m forces were resolved.

4.5 Heated Drift Tube Experiments

The data presented in Secs. 4.2, 4.3, and 4.4, especially when combined with the results of the WF experiment, gave strong evidence that the ambient potential variations along the axis of the drift tube were much smaller at 4.2°K than at 77°K or 300°K. However, the most convincing evidence for a temperature-dependent shielding effect in the drift tube is presented in this section, where we describe data taken at temperatures of 4.2°K, 4.3°K, 4.4°K, 6°K, 9°K, and 11°K. Before looking at the data, we will examine the general nature of the distributions and the method of

analysis employed in this series of experiments. We will illustrate these discussions with 4.2°K data taken from the heated drift tube series of runs; however, the comments which we will make apply equally well to the data taken at the higher temperature values.

4.5.1 Nature of the Zero-Applied-Force TOF Distribution

The 4.2°K zero-applied-force TOF spectra obtained in this set of runs fit quite well a distribution characterized by an initial t^{-4} decay out to $\sim$10 ms followed by a decaying exponential with a time constant in the range 20-40 msec, as shown in Figs. 4.10 and 4.11. The initial t^{-4} decay was rather puzzling at first since a t^{-3} decay was the most rapid seen in the earlier 4.2°K work. However, there is one important difference between the conditions under which this data was taken and the conditions of the previous LHe run. Because of a small crack which developed in one of the vacuum feedthroughs at the beginning of this run, most of the data was accumulated with residual gas pressures of $\sim 10^{-9}$ Torr. We can see the effects of such a pressure by looking at Fig. 4.12, which shows a series of TOF spectra taken over a range of residual gas pressures. We see that increasing the residual gas pressure from 8×10^{-10} Torr to 2.5×10^{-9} Torr results in a shift of the initial form of the distribution from $t^{-2.4}$ to t^{-5}. The t^{-4} dependence seen in most of our data from this set of runs would thus seem to indicate a residual gas pressure of about 2×10^{-9} Torr. We should note that the residual pressure is assumed to be almost completely due to He, since the feedthrough in question was located in the He vapor space of the dewar and since the ion pump pumps He rather inefficiently.

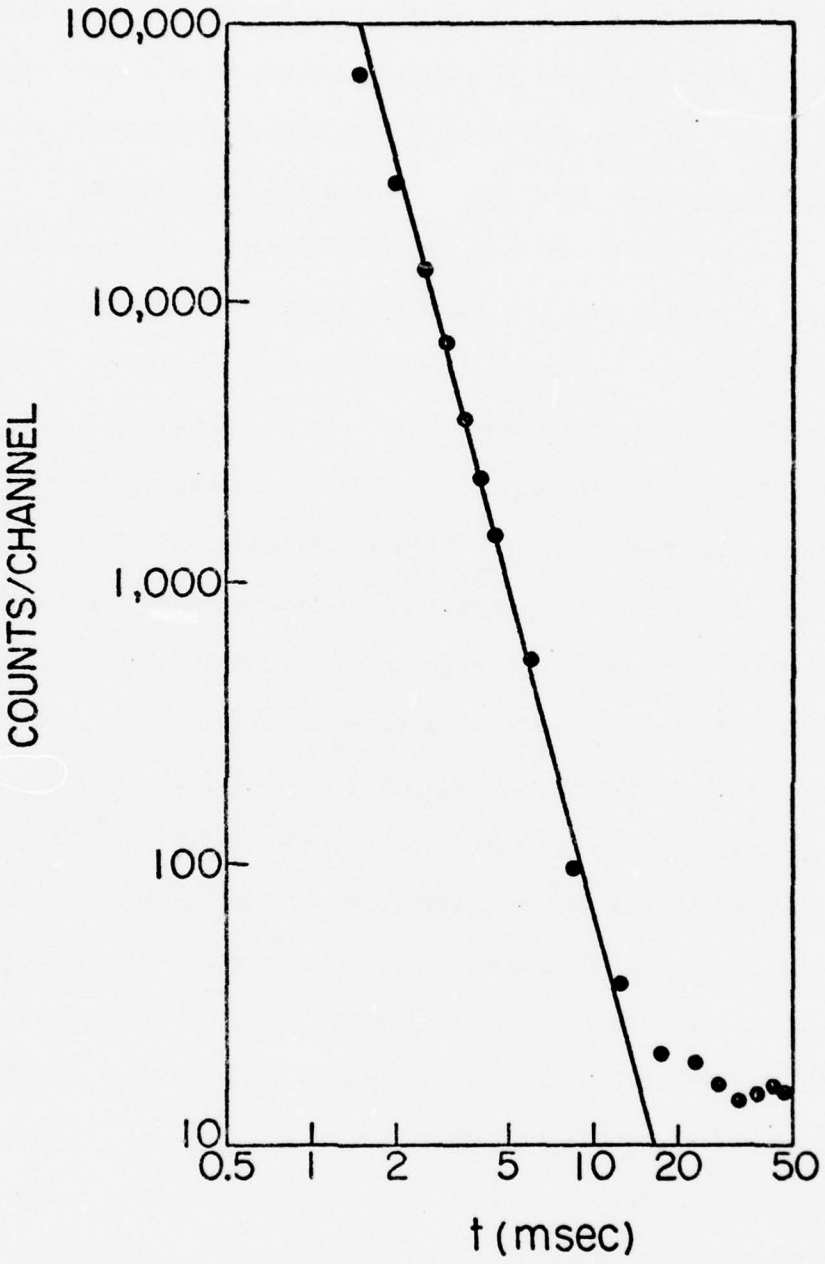


Fig. 4.10. A full logarithmic plot of the initial portion of a typical TOF distribution obtained in the heated drift tube experiments. The tube was at 4.2°K and the applied force was zero. The line is a least squares fit to the data points up to 12 msec; it represents a t^{-4} decay.

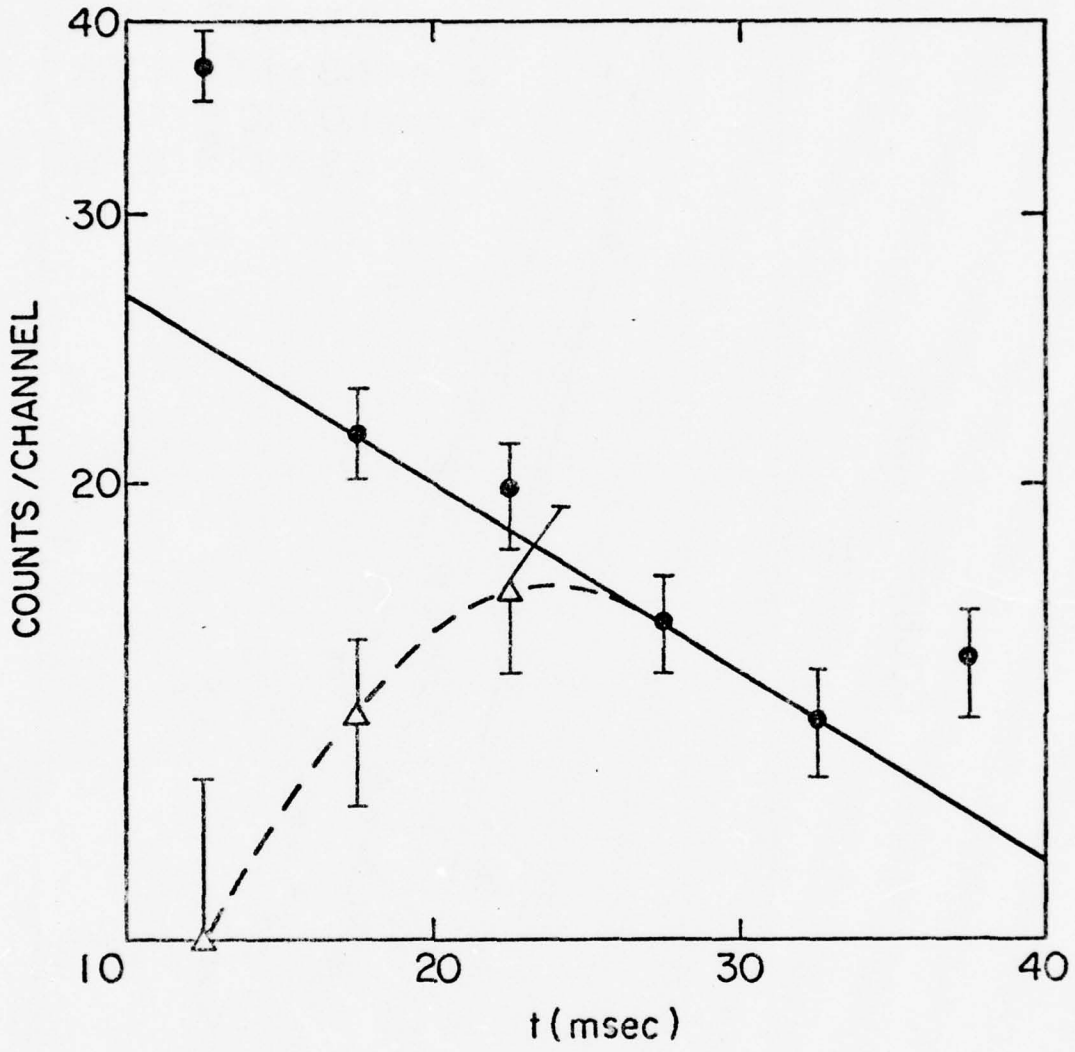


Fig. 4.11. The latter portion of the TOF distribution of Fig. 4.10. The points shown with dots are the raw data points while the points indicated with triangles show the result of subtracting from the raw data points an amount equal to the value of the curve of Fig. 4.10 at the appropriate flight time values. The straight line is a visual best fit; it represents a decaying exponential with a time constant of 35 msec. The curved line is only a guide to the eye.

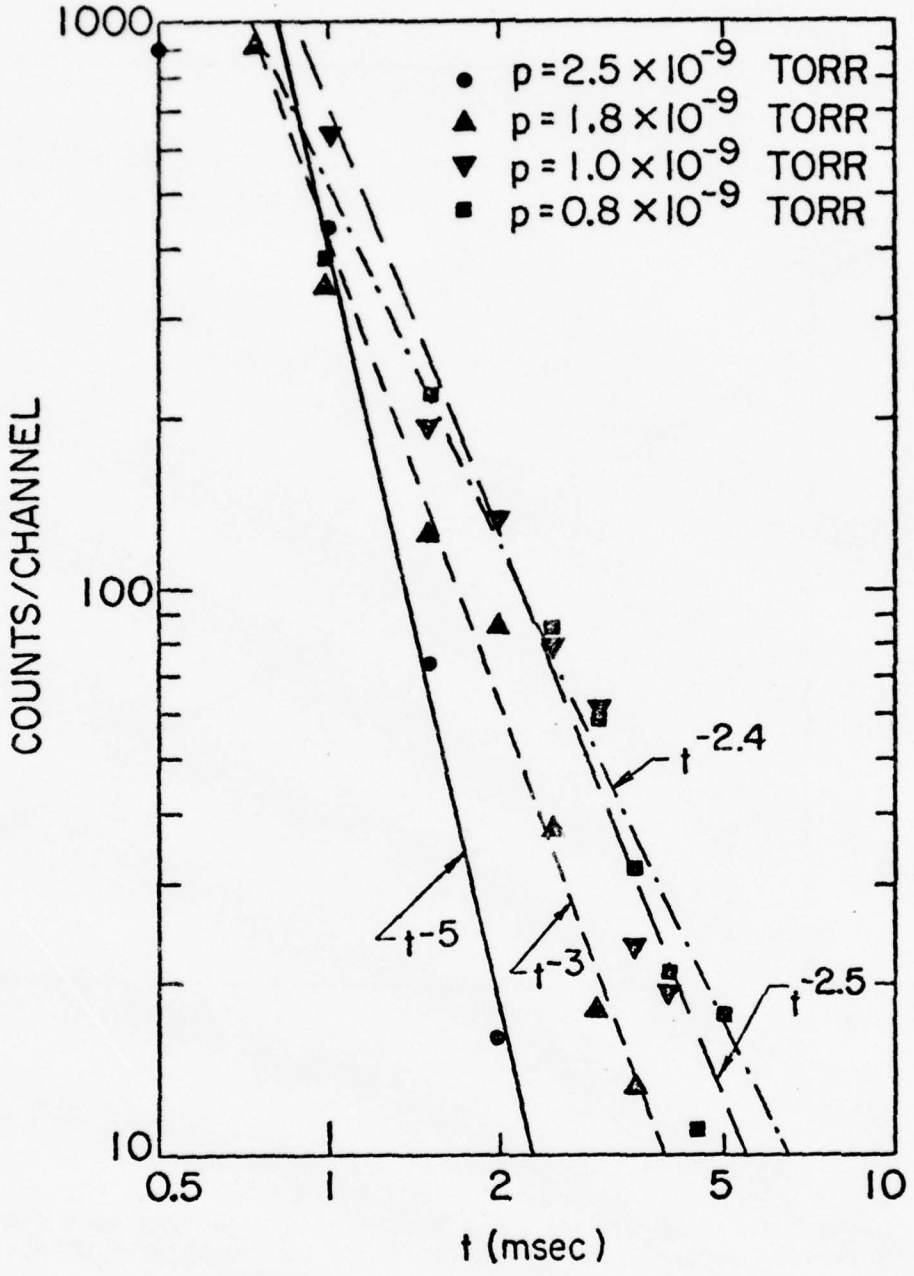


Fig. 4.12. A set of zero-applied-force 4.2°K TOF spectra taken with four different values of residual gas pressure in the vacuum chamber. The lines are visual best fits.

This value for the residual gas pressure agrees well with measurements based on the amount of ionization current drawn by the pump.

The rather short (as compared with the data of Sec. 4.4) time constant seen in the exponential decay portion of the distribution is also consistent with higher than usual background pressures if we assume that that portion of the distribution contains mainly trap-originating electrons since de-trapping collisions occur more frequently with higher values of gas density.

Although the t^{-4} decay behavior provides a very good fit to the initial 10 msec of the TOF distribution, it does not provide a complete description of the TOF distribution of electrons which result from direct emission from the cathode. This became evident during the analysis of the heated drift tube data when it was observed that direct emission electrons were present out to at least 25 msec, where they appeared to account for 20-25% of the total number of electrons reaching the detector.

A change in the form of the distribution from t^{-4} to a somewhat less rapid rate of decay at a flight time of 10 msec is reasonable on several counts. If we in fact have an appreciable rate for electron-Helium atom collisions, some fraction of the electrons removed from the early portion of the distribution by such collisions should reappear in a later portion of the distribution. Also, we should note that an electron which arrives at 10 msec has an average kinetic energy in the tube of $\frac{m}{2}(100 \text{ cm}/0.1 \text{ sec})^2 \cong 2.8 \times 10^{-8}$ eV, which is essentially the same as the 3×10^{-8} eV cyclotron level spacing of electrons in the field of our guide magnet. Electrons which have less than this energy (and which thus have longer flight

times) have less tendency to become caught in magnetic potential traps since they can no longer be raised from the cyclotron ground state to the first excited state by a collision process which converts some of their linear kinetic energy to cyclotron energy (their linear KE is now less than the quantum level spacing). Ground state electrons are normally caught in magnetic potential traps by just such a process. In any event, it does seem to be the case that a significant number of direct emission electrons with flight times of 25 msec are present in the zero-applied-force distribution.

The points indicated by triangles and the dashed curve in Fig. 4.11 show the result of subtracting the t^{-4} curve which fits the first 10 msec of the distribution from the exponential fit used after the first 10 msec. We see that the counts which are not part of the initial t^{-4} distribution (*resulting partly from trap* emission and partly from rethermalization by multi-electron collisions, e^--He collisions, or other mechanisms) begin arriving at $\approx$ 10 msec. As it turns out, the manner in which applied forces affect this second portion of the distribution indicates that the trap-originating electrons have energies of 10^{-7} eV or less. The TOF for a 10^{-7} eV electron would be only 5.5 msec; we assume that the 4.5 msec difference between this value and the 10 msec time at which we seem to begin seeing the trap-originating electrons is the time needed for a trap to become populated and begin emitting. We will make the assumption that the electrons in the second portion of the distribution which result from trap emission (apparently 75% or so of the second portion) are relatively monoenergetic (at $\sim 10^{-7}$ eV)

and that the structure of the second portion of the TOF distribution is produced by the time spread of the emission from traps. Under this assumption all of the trap-originating electrons will be delayed by the same amount when a retarding force is applied in the tube and the entire trap-originating distribution will shift along the time-of-flight axis. We will see in Sec. 4.5.3 that such behavior is consistent with the observed effects of applied retarding forces. The monoenergetic assumption implies that one particular type of trap and/or de-trapping mechanism is predominant. While such a situation seems quite feasible, we have no particular reason to believe that that situation exists. It is quite possible that several different energy distributions of trap-originating electrons could be consistent with the observed effects of applied forces. Since the question of the detailed energy distribution of the trap-originating electrons need not be answered in order to determine the ambient potential variations in the tube, we will not pursue it further.

4.5.2 Analysis of the Heated Drift Tube Data

The data taken at each value of drift tube temperature (including 4.2°K) consists of 4 TOF spectra, corresponding to applied axial currents in the drift tube walls of 0, 0.02 A, 0.05 A, and 0.1 A. If we use our measured value of drift tube resistance at 4.2°K, these currents translate to applied forces of 0, -3×10^{-8} eV/m, -7.5×10^{-8} eV/m, and -1.5×10^{-7} eV/m. A few data points involving positive (accelerating) applied forces were also taken.

In this series of experiments we made a point of taking several runs under identical conditions using this same set of applied force

values in order to improve the counting statistics. As it turned out, the amount of data acquired for each applied force was sufficient to permit a much more precise and quantitative evaluation of the fields present in the drift tube than was possible in the previous work. In particular, rather than just finding the minimum applied force which significantly affects the distribution as we did in Secs. 4.2, 4.3, and 4.4, we are able to determine directly the apparent ambient electric field in the tube.

It is fortunate that the revised technique was available for the analysis of the heated drift tube data, since the slow electron ratio technique used in the previous sections is really not very useful with this data. In the room temperature and LN_2 work, relatively large forces were studied; consequently, short (5 msec) TOF sweep times were used and therefore direct emission electrons were present all the way to the end of the TOF sweep. In the first LHe run the decay of the direct emission electrons in the initial portion of the distribution was only $t^{-1.5}$ or so; thus, direct emission was again appreciable all the way to the end of the TOF sweep for the sweep times used. Therefore an applied force should reduce the TOF distribution at all flight times after the cutoff in these cases. In the heated drift tube case, direct emission electrons do not appear to be present much after 25 msec, thus the previous slow electron ratio method would not give a good indication of the effect of an applied force.

The analysis procedure used with this data is similar to the previous slow electron ratio method in that we do ratio applied

force spectra to the zero-applied-force spectrum taken in the same run; however, in this case the ratio of corresponding TOF channels or channel groups is used rather than just the ratio of the total number of counts arriving after a certain cutoff time. Individual channels are ratioed for channels 3-9, groups of either 2 or 5 channels for 10-19, groups of 5 for 20-49, and groups of 10 for channels 50-99. This channel averaging procedure in the late channels smooths out large statistical fluctuations in the data as well as allowing a noise elimination procedure to be used.

We often have a problem with large noise bursts (from transients in the electric power line) which couple into the counting electronics to produce a large number of spurious counts in a single TOF channel. This problem is most troublesome in the later channels, where the true count rate is small. In order to minimize the deleterious effects of the burst noise, we apply Chauvenet's criterion[51] to the groups of channels in the later portion of the spectrum. Chauvenet's criterion says that in a group of N similar measurements, a measurement may be rejected if the probability of its occurrence is less than 1/2N. In our case of a group of 10 similar TOF channels, this means that a count which is more than two standard deviations away from the mean for the group may be rejected (in our case, we replace it by the group mean).

We found that in the cases where Chauvenet's criterion was employed, the standard deviation of a point in the group was larger than $\sqrt{N}$ before replacement of the point in question by the group mean; after replacement the experimental standard deviation agreed well with the theoretical $\sqrt{N}$ value based on counting statistics.

The exact effect of an applied force on the type of distribution we described in Sec. 4.5.1 is highly dependent on the magnitude of the applied force; however, we can describe here the two basic effects in general terms. First, the direct emission electron TOF distribution will have a cutoff at

$$t_{max} = \sqrt{\frac{2|F|s}{m}}$$

where s is the effective length of the drift tube (slightly less than 1 m) and F is the effective applied force in the tube. The direct emission cutoff should make all ratios after the cutoff channel less than 1.0, although as the direct emission becomes a smaller and smaller fraction of the total distribution with increasing flight times the ratio will return to 1.0. For example, if direct emission becomes negligible at $\sim$25 msec, no value of applied force will affect the distribution after that time if only direct emission electrons are considered.

The second effect of an applied force is to delay the electrons which are emitted from traps, thus shifting the entire trap-originating distribution along the TOF axis, as discussed earlier. Under the monoenergetic assumption, this shift will be significant only for applied forces which have magnitudes not too much smaller than 10^{-7} eV/m. Since this portion of the distribution basically decreases with increasing flight times, a significant shift along the TOF axis will mean that all ratios after 20 msec or so will tend to be a bit larger than 1.0. The delayed electron time shift effect and the direct emission cutoff effect will in general tend

to cancel one another to some extent. We can see this more clearly by proceeding to a discussion of the specific cases.

4.5.3 Data at 4.2°K

Table 4.1 shows, for each value of applied force F_i, the ratio R_i of the normalized number of electrons in the given TOF range of the $F = F_i$ spectrum to the number of electrons in the same TOF range of the $F = 0$ spectrum. The indicated uncertainties in the ratios represent only the errors arising from counting statistics, calculated according to the equation

$$\sigma(R_i) = R_i \sqrt{\left(\frac{\sqrt{n(F_i)}}{n(F_i)}\right)^2 + \left(\frac{\sqrt{n_0}}{n_0}\right)^2}$$

where $n(F_i)$ and n_0 are the numbers of electrons in the given TOF range of the $F = F_i$ and $F = 0$ distributions respectively. Let us assume for the moment that the ratio will have its smallest value for the TOF interval within which the cutoff occurs; we then need only identify for each value of applied force the TOF interval in Table 4.1 for which R_i is minimum. Because of the uncertainties in R_i, this problem is not completely straightforward. We use the following criteria to determine the TOF values of the R_i minima and the uncertainties in these TOF values:

(1) a minimum, $R_i(\min)$, will be considered significant only if $R_i(\min) + \sigma\left(R_i(\min)\right) < 1.0$

(2) we consider any values of R_i which are within one probable error $\left(0.67\ \sigma(R_i)\right)$ of the actual smallest value of R_i to be possible minima; the choice among

Table 4.1. Values of R_i, the ratio of the number of counts with applied force F_i to the number of counts with no applied force, for the indicated time of flight intervals. T = 4.2°K.

Force Index i	Applied Force F_i (eV/m)	Time of Flight (ms) 3-3.5	3.5-4	4-4.5	4.5-5	5-7.5	7.5-10	10-12.5	12.5-15
1	-3.0×10^{-8}	.98±.02	.89±.02	.96±.03	1.00±.04	.96±.03	.93±.06	.80±.08	.98±.13
2	-7.5×10^{-8}	.95±.02	.98±.02	.88±.03	.97±.04	.87±.03	1.04±.07	.80±.08	1.09±.13
3	-15.0×10^{-8}	.94±.02	1.00±.02	.95±.03	.95±.03	.92±.03	.98±.07	.78±.08	1.00±.12

	Time of Flight (ms) 15-17.5	17.5-20	20-22.5	22.5-25	25-30	30-35	35-40	40-45	45-50
	.72±.11	1.10±.17	.94±.14	.74±.12	1.14±.13	1.02±.13	1.02±.13	1.11±.13	.95±.12
	.83±.11	.92±.14	.89±.13	1.00±.14	.93±.10	1.03±.12	1.05±.12	.90±.10	.87±.10
	1.00±.13	1.26±.17	.94±.13	.86±.13	1.12±.12	1.19±.14	1.06±.12	1.00±.11	.93±.11

the possible minima must then be made by other means. Because of (2) the width of the TOF interval corresponding to a ratio minimum may be larger than the width of the single TOF averaging interval in which the minimum occurs; i.e., the TOF intervals adjacent to a minimum will be included in the range of times assigned to the minimum if they meet criterion (2) above.

Having thus determined the cutoff TOF range(s) for each value of applied force, we take the midpoint of the range to be the cutoff time and the TOF range itself as the uncertainty in the cutoff time. We then convert the cutoff times and their uncertainties to observed force values and their uncertainties according to the equation

$$F = \frac{2ms}{t^2} \approx \frac{1.14 \times 10^{-11} \text{ eV sec}^2/\text{m}}{t^2} \quad . \qquad (4.1)$$

For the case of the 4.2°K data, this yields Table 4.2. If we then plot the observed force values against the corresponding applied force values, we obtain Fig. 4.13. The straight line is a least squares fit to the three points which result if we assume that the 2.1×10^{-8} eV/m point is the proper observed force corresponding to the -3×10^{-8} eV/m applied force and that the 4.4×10^{-8} eV/m observed force point at the same applied force value is an artifact. The parameters of this fit are

intercept: 6.19×10^{-10} eV/m

slope: 0.62

coefficient of determination: 0.998.

The ambient effective force in the tube indicated by the above intercept should not be taken too seriously since we cannot expect to

Table 4.2. Values of t_{min}, the flight time for which R_i is minimum (as determined from Table 4.1), the corresponding value of R_i, and the corresponding observed force as calculated from Eq. (4.1). T = 4.2°K.

Force Index i	Applied Force F_i (eV/m)	t_{min} (ms)	$R_i(t_{min})$	Observed Force (eV/m)
1	-3.0×10^{-8}	15-17.5	.72 ± .11	$-(4.2^{+0.7}_{-0.6}) \times 10^{-8}$
		22.5-25	.74 ± .12	$-(2.0^{+.25}_{-.20}) \times 10^{-8}$
2	-7.5×10^{-8}	15-17.5	.83 ± .11	$-(4.3^{+0.7}_{-0.6}) \times 10^{-8}$
3	-15.0×10^{-8}	10-12.5	.78 ± .08	$-(9.0^{+2.4}_{-1.8}) \times 10^{-8}$

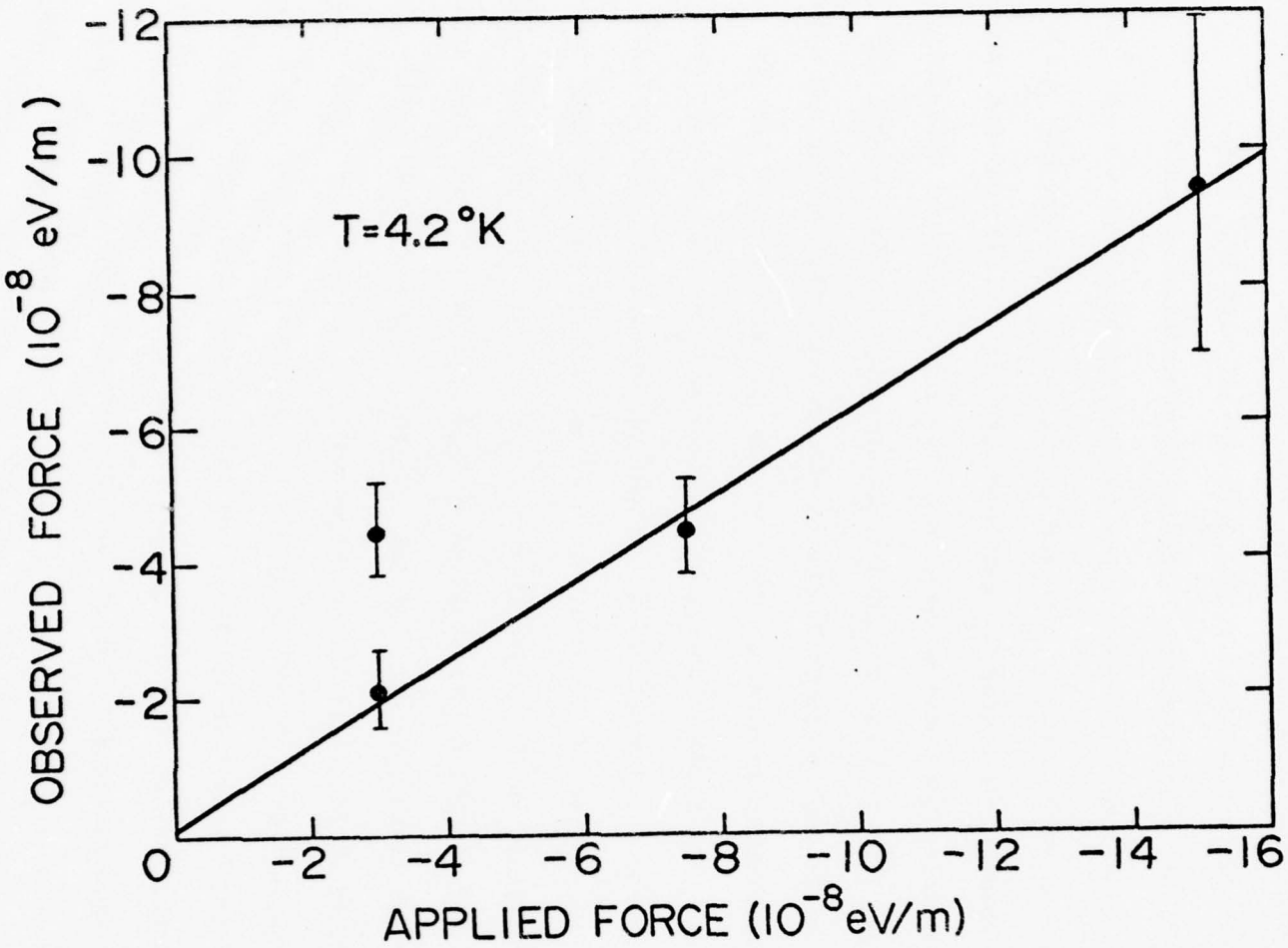


Fig. 4.13. A plot of the observed force (obtained from Table 4.1 and Eq. (4.1)) corresponding to each of three values of applied force. The straight line is a least squares fit to the data points other than the upper point corresponding to the smallest value of applied force.

extrapolate a three-point linear curve to a point approximately two orders of magnitude smaller than the points used in obtaining the fit with much accuracy; however, this intercept does indicate that the ambient effective force is much smaller than 10^{-8} eV/m, especially since the coefficient of determination of 0.998.

Additional evidence for the identification of the 4.4×10^{-8} eV/m point as an artifact is provided by Fig. 4.14. Whereas Fig. 4.13 was obtained by adding the data from several similar runs and then determining the location in time of the ratio minima as described above, Fig. 4.14 was obtained by determining the ratio minima for the three applied force values in each run and then taking the mean of the resulting measured force values for each value of applied force. The standard deviation of the mean σ_μ was also determined for each of the points of the graph; the error bars shown in Fig. 4.14 represent the uncertainty in observed force corresponding to an uncertainty in the cutoff time of $\pm\sigma_\mu$. Finally, a least squares fit was made to the points obtained by this procedure. The actual ambient field results obtained from the "scatter analysis" which is summarized in Fig. 4.14 are not expected to be as accurate as the results shown in Fig. 4.13 since many of the individual runs had only a few counts in some time intervals and thus displayed large statistical fluctuations in the force/no force ratios. However, the fact that the measured-versus-applied force line obtained by the "scatter analysis" technique does come closer (although not by much) to the smaller of the two measured force points corresponding to a 3×10^{-6} eV/m applied force helps to confirm that the smaller point is the correct one. We will make use of the "scatter analysis" technique

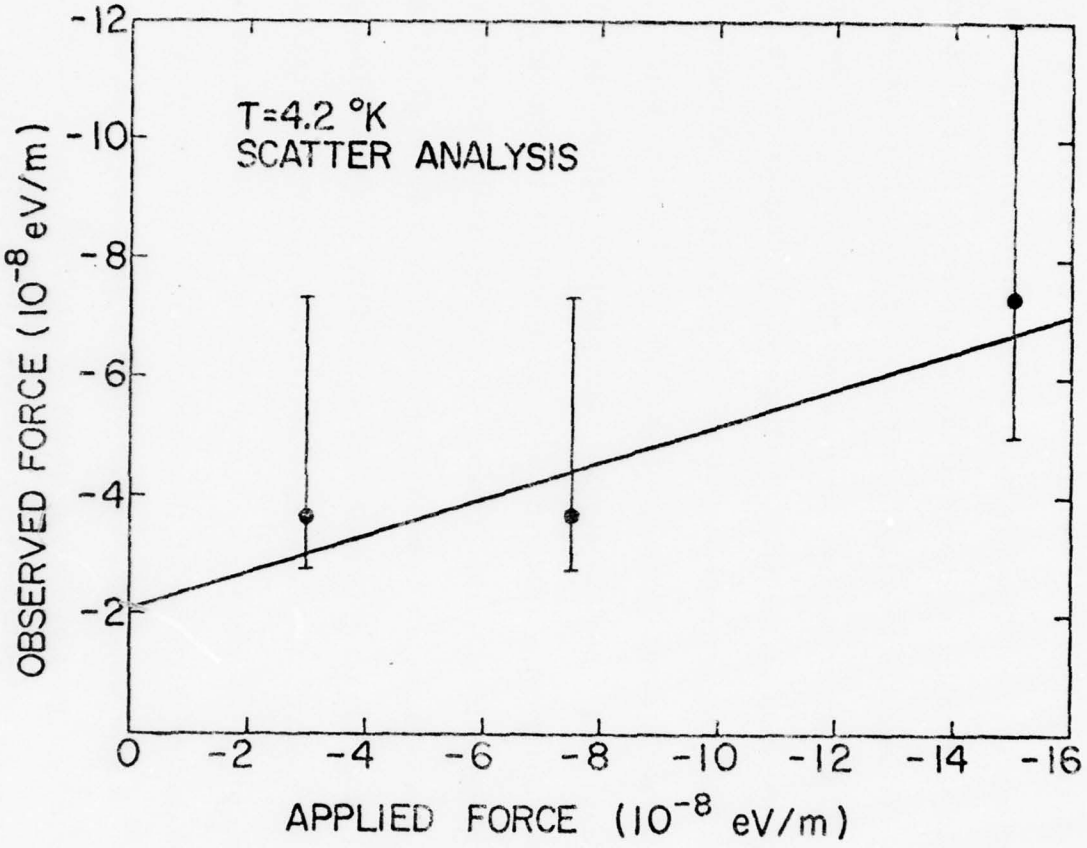


Fig. 4.14. A plot of observed versus applied force obtained by applying the scatter analysis technique described in the text to the 4.2°K data. The straight line is a least squares fit to the three points.

later to resolve other ambiguities in the identification of the correct observed force point when more than one reasonable possibility exists.

The slope of 0.62 of the least squares fit in Fig. 4.13 indicates that the applied force values calculated by multiplying the axial current in the tube walls by the measured resistance of the tube produce effective applied forces which are smaller by a factor of 0.62. We expect some reduction in the effective force values as compared to the calculated force values because of field penetration into the ends of the tube, as discussed in Chapter 3. It is also possible that our measurement of the drift tube resistance had a systematic error, although great care was taken in that measurement (again, see Chapter 3). One possible explanation for the sizeable reduction factor between the effective and calculated applied force values is the presence of non-negligible resistance in the joint between the leads to the drift tube and the drift tube itself. The connection is made with tight-fitting circumferential clamps, so there is always the possibility that sufficient oxidation has taken place between the clamp and the tube to provide a resistance which amounts to 0.2 - 0.3 of the total measured resistance of 1.5×10^{-6} Ω. In any event, we will use the effective force values determined by Fig. 4.13 in our future calculations; i.e., we will apply a correction factor of 0.62 to the applied force values obtained by measuring the axial tube current. Our three values of (effective) applied force are then -9.5×10^{-8} eV/m, -4.4×10^{-8} eV/m, and -2.1×10^{-8} eV/m.

Let us look at the effects of these force values on the trap-originating portion of the distribution, since Fig. 4.13 seems to establish that with the revised force values, cutoffs in the direct emission distribution occur at the proper times.

We have speculated that the trap-originating electrons begin to be emitted in significant quantities at about 4.5 msec and have flight times of about 5.5 msec, thus arriving at 10 msec. An applied force of -9.5×10^{-8} eV/m will shift this flight time to a new value of

$$t_f' = \frac{-1/t_f + \sqrt{(1/t_f)^2 + 2F/m}}{F/m} \approx 11 \text{ msec} . \qquad (4.2)$$

Thus if our speculations have any merit, the trap-originating electrons should now begin arriving at (4.5 + 11)msec = 15.5 msec and we might expect to see a peak in the slow electron ratios for $F = -9.5 \times 10^{-8}$ eV/m shortly after this TOF value. Looking at line 3 of Table 4.1 we see that indeed the ratio reaches a peak of 1.26 in the TOF range 17.25-19.75 msec. Also, as we discussed near the end of Sec. 4.5.2, we expect that the ratios after 20-25 msec should tend to be a bit larger than 1.0; again, a look at Table 4.1 shows that there is such a trend after 25 msec. This provides confirmation for our hypothesis that the direct emission distribution does not extend much beyond 25 msec, since the larger ratios after 25 msec indicate that the increase in the number of counts because of the shift of the delayed distribution is more important than the loss of counts due to the cutoff in the direct emission distribution.

Turning to the -4.4×10^{-8} eV/m applied force, we find by applying Eq. (4.2) that the delayed distribution will be shifted

by only about 1.0 msec. Since this is less than half the TOF group width used, we would not expect to see any significant peaks in the ratios for this force; Table 4.1 bears this out. We might also expect the ratios between the 16 msec (the cutoff time) and 25 msec to be a bit less than 1.0, with the ratios after 25 msec remaining close to 1.0. The data shows a slight tendency for the 17.25-30 msec ratios to be less than 1.0; however, the ratios after $\sim$ 40 msec show about the same tendency.

Finally, the smallest applied force, -2.1×10^{-8} eV/m, produces a negligible time shift of the delayed distribution, so that the cutoff should be the only prominent feature of this data. We might expect ratios of a bit less than 1.0 for several msec before the cutoff because of time-spreading of the low energy electrons; there is some evidence for this in the data.

Thus, considering all of the points discussed above, we feel that we have reasonably strong evidence that the ambient potential variations in the drift tube are less than 10^{-9} V/m at 4.2°K. This then is in agreement with both our earlier LHe data and with the measurements made by Witteborn and Fairbank in 1967.

We will now look at how this situation changes as we increase the temperature of the drift tube.

4.5.4 Data at 4.3°K

Table 4.3(a) presents the corresponding applied and observed force values for a drift tube temperature of 4.3°K. For the applied forces, we are using the revised values as discussed in the previous section.

Table 4.3. (a) Values of t_{min}, the corresponding R_i, and the corresponding observed force for T = 4.3°K.

Force Index i	Applied Force F_i (eV/m)	t_{min} (ms)	$R_i(t_{min})$	Observed Force (eV/m)
1	-2.1×10^{-8}	12.5-5	$.82 \pm .09$	$-(6^{+1.2}_{-1.0}) \times 10^{-8}$
2	-4.4×10^{-8}	5-5.5	$.87 \pm .04$	$-(4.1^{+.45}_{-1.35}) \times 10^{-7}$
		$13.75^{+1.25}_{-3.75}$	$.87 \pm .10$ $.92 \pm .09$	$-(6^{+5.4}_{-1.0}) \times 10^{-8}$
3	-9.5×10^{-8}	9-9.5	$.81 \pm .11$	$-(1.3^{+0.1}_{-0.1}) \times 10^{-7}$
		20-22.5	$.72 \pm .10$	$-(2.45^{+0.4}_{-0.2}) \times 10^{-8}$

(b) Values of t_{max} and the corresponding R_i for T = 4.3°K when upward applied forces were used.

Force Index i	Applied Force F_i (eV/m)	t_{max} (ms)	$R_i(t_{max})$
1	$+2.1 \times 10^{-8}$	8-12	$1.26 \pm .27$
2	$+4.4 \times 10^{-8}$	8-8.5	$1.34 \pm .29$
3	$+9.5 \times 10^{-8}$	6-6.5	$1.16 \pm .22$
		8-8.5	$1.08 \pm .24$
		12.5-15	$1.07 \pm .19$

The smallest applied force gave an unambiguous determination of the observed force; however, each of the larger two applied forces has two corresponding observed force values which meet the criteria discussed in the preceding section.

These results are plotted in Fig. 4.15. If we use the smaller of the two observed force values corresponding to the -4.4×10^{-8} eV/m applied force and the larger observed force value for the -9.5×10^{-8} eV/m applied force, a linear regression analysis yields the solid line shown in the figure. The parameters of this fit are:

intercept: -2.78×10^{-8} eV/m

slope: 1.06

coefficient of determination: 0.82.

In analyzing the data taken at temperatures above 4.2°K we are primarily interested in determining the equivalent ambient electric field in the tube; i.e., the intercept of the observed-versus-applied force line. Once we have determined the effective drift tube resistance, as we did in Sec. 4.5.3, we can accurately specify the actual effective applied force that was used in each set of measurements. Thus we expect that when the proper values of applied force are used, the observed versus applied force line should always have a slope of 1.0, since a given change in the applied force should produce exactly the same change in the observed force. In order to get the best determination of the intercept in our force plots, we will generally constrain the slope of the measured-versus-applied force line to be 1.0; that is, we will find the least squares fit which has unit slope (often a visual fit will be quite adequate). The dashed line in Fig. 4.15 represents a visual

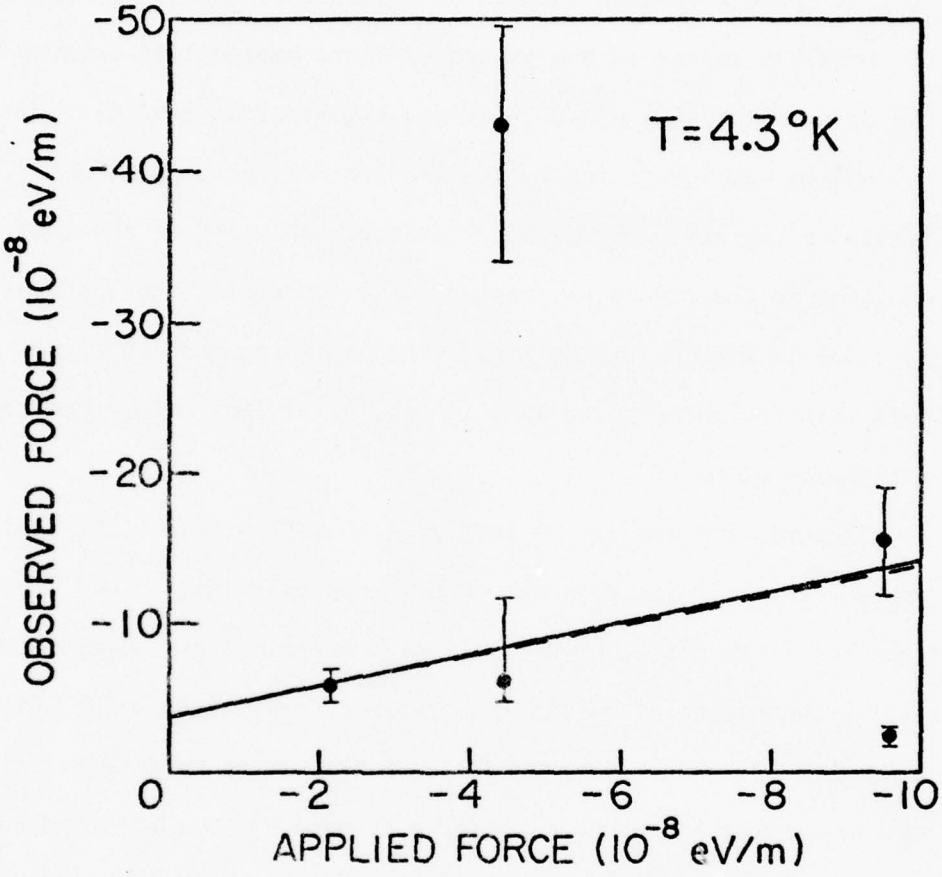


Fig. 4.15. The observed force results with the drift tube at 4.3°K. The solid line is an unconstrained least squares fit to the three data points which are near the line while the dashed line is a visual best-fit unit-slope line fitted to the same three points.

best fit line having slope 1.0. Of course, since the unconstrained least squares fit had a slope of 1.06, the two lines are quite similar.

It appears that our choice of observed force values from the two possible values in the two cases where ambiguities existed is the only choice that yields a reasonable straight line fit. However, to confirm our identification of the two remaining points as artifacts, we again performed a "scatter analysis" of the type employed in the preceding section. The force plot thus obtained is shown in Fig. 4.16. Note that the least squares fit agrees quite well with the force-force line in Fig. 4.15, thus helping to confirm our choice of points.

The results summarized in Fig. 4.15 indicate that the equivalent ambient electric field in the tube is approximately $+3 \times 10^{-8}$ V/m. Because of the nature of the data (the experimental "points" should really be thought of as experimentally determined observed force ranges rather than actual points with associated uncertainties) and the requirement that the slope of the force-force line be constrained to 1.0, it is difficult to provide a precise estimate of the error in this ambient field determination. A proper error analysis would seem to require numerical differentiation of a chi-square map of constrained least squares fits having a range of observed force intercepts. The rather limited precision of the data hardly warrants such a lengthy treatment. Also, we are really more interested in obtaining an order of magnitude estimate of the ambient field than in determining a precise value. Efforts to make constrained visual fits with different intercepts show that it is reasonable to quote

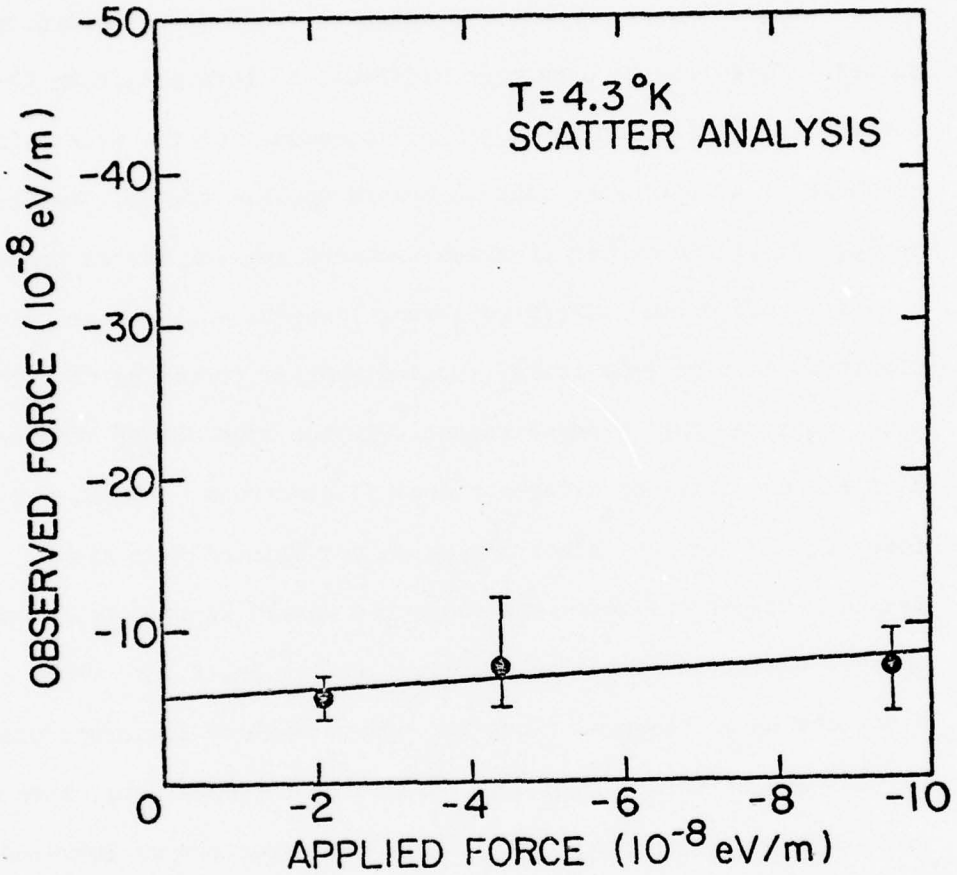


Fig. 4.16. The scatter analysis plot for the 4.3°K data. The straight line is a least squares fit to the points.

our result for the ambient electric field in the tube at 4.3°K as $(3^{+4}_{-2}) \times 10^{-8}$ V/m.

4.5.5 4.3°K Data with Upward Applied Forces

A small amount of data was taken at 4.3°K using upward applied forces. This data is even more difficult to interpret than the downward applied force data, primarily because of the much different response of trapped electrons to upward applied fields. We discussed in Sec. 4.5.2 the manner in which downward applied forces produce both a cutoff of the direct emission electrons and a retardation of electrons emitted from traps. Upward applied forces on the other hand, although they produce essentially the same cutoff effects, have a much different effect on trapped electrons. First, the upward force accelerates any electrons which are emitted from traps. Second, and perhaps more important, the upward force acts to cancel to some extent the potential barriers in the drift tube which cause electrons to be trapped. Thus the upward applied force produces a certain amount of de-trapping. Because of these effects, several peaks and nulls tend to appear in the time spectrum of force/no force ratios. This is particularly the case for the larger values of upward applied force.

If there is actually an ambient electric field in the tube of $+3 \times 10^{-8}$ V/m [producing a (downward) force of -3×10^{-8} eV/m on an electron] we expect that the application of successively larger values of upward applied force will first reduce the net observed force to zero and then make it positive (i.e., negative equivalent observed electric field). A glance at Fig. 4.17 shows that there is a good case for the identification of such behavior in the data.

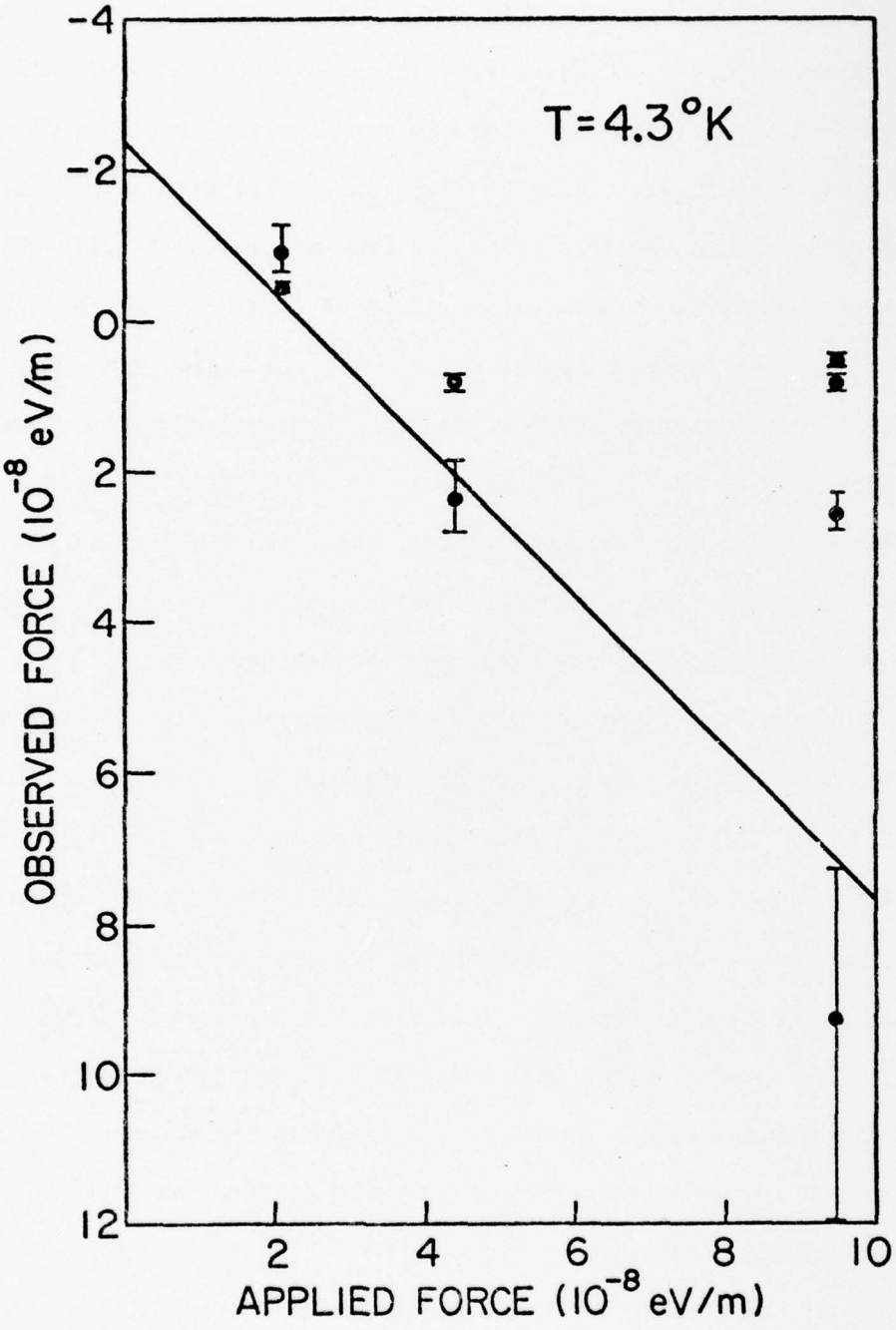


Fig. 4.17. The observed force results obtained with upward applied forces. The drift tube was at 4.3°K.

In this figure we have plotted both positive and negative values of observed force on the y-axis against positive (upward) applied force on the x-axis. The line shown is a visual best fit obtained under the constraint that the slope be +1.0 (note that because of the axes chosen for this plot, the line has an inclination which we would normally associate with a slope of -1.0). As we expected, the force/no force ratios go through several minima (and thus there are several observed force values for each applied force value), especially in the case of the $+9.5 \times 10^{-8}$ eV/m applied force. However, with the slope constraint, the line displayed is the only one which provides a reasonable fit to <u>one</u> of the possible observed force values corresponding to each applied force.

Again, the important piece of information to be gleaned from this graph is the observed force intercept of approximately -2.4×10^{-8} eV/m (with an uncertainty of roughly $(^{-0.4}_{+1.0}) \times 10^{-8}$ eV/m, obtained by constructing acceptable fits having minimum and maximum intercepts), which we presume to be the ambient force in the tube. Note that this agrees quite well with the estimate of $(-3^{-4}_{+2}) \times 10^{-8}$ eV/m obtained from the downward applied force data. The way in which the upward and downward applied force lines connect to form one continuous curve certainly helps to confirm the validity of our method of analysis.

Identification of the observed forces in Fig. 4.17 as positive rather than negative is made on the basis of an analysis of the trapped electron peak which we described in connection with the 4.2°K data. If a graph of the type presented in Fig. 4.11 is constructed for the 4.3°K data, we find that the 4.3°K arrival time

distribution of trap-originating electrons has a peak in the range 10-12 msec. If we select the midpoint of this interval, 11 msec, as t_t, the minimum transit time for trap-originating electrons when no applied forces are present, and employ Eq. (4.2) we can calculate the expected arrival time of the trapped electron peak for the applied force cases by substituting t_t = 11 msec for t_f in the equation. If a given positive applied force actually shifts the net force in the tube in the positive direction by an amount equal to its magnitude then the shifted trapped electron peaks should show up in the data as maxima in the force/no force ratios occurring at the predicted times. (Actually the maxima may tend to occur a bit earlier than anticipated because of the presumed partial lowering of potential barriers by upward applied forces.) The predictions of Eq. (4.2) for t_t', the shifted arrival time of the trap-originating electrons are

$$F_a = +2.1 \times 10^{-8} \text{ eV/m} \qquad t_t' = 9.26 \text{ msec}$$

$$F_a = +4.4 \times 10^{-8} \text{ eV/m} \qquad t_t' = 8.16 \text{ msec}$$

$$F_a = +9.5 \times 10^{-8} \text{ eV/m} \qquad t_t' = 6.78 \text{ msec.}$$

Reference to Table 4.3(b) shows that these predictions agree quite well with the force/no force ratio maxima in the data.

Thus both the downward and upward applied force data indicate an equivalent ambient electric field of $\sim +3 \times 10^{-8}$ eV/m in the drift tube at 4.3°K. It appears that the surface shielding whose presence we hypothesize at 4.2°K has already become less effective with only a 0.1°K rise in temperature. We shall later see that a

slightly larger increase in temperature seems to almost completely eliminate the apparent shielding effect.

4.5.6 Data at 4.4°K

Table 4.4 and Fig. 4.18 present the 4.4°K data. In this data the analysis is not complicated by multiple (separated) observed force values for any of the applied forces; however, two of the observed force ranges are quite large. A reasonable constrained-slope fit is shown; this line predicts an ambient force of about $(-3.1^{-2.4}_{+0.4}) \times 10^{-7}$ eV/m at 4.4°K (again the error limits are determined by finding the constrained-slope lines with minimum and maximum intercept which pass through two of the three observed force ranges).

4.5.7 Data with Upward Applied Forces at 4.4°K

Only one short run was taken with upward applied forces at 4.4°K; however, the data will be described for completeness. Table 4.4(b) and Fig. 4.19 present the data. We seem to have reasonably good observed force determinations at applied forces of $+2.1 \times 10^{-8}$ and $+9.5 \times 10^{-8}$ eV/m. The situation for the $+4.4 \times 10^{-8}$ eV/m applied force is quite ambiguous. Actually the upper two observed force points at this applied force value only meet criterion (2) of Sec. 4.5.3; however, they are quite close to meeting criterion (1) so we included them in order not to miss any possibly valid points.

When the slope of the force-force line is constrained to be 1.0, the line shown is the only reasonable fit. Once again making use of maximum and minimum intercept constrained lines to estimate the error in the intercept, we obtain an ambient force value of $(-2.4^{-0.2}_{+0.8}) \times 10^{-7}$ eV/m. Again the agreement with the downward applied

Table 4.4. (a) Values of t_{min}, the corresponding R_i, and the corresponding observed force for T = 4.4°K.

Force Index i	Applied Force F_i (eV/m)	t_{min} (ms)	$R_i(t_{min})$	Observed Force (eV/m)
1	-2.1×10^{-8}	6-6.5	$.78 \pm .06$	$-(2.9^{+.25}_{-.20}) \times 10^{-7}$
2	-4.4×10^{-8}	$5.25^{+.25}_{-.75}$	$.89 \pm .05$ $.90 \pm .05$	$-(4.12^{+1.5}_{-.35}) \times 10^{-7}$
3	-9.5×10^{-8}	$4.75^{+.75}_{-.75}$	$.91 \pm .05$ $.89 \pm .04$	$-(5.0^{+2.10}_{-1.25}) \times 10^{-7}$

(b) Values of t_{max}, the corresponding R_i, and the corresponding observed force for T = 4.4°K when upward applied forces were used.

Force Index i	Applied Force F_i (eV/m)	t_{max} (ms)	$R_i(t_{max})$	Observed Force (eV/m)
1	$+2.1 \times 10^{-8}$	7.5-10	$.48 \pm .17$	$-(1.5^{+0.5}_{-0.4}) \times 10^{-7}$
		40-45	$.61 \pm .23$	$-(6.3^{+0.8}_{-0.7}) \times 10^{-9}$
2	$+4.4 \times 10^{-8}$	4-4.5	$.72 \pm .29$	$-(6.3^{+0.8}_{-0.7}) \times 10^{-7}$
		7.5-10	$.84 \pm .25$	$-(1.5^{+0.5}_{-0.4}) \times 10^{-7}$
		15-20	$.74 \pm .22$	$-(3.7^{+1.3}_{-0.9}) \times 10^{-8}$
		40-45	$.52 \pm .18$	$-(6.3^{+0.8}_{-0.7}) \times 10^{-9}$
3	$+9.5 \times 10^{-8}$	$8.25^{+1.25}_{-1.25}$	$.52 \pm .18$	$-(1.5^{+0.5}_{-0.4}) \times 10^{-7}$

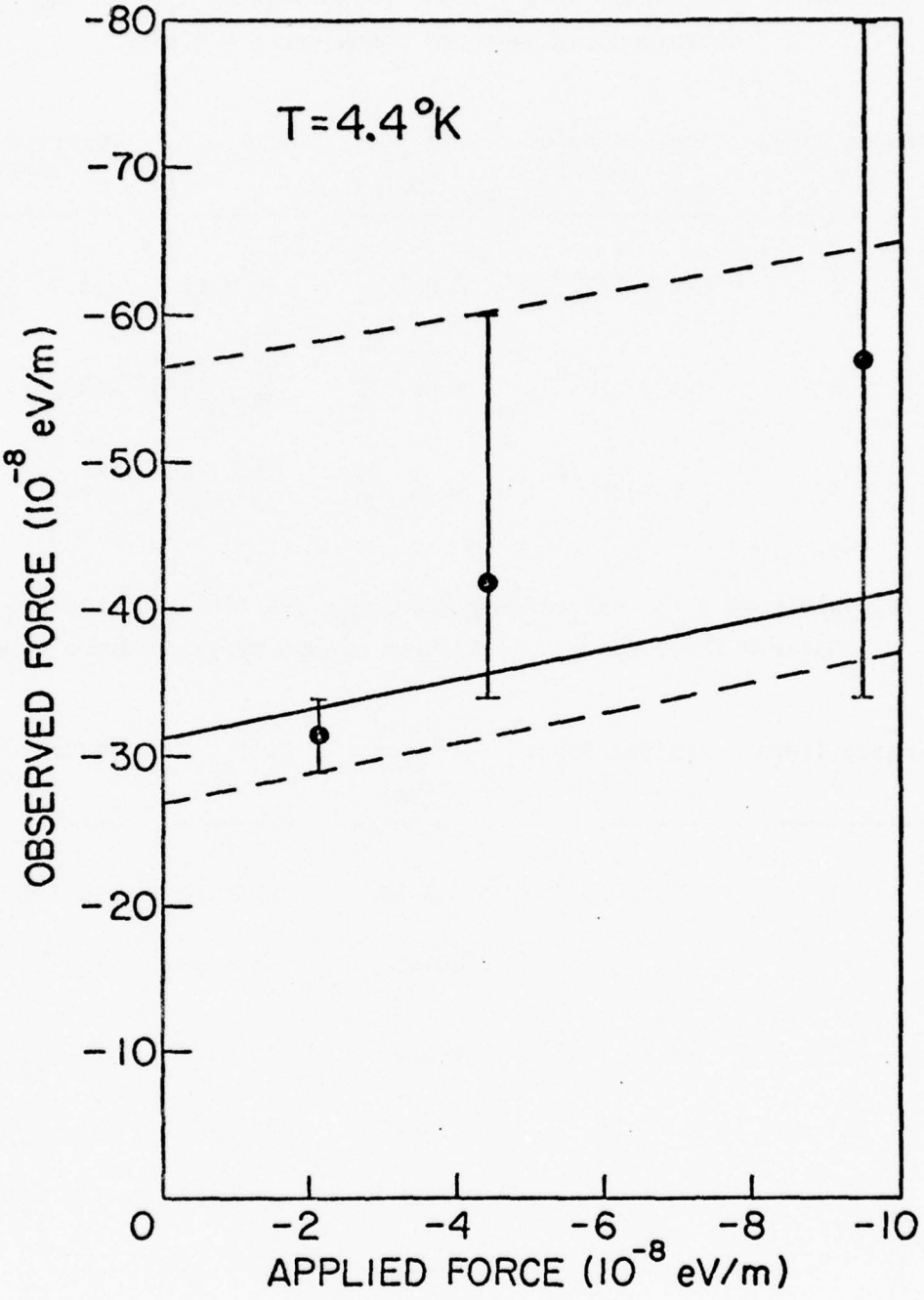


Fig. 4.18. The observed force results corresponding to a drift tube temperature of 4.4°K. The solid line is a visual best-fit unit-slope line. The dashed lines indicate the minimum and maximum y-intercept values which a unit-slope line can have if it is to be reasonably consistent with the data.

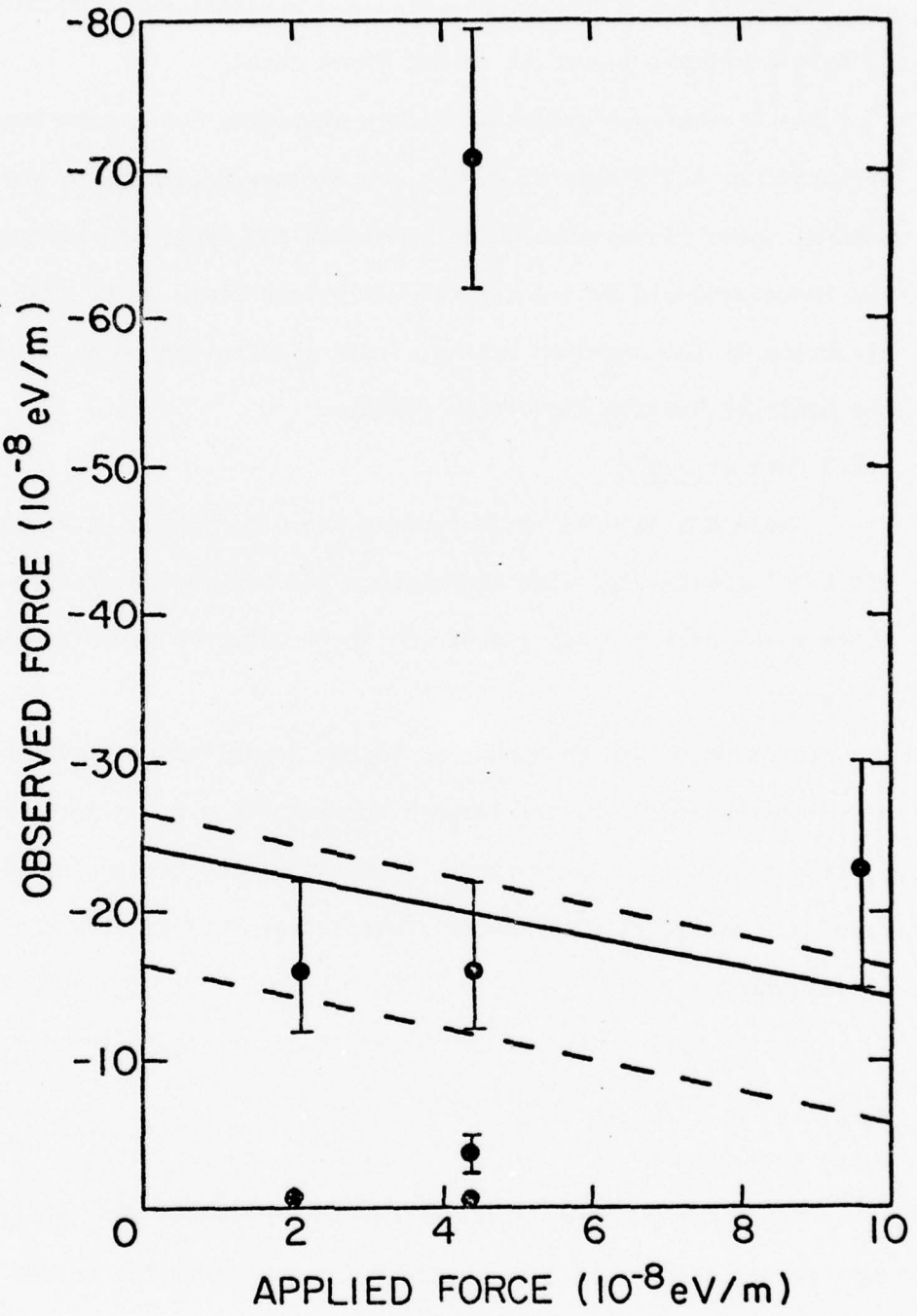


Fig. 4.19. The observed force results obtained at 4.4°K with upward applied forces. The solid line is a visual best fit having unit slope while the dashed lines again indicate minimum and maximum intercepts.

force data is reasonably good; this is a pleasant surprise in view of the very small amount of upward force data.

We see that our proposed surface shielding has become even less effective at 4.4°K than at 4.3°K. We are now beginning to see an ambient force in the tube which is within the range of estimates for the force produced by the lattice distortion field (note that the direction of the observed ambient field is also that expected on the basis of lattice distortion fields).

4.5.8 Data at 6.3°K

Table 4.5 and Fig. 4.20 present the 6.3°K data. A visual best fit constrained-slope line and minimum and maximum contrained-slope lines which pass through two of the three observed force ranges are shown.

In order to add confirmation to the identification of the upper point corresponding to the largest applied force as an artifact, a scatter analysis was performed. Figure 4.21 is the plot resulting from that analysis; the scatter analysis seems to provide the desired confirmation.

Thus we will quote our 6.3°K results from Fig. 4.20 as

$F_{ambient} = (-3.5^{-0.6}_{+0.15}) \times 10^{-7}$ eV/m.

4.5.9 Data at 9°K

Table 4.6 and Fig. 4.22 present this data and show the usual constrained-slope fits. We obtain from the figure the result

$F_{ambient} = (-2.7^{-1.4}_{+0.6}) \times 10^{-7}$ eV/m.

Table 4.5. Values of t_{min}, the corresponding R_i, and the corresponding observed force for T = 6.3°K.

Force Index i	Applied force (eV/m)	t_{min} (ms)	$R_i(t_{min})$	Observed Force (eV/m)
1	-2.1×10^{-8}	5.25±.75	.93 ± .07	$-(4.1^{+1.5}_{-.09}) \times 10^{-7}$
2	-4.4×10^{-8}	5.25±.50	.88 ± .06	$-(4.1^{+0.9}_{-0.6}) \times 10^{-7}$
		7.25±.50	.80 ± .12	$-(2.2^{+0.3}_{-0.3}) \times 10^{-7}$
3	-9.5×10^{-8}	3.75±.50	.75 ± .04	$-(8.1^{+1.9}_{-1.8}) \times 10^{-7}$
		5.5±.75	.75 ± .06	$-(4.1^{+0.9}_{-1.2}) \times 10^{-7}$

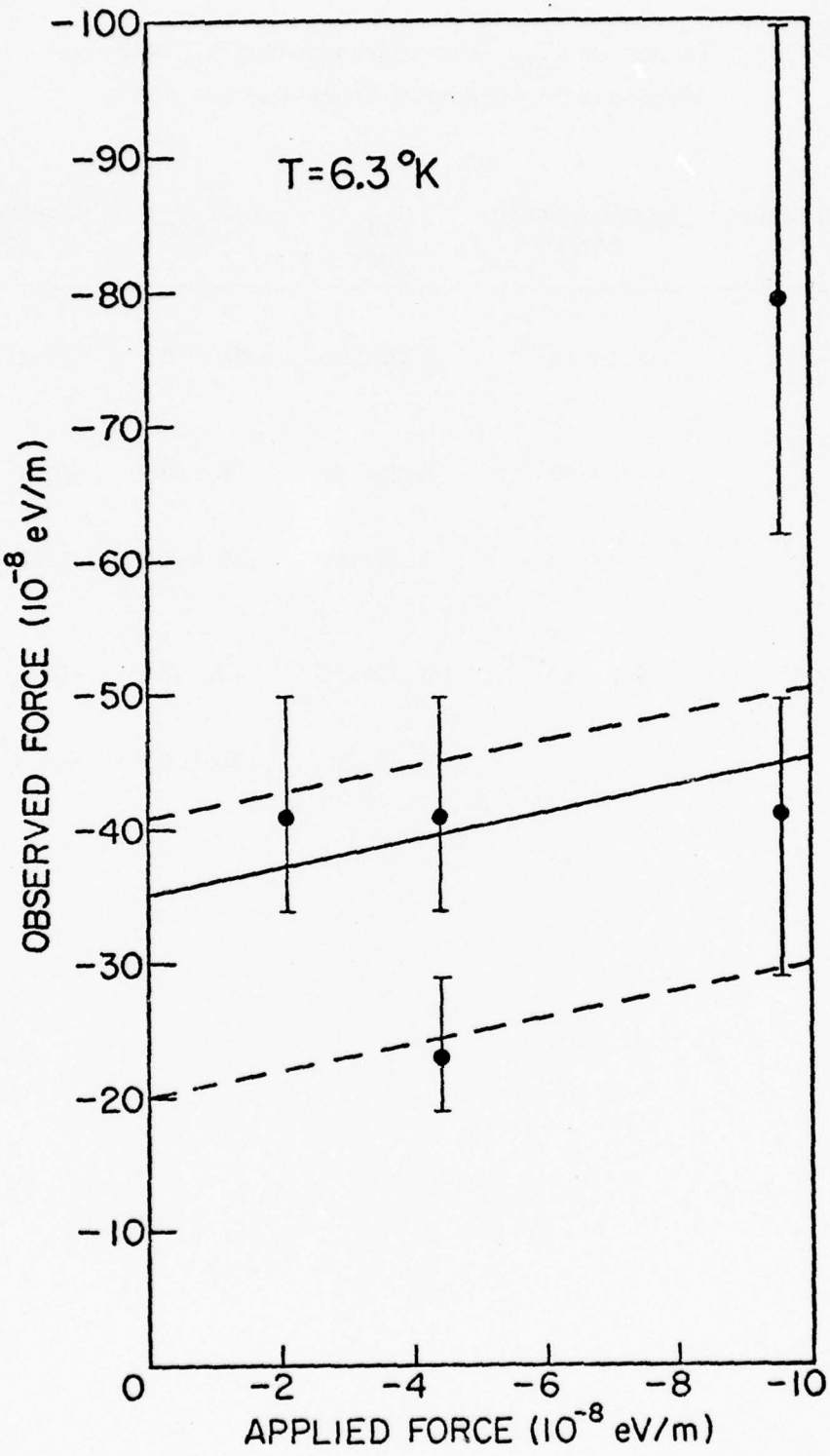


Fig. 4.20. The observed force results obtained at 6.3°K.

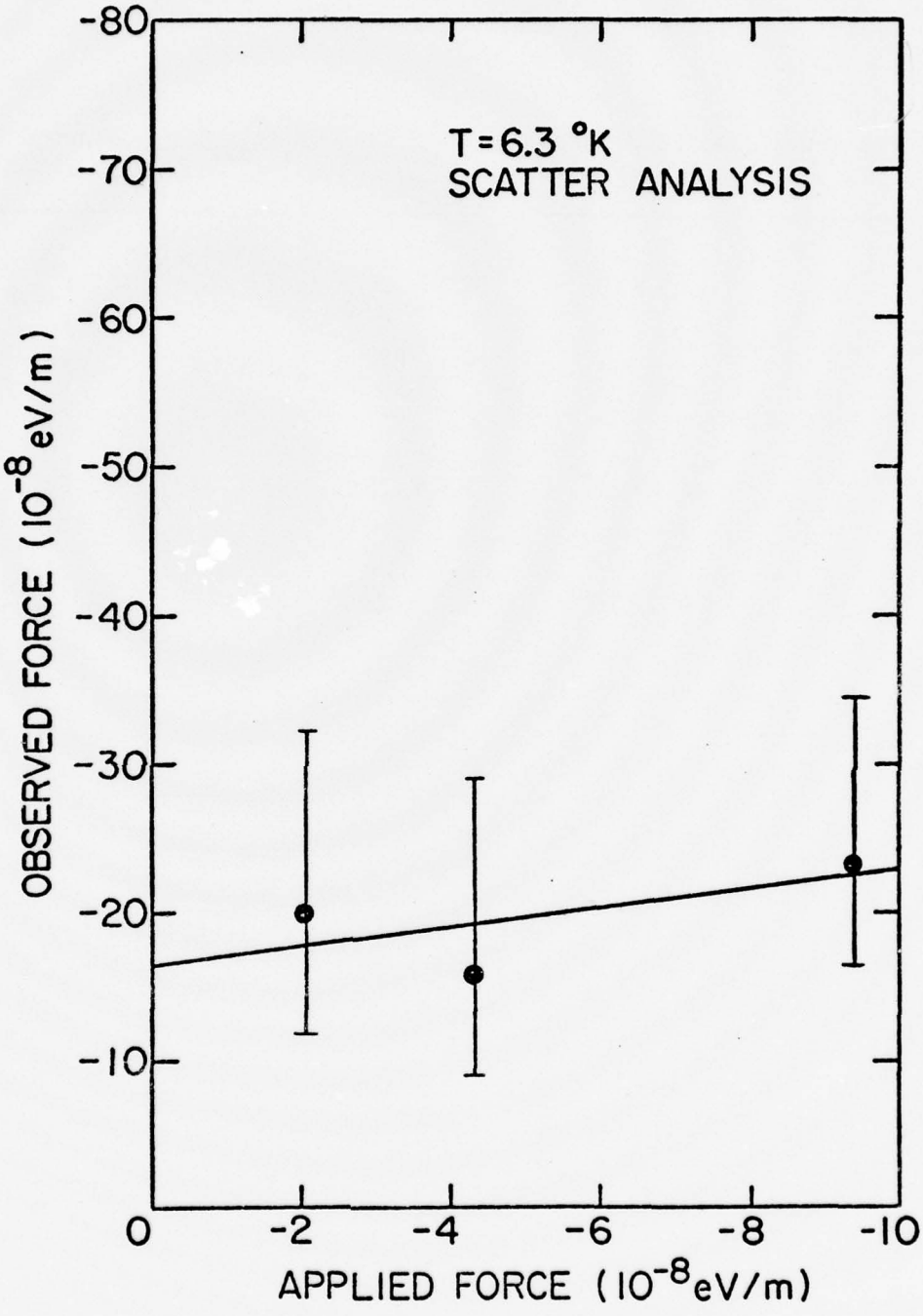


Fig. 4.21. The scatter analysis observed force results at 6.3°K.

Table 4.6. Values of t_{min}, the corresponding R_i, and the corresponding observed force for T = 9°K.

Force Index i	Applied Force F_i (eV/m)	t_{min} (ms)	$R_i(t_{min})$	Observed Force (eV/m)
1	-2.1×10^{-8}	$4.0 \pm .25$	$.87 \pm .12$	$-(7.1^{+1.0}_{-0.9}) \times 10^{-7}$
		$7.25^{+0.5}_{-2.25}$	$.92 \pm .09$	$-(2.2^{+2.3}_{-0.3}) \times 10^{-7}$
2	-4.4×10^{-8}	$3.5 \pm .25$	$.93 \pm .07$	$-(9.3^{+1.4}_{-1.3}) \times 10^{-7}$
3	-9.5×10^{-8}	$3.5 \pm .25$	$.91 \pm .06$	$-(9.3^{+1.4}_{-1.3}) \times 10^{-7}$

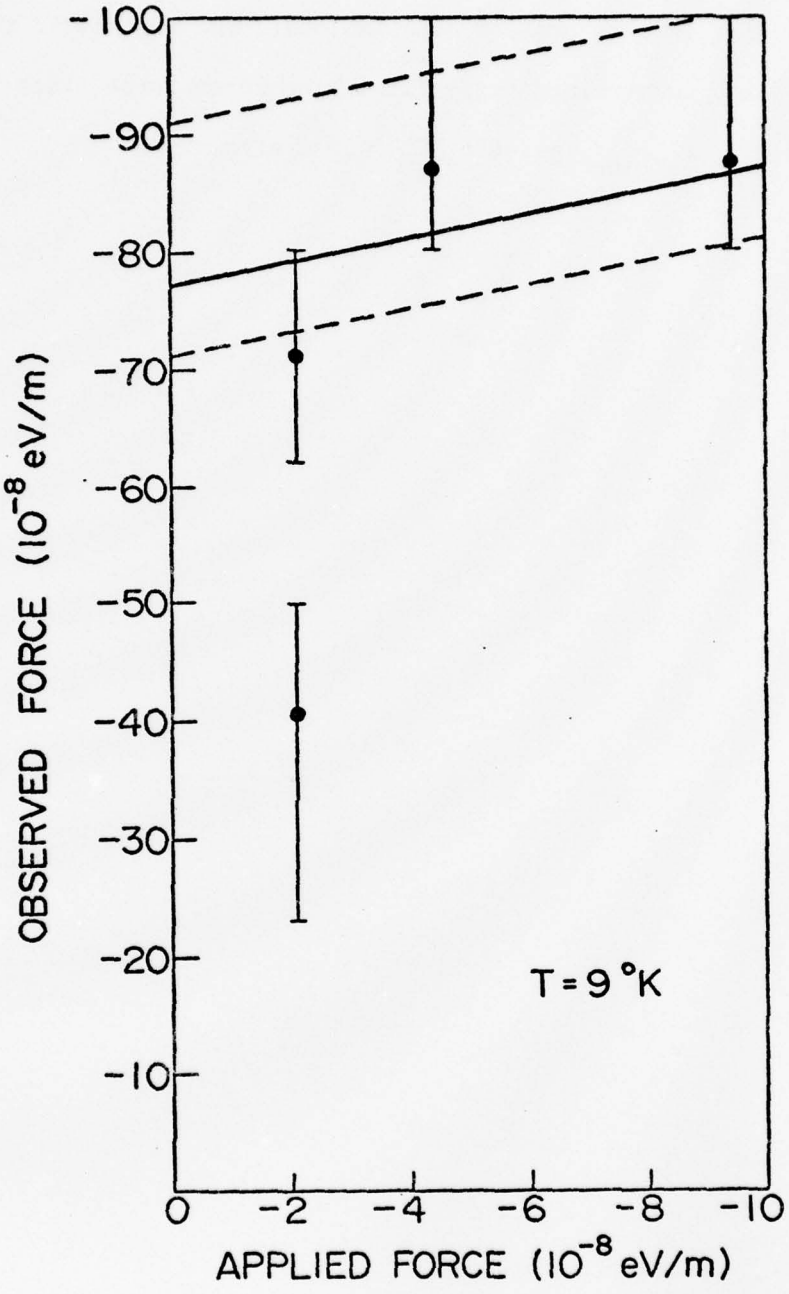


Fig. 4.22. The observed force results at 9°K.

4.5.10 Data at 11°K

The data is presented in Table 4.7 and Fig. 4.23; the figure shows the constrained-slope fits. The force-force lines imply a result of $F_{ambient} = (-6.6^{-1.0}_{+1.8}) \times 10^{-7}$ eV/m.

Table 4.7. Values of t_{min}, the corresponding R_i, and the corresponding observed force for T = 11°K.

Force Index i	Applied Force F_i (eV/m)	t_{min} (ms)	$R_i(t_{min})$	Observed Force (eV/m)
1	-2.1×10^{-8}	$2.5 \pm .25$	$.77 \pm .11$	$-(5.6^{+0.7}_{-0.6}) \times 10^{-7}$
2	-4.4×10^{-8}	$4.0^{+.75}_{-.25}$	$.89 \pm .10$	$-(7.1^{+1.0}_{-2.1}) \times 10^{-7}$
3	-9.5×10^{-8}	$3.5 \pm .25$	$.86 \pm .07$	$-(9.2^{+1.5}_{-1.1}) \times 10^{-7}$

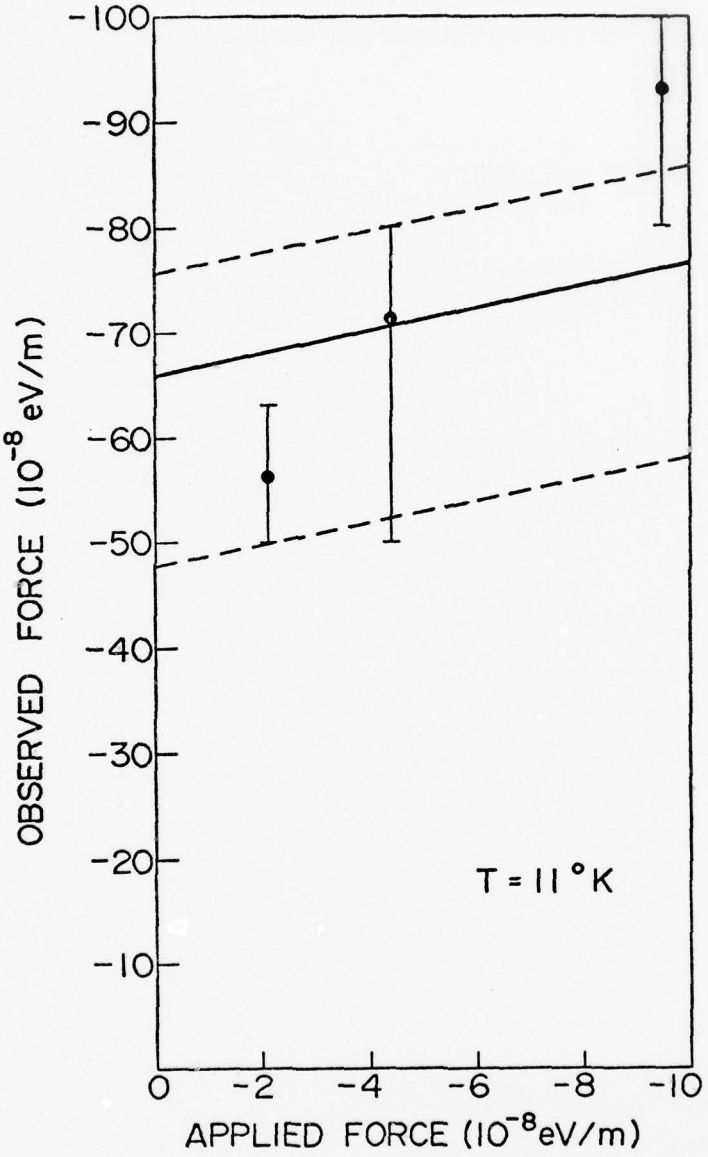


Fig. 4.23. The observed force results at 11°K.

CHAPTER 5

SUMMARY AND CONCLUSIONS

If we plot the observed ambient effective force in the drift tube at 4.2°K, 4.3°K, 4.4°K, and 6°K (as obtained from Figs. 4.13, 4.15, 4.18, and 4.20) against the amount by which the temperature exceeds 4.2°K, we obtain Fig. 5.1.

This figure illustrates the rather amazing temperature dependence of the observed ambient force on an electron in the tube. Our result at 4.2°K was that the ambient effective force was less than 10^{-9} eV/m; we take as the correct value at 4.2°K the Witteborn-Fairbank result that the net force is $(0 \pm 5) \times 10^{-12}$ eV/m. We then see from Fig. 5.1 that at a temperature only 0.2°K higher than 4.2°K the ambient force is roughly 5 orders of magnitude larger. If we add to the plot the ambient forces seen at 9°K and 11°K (obtained from Fig. 4.22 and Fig. 4.23), we get Fig. 5.2. In this figure it appears that the ambient effective force is varying slightly between 6°K and 11°K. However, it is clear that almost all of the temperature dependence occurs between 4.2°K and 4.4°K. The ambient force is probably constant between 9°K and 11°K.

We can obtain additional confirmation of the basic correctness of our determination of the behavior of the ambient effective force acting on an electron in the drift tube as the tube temperature is raised above 4.2°K by performing another type of ratio analysis. From our discussion in Chapter 4 of the ratio analysis technique as used in the case of applied forces, we came to the conclusion that the R_i values for the TOF spectrum with a given value of applied force ought to reach a minimum in the TOF interval

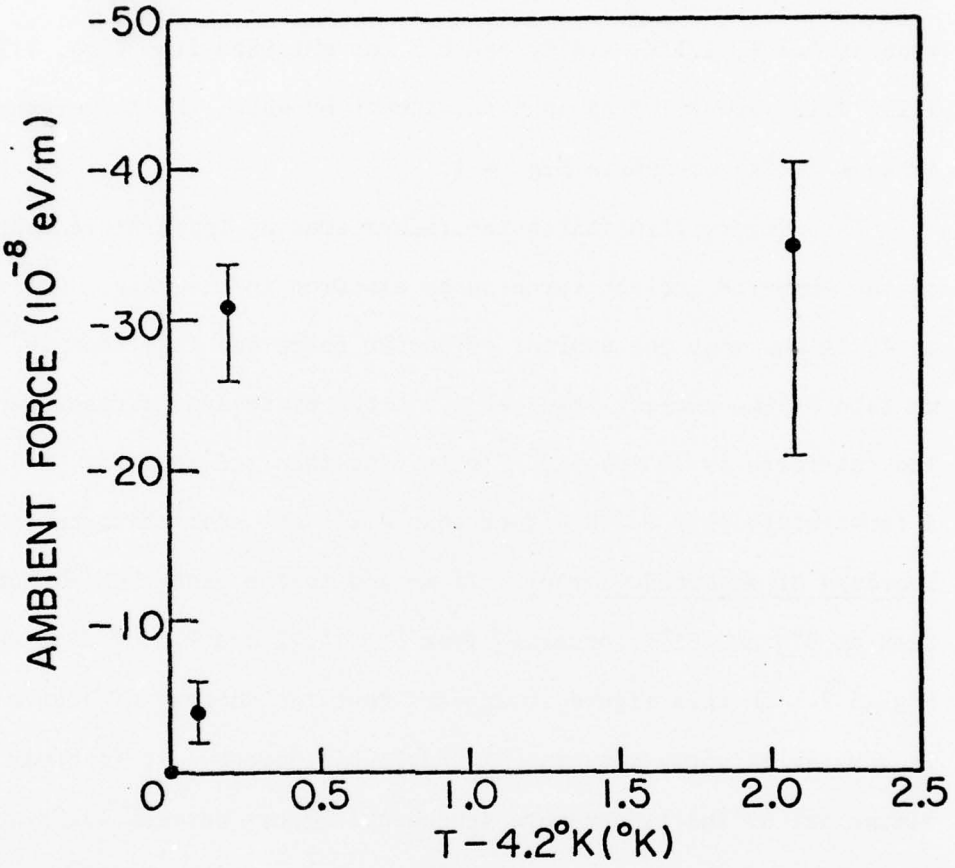


Fig. 5.1. A summary of the temperature dependence of the observed ambient force in the drift tube showing the results at the four lowest temperature values.

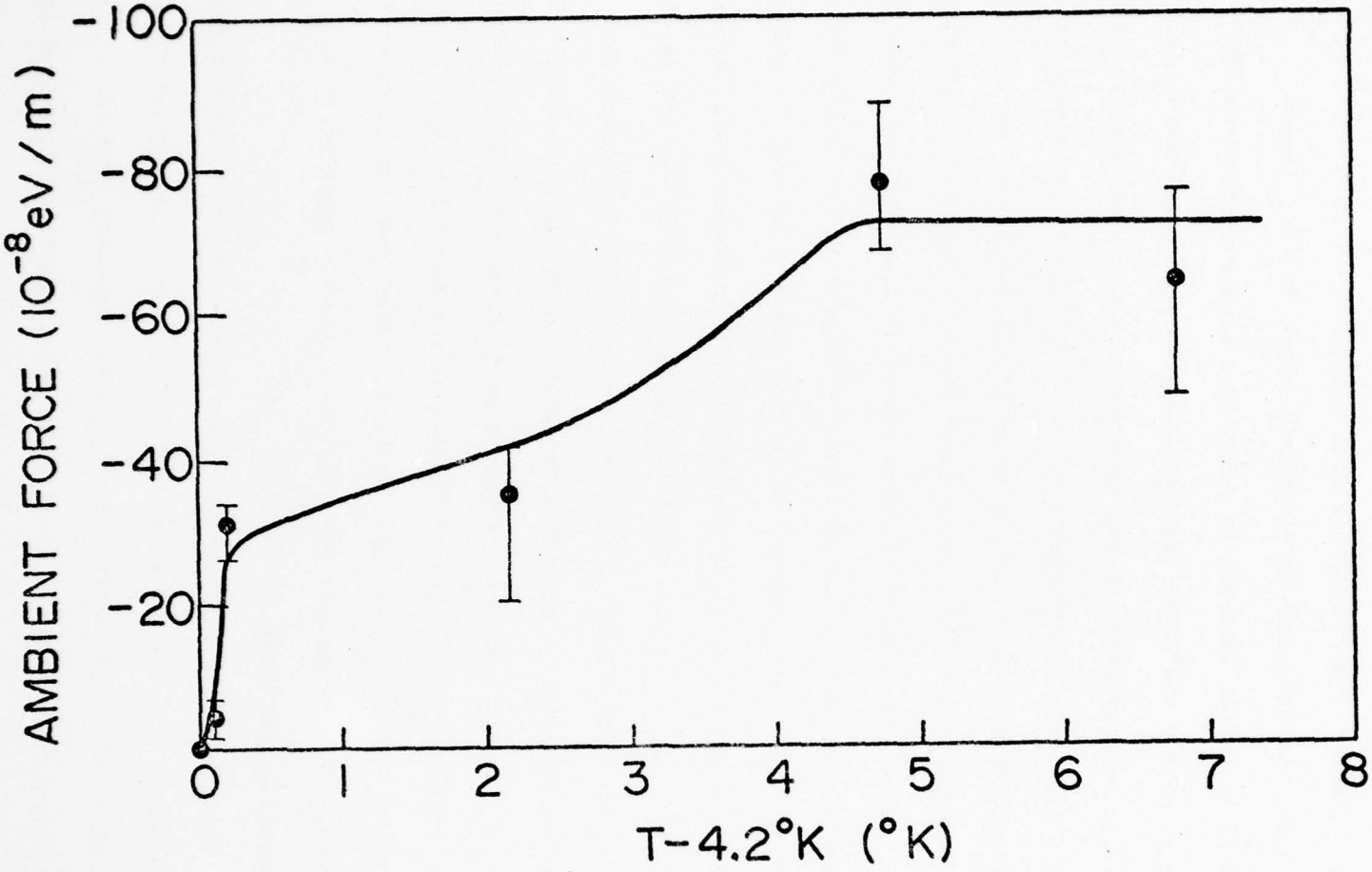


Fig. 5.2. A summary of the temperature dependence of the observed ambient force in the drift tube showing all results obtained in the heated drift tube work. The curve is only a guide to the eye and does not represent a theoretical fit.

corresponding to the theoretical cutoff time for the given force. Now if ambient forces are appearing in the drift tube when its temperature is raised above 4.2° K, then a table of R_i values obtained by ratioing a higher temperature TOF spectrum with a 4.2°K TOF spectrum ought to show a minimum R_i in the TOF range corresponding to the theoretical cutoff time for the ambient force present at that temperature. Such a table of R_i values for the temperatures we have used is presented in Table 5.1. We see that indeed there is a definite minimum in the R_i values for each temperature. If we then convert the time interval in which the minimum R_i occurs to a value of effective observed ambient force (taking the midpoint of the time interval to get the force value and the endpoints of the time interval to get the uncertainty in force) using Eq. (4.1) we obtain Fig. 5.3. Note that this is quite similar (except for the temperatures very near 4.2°K) to Fig. 5.2. We do not expect this method to be quite as quantitative as the method used to obtain Fig. 5.2; however, it does provide a nice independent check of the basic validity of the applied force-observed force fits made in Chapter 4. It thus seems that we have another piece of evidence that the change in the ambient force in the tube with temperature is essentially that shown in Fig. 5.2.

Thus the ambient effective electric field in the tube between 4.4°K and 11°K is in the range $+(2\text{-}9) \times 10^{-7}$ V/m. This value of ambient field is consistent with the field expected from the gravitationally-induced distortion of the ion lattice discussed in Chapter 2. Our measurements at 300°K and 77°K are consistent with

Table 5.1. Values of the ratio of the number of counts in the indicated TOF interval for the given value of temperature to the number of counts in the same TOF interval with T = 4.2°K.

Temperature (°K)	Time of Flight (ms) 1.5-2	2-2.5	2.5-3	3-3.5	3.5-4	4-4.5	4.5-5	5-7.5
4.3°K	.78	.70	.64	.59	.60	.55	.57	.53
4.4°K	.92	.72	.61	.52	.53	.52	.37	.53
6.3°K	.54	.43	.36	.31	.32	.29	.27	.28
9°K	.53	.30	.19	.12	.11	.10	.12	.16
11°K	.44	.24	.15	.10	.08	.07	.07	.11

7.5-10	10-15	15-20	20-25	25-30	30-35	35-40	40-45	45-50
.75	1.06	1.19	1.29	1.41	1.48	1.29	1.23	1.17
.77	1.21	1.59	1.45	1.59	1.82	1.73	1.56	1.58
.40	.70	.96	.98	1.12	1.15	.99	.90	.99
.46	.88	1.19	1.00	1.17	1.32	1.16	1.00	1.08
.25	.53	.77	.62	.68	1.01	.75	.52	.70

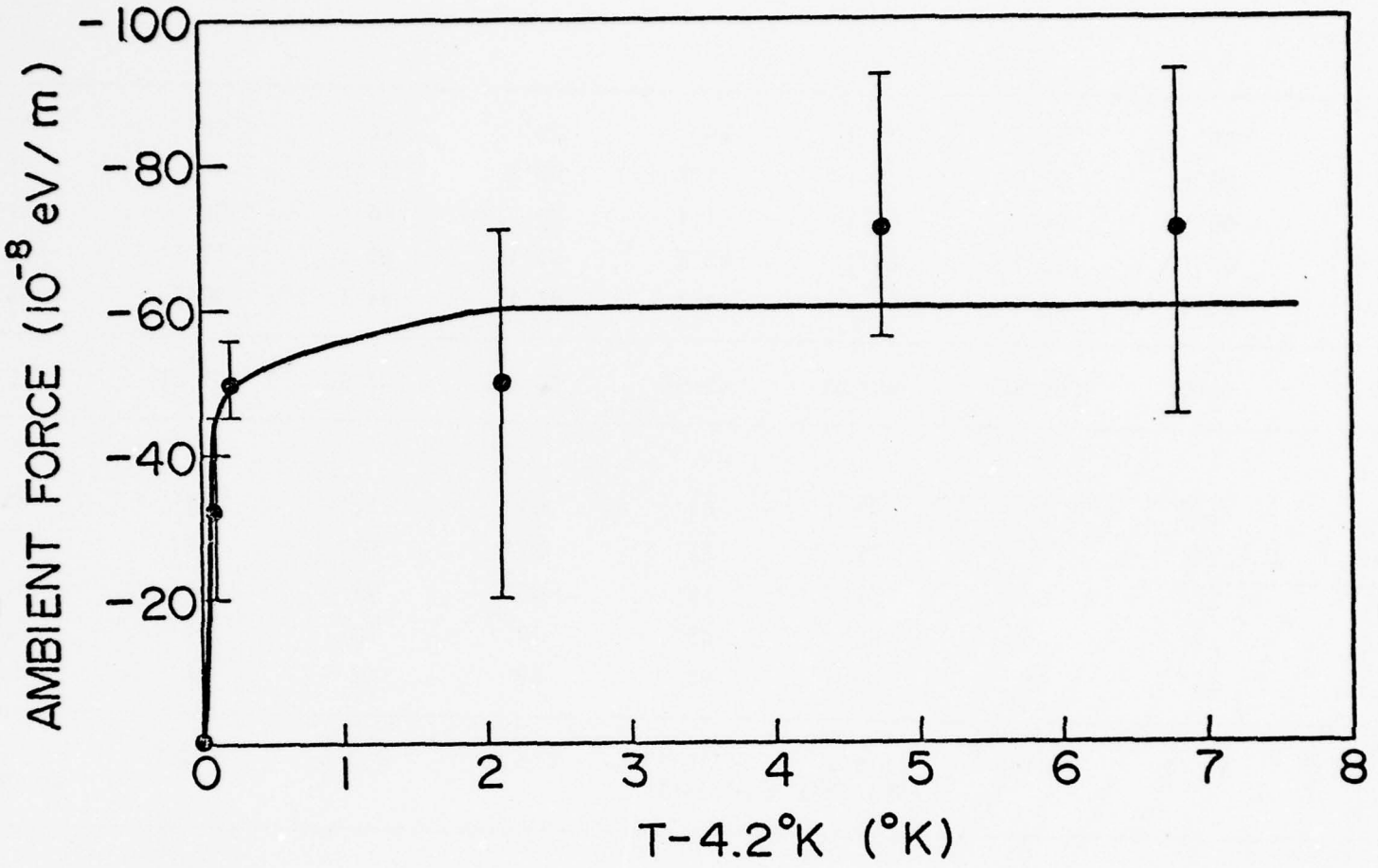


Fig. 5.3. A plot of the temperature dependence of the ambient force in the tube obtained by ratioing zero-applied-force TOF spectra taken at each of the indicated temperatures to an equivalent 4.2°K TOF spectrum. The method is explained in the text. The curve is only a guide to the eye and does not represent a theoretical fit.

the existence of an effective field at least that large at those temperatures. We feel that the only conclusion consistent with our results, the results of the Witteborn-Fairbank electron free fall experiment, and the results of the various experimenters who have studied gravitationally-induced and patch effect fields in metals is that there is a very effective surface shielding mechanism involving electrons which exists at 4.2°K but vanishes at temperatures only a few tenths of a degree higher.

It is possible that our results could be a manifestation of the appearance of large patch effect fields at temperatures just above 4.2°K; however, it is unlikely that patch effect fields would produce the reasonably consistent determination of effective ambient force from run to run which we observed. In any event, even if we are suddenly seeing large patch effect fields at 4.4°K, this still requires the kind of temperature-dependent electron surface shielding that we have discussed in order that the large patch effect fields not be present at 4.2°K.

Theoretical models for an electron surface state which has the requisite shielding properties, temperature transition, and lack of coupling to the strain field of the underlying metal are currently being considered by a group at Stanford under the direction of John Madey.[52] One of the possibilities is the type of electron surface state which arises from the discontinuity in periodic potential introduced when a crystal is terminated at a surface. Such surface states were first discussed by Tamm[53] and later by Shockley.[54] Another possibility is the type of surface state described by Schrieffer[55] in which electrons are free to move parallel to the

surface but motion normal to the surface is restricted. A good review of the literature on surface states is that of Davison and Levine.[56]

It is assumed that the nature of the temperature transition in the surface shielding effect is determined by the statistics of the surface electrons and their thermal distribution of energies. One can assume either that the surface electrons form a straightforward Fermi system or that each electron and its image in the metal couple to form an integral spin pair for which Bose statistics are appropriate. Both approaches have been pursued by Madey and his associates. It is possible that the temperature transition in the shielding comes about when the thermal energy of the surface electrons is no longer large compared to a particular type of electron-electron or electron-image interaction. For example, we may be seeing the effects of a transition to a Wigner solid[57] at the surface at low temperatures, or perhaps the onset of the type of exciton superconductivity discussed by Allender, Bray, and Bardeen.[58]

We are pursuing additional experiments in order to gain further knowledge of the parameters of the shielding effect and the conditions under which it occurs. Such knowledge would be quite useful in narrowing the range of physical mechanisms which could be responsible for the effect. The development of an actual model which explains the temperature-dependent surface shielding and which is consistent with the nature of our copper surface should be quite interesting.

REFERENCES

1. L. I. Schiff and M. V. Barnhill, Phys. Rev. 151, 1067 (1966).

2. A. J. Dessler, F. C. Michel, H. E. Rorschach, and G. T. Trammel, Phys. Rev. 168, 737 (1968).

3. F. C. Witteborn and W. M. Fairbank, Phys. Rev. Lett. 19, 1049 (1967); Nature 220, 436 (1968).

4. F. C. Witteborn, Ph.D. thesis, Stanford University (1965).

5. L. I. Schiff, Phys. Rev. B1, 4649 (1970).

6. P. P. Craig, Phys. Rev. Lett. 22, 700 (1969).

7. F. C. Witteborn and W. M. Fairbank, "Apparatus for Measuring the Force of Gravity on Freely Falling Electrons" (to be published).

8. C. Herring and M. H. Nichols, Rev. Mod. Phys. 21, 185 (1949).

9. D. H. Seib, Ph.D. thesis, Stanford University, p. 47 (1969).

10. N. Underwood, Phys. Rev. 47, 502 (1935).

11. W. F. Krolikowski and W. E. Spicer, Phys. Rev. 185, 882 (1969).

12. R. L. Paugh, private communication.

13. J. M. J. Madey, Ph.D. thesis, Stanford University, Part II (1970).

14. J. W. Allen, Trans. Faraday Soc. 48, 273 (1952).

15. N. P. Danilova and A. I. Shal'nikov, Prib. Tekh. Eksp. [Instrum. Exp. Tech.] No. 6, 199 (1967).

16. L. L. Antes and N. Hackerman, J. Appl. Phys. 22, 1395 (1951).

17. J. H. Parker and R. W. Warren, Rev. Sci. Instr. 33, 948 (1962).

18. N. Hackerman and E. H. Lee, J. Phys. Chem. 59, 900 (1955).

19. R. C. Tolman and T. D. Stewart, Phys. Rev. 8, 97 (1916).

20. C. Herring, Phys. Rev. 171, 1361 (1968).

21. L. I. Schiff, Phys. Rev. B1, 4649 (1970).

22. L. D. Landau and E. M. Lifshitz, Theory of Elasticity (Pergamon, Elmsford, N.Y., 1970), p. 15.

23. C. Kittel, Introduction to Solid State Physics (Wiley, New York, 1971), 4th ed., p. 247.

24. Ibid., p. 149.

25. Ibid., p. 248.

26. E. Wigner and J. Bardeen, Phys. Rev. 48, 84 (1935).

27. M. Peshkin, Phys. Lett. 29A, 181 (1969).

28. Schiff, loc. cit.

29. T. J. Rieger, Phys. Rev. B2, 825 (1970).

30. J. W. Beams, Phys. Rev. Lett. 21, 1093 (1968).

31. P. P. Craig, Phys. Rev. Lett. 22, 700 (1969).

32. S. H. French and J. W. Beams, Phys. Rev. B1, 3300 (1970).

33. E. W. Guptill, Can. J. Phys. 49, 3150 (1971).

34. C. R. Brown, J. B. Brown, E. Enga, and M. R. Halse, J. Phys. D4, 298 (1971).

35. E. Enga, Can. J. Phys. 52, 708 (1973).

36. Y. Goldstein, M. Cohen, and B. Abeles, Phys. Rev. Lett. 25, 1571 (1970).

37. G. T. Trammel and H. E. Rorschach, Phys. Rev. B2, 4761 (1970).

38. W. A. Harrison, Phys. Rev. 180, 1606 (1969).

39. B. M. Kincaid, private communication.

40. C. A. Mead, J. Appl. Phys. 32, 646 (1960).

41. H. Kanter and W. A. Feibelman, J. Appl. Phys. 33, 3580 (1962).

42. R. E. Collins and L. W. Davies, in Solid State Electronics (Pergamon, New York, 1964), pp. 445-453.

43. D. G. Onn, P. Smejtek, and M. Silver, J. Appl. Phys. 45, 119 (1974).

44. A. van der Ziel, Solid State Physical Electronics (Prentice-Hall, Englewood Cliffs, N.J., 1957), p. 106.

45. F. N. H. Robinson, Noise in Electrical Circuits (Oxford, London, 1962), p. 31.

46. J. R. Clement and E. H. Quinnell, Rev. Sci. Instr. 23, 213 (1952).

47. R. V. Stewart et al., A Compendium of the Properties of Materials at Low Temperatures (Phase II) (Clearinghouse for Federal Scientific and Technical Information, Springfield, Va., 1961), p. 45.

48. V. J. Johnson, ed., A Compendium of the Properties of Materials at Low Temperatures (Phase I): Part II. Properties of Solids (Clearinghouse for Federal Scientific and Technical Information, Springfield, Va., 1960), p. 4.112-1.

49. A. V. Gold et al., Phil. Mag. 5, 765 (1960).

50. A. J. Lichtenberg, Phase-Space Dynamics of Particles (Wiley, New York, 1969), pp. 30 ff.

51. S. L. Meyer, Data Analysis for Scientists and Engineers (Wiley, New York, 1975), p. 17.

52. J. M. J. Madey, private communication.

53. I. Tamm, Physik Z. Sowjetunion 1, 733 (1932).

54. W. Shockley, Phys. Rev. 56, 317 (1939).

55. J. R. Schrieffer, in Semiconductor Surface Physics, edited by R. H. Kingston (University of Pennsylvania Press, Phildelphia, 1957), p. 68.

56. S. G. Davison and J. D. Levine, Solid State Phys. 25, 37 (1970).

57. E. Wigner, Trans. Faraday Soc. 34, 678 (1938).

58. D. Allender, J. W. Bray, and J. Bardeen, Phys. Rev. B9, 119 (1974).